Max-Planck Institut für Biochemie
Abteilung Molekulare Strukturbiologie

Interpretation of electron tomograms of biological specimens by means of the Scaling Index Method

Alexandros A. Linaroudis

Vollständiger Abdruck der von der Fakultät für Chemie der Technischen Universität München zur Erlangung des akademischen Grades eines

Doktors der Naturwissenschaften

genehmigten Dissertation.

Vorsitzender:	Univ.-Prof. Dr. Johannes Buchner
Prüfer der Dissertation:	
	1. Hon.-Prof. Dr. Wolfgang Baumeister
	2. Univ.-Prof. Dr. Sevil Weinkauf

Die Dissertation wurde am 12.05.2006 bei der Technischen Universität München eingereicht und durch die Fakultät für Chemie am 25.07.2006 angenommen.

Abstract

Electron Tomography (ET) is uniquely suited to obtain three-dimensional reconstructions of pleomorphic structures, such as cells or organelles. Recent advances in the recording schemes improve the speed and resolution and provide new insights into the structural organization of different specimens. However the low signal to noise ratio arising from the radiation sensitivity of biological materials in conjunction with distortions introduced by the limited tilt range of the sample in the electron microscope, hinders the application of image processing methods for data analysis. Therefore a good signal improvement technique ("denoising" technique) is necessary. Additionally, the investigation of more complex and rather thick objects increases the image complexity. Image simplification techniques (interactive or automated) are necessary for separating the image into parts with similar or coherent properties, which improve the visualization capabilities as a consequence of focusing the 3D images on the parts of most interest and minimizing their size to the features of interest.

The major objective of this work was the development and application of methods for a quantitative evaluation and visualization of cryoelectron tomograms. A new noise reduction technique is proposed based on nonlinear anisotropic diffusion. It combines conventional diffusion methods with the scaling index method, the latter used for steering the filtering process. This diffusion technique shows a superior performance compared to existing diffusion realizations, as well as to conventional methods typically applied in image processing (e.g. low-pass filtering, median filtering). In addition, a novel approach for segmenation was developed that combines the information provided by the scaling index method with morphological operators, and subdivides the pixels/voxels into different categories according to the kind of structure to which they belong. Furthermore, a novel approach for identification of macromolecular complexes is proposed. The identification technique is not based on the similarity of the density values between input and target volume, as is the case in template matching, but on the similarity of the calculated scaling indices. The big advantage of this method is that it is very fast, since scaling index is rotationally invariant.

Abstrakt

Die Elektronentomographie (ET) ermöglicht die drei-dimensionale Darstellung von pleomorphen Strukturen, wie beispielsweise Zellstrukturen. Die stetige Weiterentwicklung der Methoden ermöglicht einen Einblick in den strukturellen Aufbau von verschiedenen Untersuchungsobjekten. Da die Daten von den Elektronentomogrammen ein niedriges Signal zu Rausch Verhältnis haben und Rekonstruktionsartefakte aufweisen, letztere bedingt durch den beschränkten Kippwinkelbereich, ist nur eine erschwerte Bildverarbeitung möglich. Deshalb sind gute Methoden zur Signalverstärkung (Entrauschungsmethoden) notwendig. Die zunehmende Komplexität der Untersuchungsobjekte erfordert den Einsatz von Segmentierungsmethoden (interaktiven oder automatisierten) zur Aufteilung des Bildes in verschiedene Regionen, welche zu einer Verbesserung der Visualisierungsmöglichkeit führt.

Das Hauptziel dieser Arbeit war die Entwicklung von Methoden für eine quantitative Auswertung und Visualisierung von Kryo-Elektrontomogrammen. Hier wird eine neue Entrauschungsmethode vorgeschlagen, die auf nicht linearer, anisotroper Diffusion basiert. Es handelt sich um eine Kombination von konventionellen Diffusionsmethoden und der Scaling Index Methode. Die Scaling Index Methode wurde in diesem Fall benutzt, um den Filterungsprozess zu steuern. Diese kombinierte Entrauschungsmethode hat im Vergleich mit entweder konventionellen Methoden wie zum Beispiel Tiefpassfilterung oder mit anderen existierenden Diffusionsprozessen, viel bessere Leistung gebracht. Außerdem wurde eine neue Methode zur Segmentierung entwickelt, die die Information der Scaling Index Methode mit morphologischen Operationen kombiniert, und die Pixels/Voxels entsprechend ihrer Struktur in verschiedene Gruppen einteilt. Weiterhin wird eine neue Technik zur Lokalisierung und Identifikation von Makromolekülen in Elektronentomogrammen ist präsentiert. Sie basiert nicht auf der Ähnlichkeit der Intensitätsgrauwerten von zwei Volumen, sondern auf der Ähnlichkeit ihrer kalkulierten Scaling Indices. Der größte Vorteil dieser Methode ist ihre Schnelligkeit, da die Scaling Index Methode rotationsunabhängig ist.

Contents

List of Figures

Chapter 1

Cryo-Electron Tomography of Biological Specimens

1.1 Introduction

Living things, though infinitely varied when viewed from outside, are fundamentally similar inside. Nowadays, it is common knowledge that all living things are made of cells, and that these units of living matter share the same machinery for their most basic functions. Cells are generally microscopic and have a highly complex architecture. It is hard to see their ultra structure, hard to discover their molecular composition, and harder still to find out how the various components function. The interest of modern molecular biology is focused on understanding the functions that take place inside the cell, performed by the so-called "molecular machines" [Alberts, 1998]. Molecular machines are multicomponent systems that are composed of macromolecules, mainly proteins. The structure of molecular complexes can be derived from data obtained with high-resolution techniques such as X-ray crystallography, nuclear magnetic resonance, or electron crystallography. Nevertheless, such techniques require the biochemical purification of the macromolecule. On the other hand, there are, particularly in Cell Biology, different forms of light microscopy that allow the study of cellular structures and their dynamics in physiologically compatible environment. Unfortunately, the resolution in light microscopy is not sufficient for the structure of macromolecules to be resolved.

Cryo-electron Tomography (CryoET) has the potential to bridge the gap between atomic structures defined by X-ray crystallography and the more global patterns of organization

that can be observed by light microscopy [Baumeister, 2002] [Baumeister and Steven, 2000]. This technique combines the power of 3D imaging with the preservation of the biological material in near-physiological conditions to obtain structural information at molecular resolution, avoiding at the same time the risk of artifacts associated with chemical fixation, staining or dehydration. Electron Tomography (ET) is based on a mathematical principle, that was first discovered by Radon [Radon, 1917] : A function can be reconstructed from its projections, provided that a sufficient number of projections in different directions is available. This principle is used in all methods of three-dimensional (3D) electron microscopy and was first implemented by DeRosier *et al.* [DeRosier and Klug, 1968] and Hart [Hart, 1968]. In order to acquire projections from different angles, the sample has to be mechanically tilted. The fundamental limitation in CryoET is the electron-dose that is used. Because of the fact that frozen-hydrated biological specimens are very sensitive to radiation damage, the tomogram has to be recorded under low-dose conditions, which results in poor contrast, a low signal-to-noise ratio (SNR) and a limited number of projections. A technical problem during the recording of a tomogram is the mechanical instability of the specimenholder. It is not possible to achieve mechanical precision on a nanometer scale, with the result that the specimen moves from its eucentric position during tilting. The development of microprocessor-controlled microscopes together with appropriate programs minimized the electron-dose, used for the necessary corrections, down to 3 percent of the total dose [Typke et al., 1991][Dierksen et al., 1992][Dierksen et al., 1993]. This allowed the recording of the first tomograms of frozen hydrated specimens [Dierksen et al., 1995]. The additional introduction of energy filters improved the image quality and led to the recording of the first tomograms of eukaryotic cells [Grimm et al., 1998]. Finally, the work of Medalia et al [Medalia et al., 2002] impressively showed that it is possible to visualize molecular machines like e.g. the 26S proteasome in the context of whole eukaryotic cells.

The technical developments and improvements in the field of CryoET in recent years made it possible to record high-quality tomograms of biological pleomorphic specimens as a matter of routine. CryoET is capable of answering significant biological questions by the evaluation of tomograms, and for all of the reasons mentioned above is considered to be the leading imaging technique for studying large, complex biological specimens with a resolution of a few nanometers.

Despite the improvements, the SNR of the electron micrographs remains unsatisfactory. Most of the electron tomographic reconstructions suffer from a very low SNR, which make further scrutiny of the specimen very difficult. Therefore a good signal improvement technique ("denoising" technique) is necessary. Additionally, the investigation of more complex and rather thick objects increases the image complexity. Image simplification techniques (interactive or automated) are necessary for separating the image into parts with similar or coherent properties, which improve the visualization capabilities as a consequence of focusing the 3D images on the parts of most interest and minimizing their size to the features of interest. This thesis is concerned with the improvement of visualization of 3-D reconstructions in CryoET. Three image processing techniques have been developed and implemented in the field of electron microscopy in order to improve the performance in terms of signal reconstruction, processing time and visualization : (a) a hybrid approach for nonlinear anisotropic diffusion, as a noise reduction method, (b) a Scaling Index Based Segmentation (SIBS) for automatic segmentation, and (c) fast automated detection of objects using the scaling index information. They are mainly based on the Scaling Index Method (SIM) and explore the applicability of the latter on tomographic data.

1.2 Transmission Electron Microscopy

1.2.1 Image Formation

Electron microscopy is the only technique capable of visualizing molecular structures in a cellular context, with a resolution in the nanometer range. The performance of the visualization is strongly dependent on the specimen preparation and the electron microscope itself. The image formation is the result of the interaction of an electron beam with the Coulomb potential of the specimen and the subsequent magnification by the objective lens. Thin biological objects are weakly forward scattering phase objects; therefore the image is approximately a projection of the density distribution, which is in its part linearly related to the Coulomb potential of the specimen. The electrons interact with atoms by elastic and inelastic scattering. In the case of bright-field electron microscopy, the contrast mechanism is actually a modification of the incident wave. Bright-field contrast is produced either by intercepting the electrons scattered at angles larger than the objective aperture

(scattering contrast), or by interference between the scattered wave and the incident wave at the image point (phase contrast). In transmission electron microscopy (TEM) both the elastically scattered and the inelastically scattered electrons contribute to the image intensity; nevertheless for thin and weakly scattering specimens, as observed in biological electron microscopy, the phase contrast gives the major contribution.

1.2.2 Contrast Transfer Function

As in the case of any optical instrument, the resolution limit is described by a point spread function (PSF). A point-like input signal produces output that is spread over a certain area of the image plane, and the distribution is described by the PSF. In the case of phase contrast, the electron beam modulation is described in Fourier space with the phase contrast transfer function (CTF).

$$PSF = \mathcal{F}(CTF) \tag{1.1}$$

The micrograph is a projection of the specimen's electrostatic potential, convoluted with the Fourier transform (symbolized by $\mathcal{F}$) of the CTF, in which the CTF describes the imaging conditions and the TEM properties. In other words, it characterizes the effect of the instrument on the image formation and is independent of the particular specimen in question:

$$CTF(f) = -2 \cdot \sin\left(\frac{\pi}{2} \cdot (C_S \lambda^3 f^4 - 2\Delta z \lambda f^2)\right) \tag{1.2}$$

where C_S is the spherical aberration constant, Δz the defocus, λ the wavelength of the electron beam, and f the spatial frequency.

1.2.3 Electron Microscope

The electron beam generated by a field emission gun (FEG) is preferred to a conventional, e.g. LaB_6, cathode in order to decrease the damping of the CTF at high spatial frequencies caused by spatial and temporal incoherence. The electrons are then accelerated with a tension that usually ranges between 100-300kV. The condensor system creates a parallel electron beam, which irradiates the specimen. The heart of the electron microscope is the objective lens,the properties of which determine the quality of the image (Figure 1.1).

The intermediate and projection lenses serve to magnify the primary image produced by the objective. The projection lens enlarges any defects of the objective lens, whereas defects in the projector itself are not subject to subsequent significant magnification and are thus not usually evident. The resulting image can be recorded by direct exposure of a photographic film or digitally via a phosphorescent screen coupled by a fiber-optic plate to a CCD camera.

1.2.4 Energy Filtering

Energy filtering is a viable way to circumvent the effects of the chromatic aberration of the Transmission Electron Microscopes, thus increasing the contrast [Lucic et al., 2005]. Energy filtering allows the selection of electrons with a specific kinetic energy for imaging. The mode of imaging which is most useful for low-dose applications is "zero-loss" energy filtering, where the energy selecting window is positioned at the energy of the primary beam, selecting only unscattered and elastically scattered electrons for imaging. The effect of zero-loss filtering becomes obvious in the case of thick specimens (0.2-1 μm). Energy filters operating in zero-loss mode eliminate all inelastically scattered electrons from the images, thereby reducing the image intensity and increasing the image contrast [Grimm et al., 1996]. This is why energy filters are indispensable for tomography of whole, ice-embedded cells [Grimm et al., 1997] [Grimm et al., 1998]. The effect of energy filtering is illustrated in Figure 1.2.

1.2.5 CCD Camera

Cooled charge-coupled device (CCD) cameras offer a number of advantages in recording images in electron microscopy. The immediate availability of the images acquired with a CCD camera in a digital format allows further real time image processing. In one important respect however, the use of photographic film has superior properties: the spatial resolution of CCD detectors so far are inferior to film. A solution to the limited resolution problem could be given by the latest developments in CCD cameras with large-area chips containing up to 4096x4096 pixels. Additional advantages of the CCD devices are the excellent linearity between input electron exposure and the output signal and their large dynamic range.

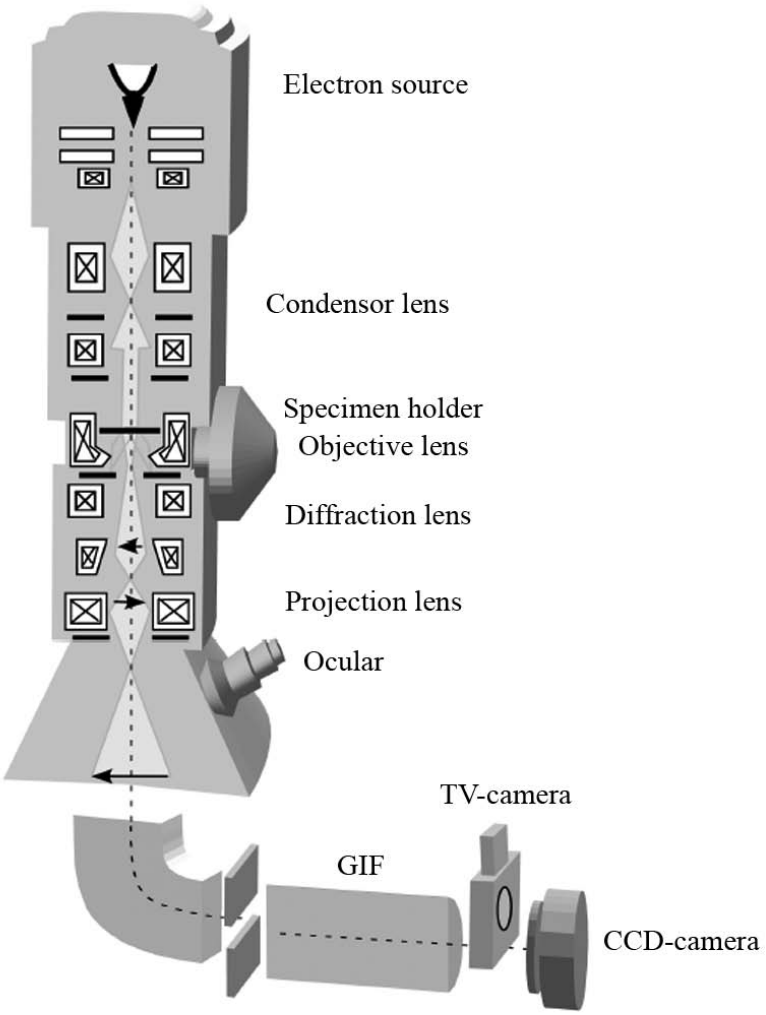

Figure 1.1: Scheme illustrating the CM300 TEM located in Martinsried. This instrument is equipped with a Gatan post-column energy filter (GIF) and a CCD camera. The picture is taken from [Schweikert, 2004].

In a CCD camera for electron microscopy, the electrons are first converted into photons by means of a scintillation screen at the entrance of the camera. The photons are then transported via fiber optic elements to the CCD chip, where the signal (image) is produced. The CCD chip is cooled to $-35°C$ in order to prevent the signal from the influence of thermally generated electrons.

1.3 Noise Model

The major noise contribution is associated with the illuminating beam (also called particle noise). The number of particles k in a given area (e.g., pixel) follows a Poisson distribution $P(k,\lambda) = \frac{\lambda^k}{k!} \cdot e^{-\lambda}$, with the variance ${\sigma^2}_{Part} \sim \lambda$. Considering λ as the expected signal, the signal-to-noise-ratio ($SNR = \frac{Power_{Signal}}{Power_{Noise}} = \frac{\lambda^2}{\lambda} = \lambda$) is proportional to λ. In the case of bright-field imaging of a weakly scattering objects, the expected signal is given by $\Delta\lambda = \lambda - \overline{\lambda}$, where $\overline{\lambda}$ is the mean value of the expected values of all pixels. Assuming that $\Delta\lambda \ll \overline{\lambda}$, the noise becomes signal-independent and therefore the approximation of additive Gaussian noise is valid [Hegerl and Hoppe, 1976]. Other noise sources, e.g. noise of the recording system etc., can then be assumed as additive and normally distributed. For various imaging techniques the noise can be closely modeled as additive Gaussian and

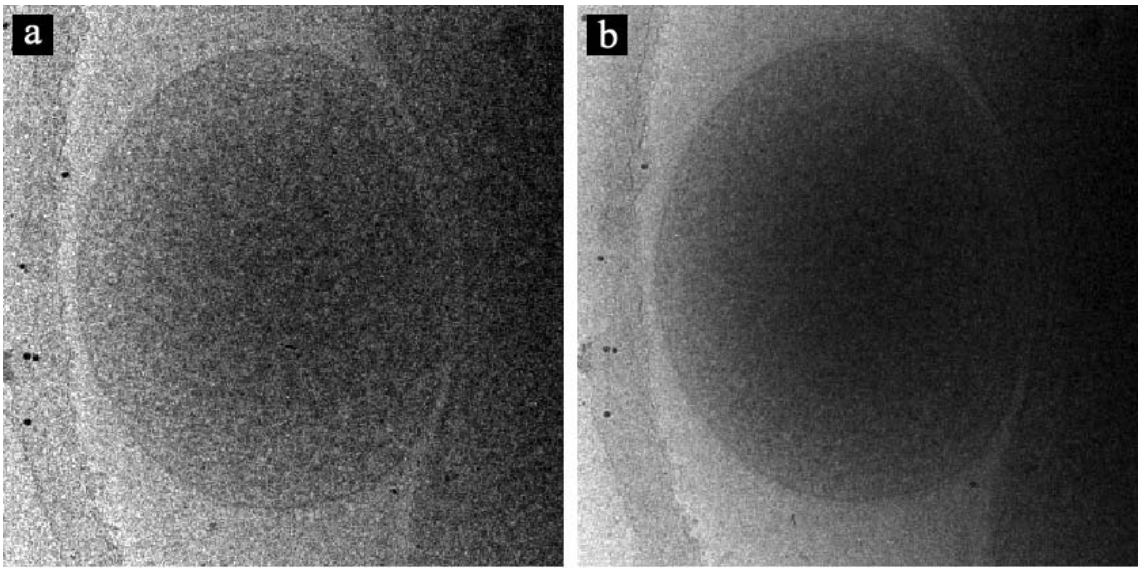

Figure 1.2: Digital micrographs without (a) **and with** (b) **energy filtering. Images** a **and** b **are *Thermoplasma acidophilum* images courtesy of C. Kofler, MPI Biochemistry, Martinsried.**

signal-independent [Donoho, 1993] [Donoho, 1995].

The signal reconstruction problem for this case is formulated in the following way: Let $\mathbf{y}$ be the noisy observation (projection images) of $\mathbf{x}$ (object under scrutiny), degraded by the noise $\mathbf{n}$, such that

$$\mathbf{y} = \mathbf{A} \cdot \mathbf{x} + \mathbf{n},$$

$\mathbf{A}$ (imaging process) represents a transformation matrix describing a linear operation applied to the object. The estimate $\overline{x}$ from $\mathbf{y}$ has to be determined such that the remaining noise in $\overline{x}$ is sufficiently low and $\overline{x}$ resembles $\mathbf{x}$ sufficiently closely. Depending on the image processing task and the specimen under scrutiny, the noise sources vary. Apart from the typical noise sources listed above, missing information as in the case of 3D electron microscopic reconstructions can introduce distortions.

1.4 Specimen Preparation

In electron tomography a very important step before the acquisition of the tomographic data is the preparation of the specimen. The task of specimen preparation methods is to stabilize and preserve the structural information of the biological sample. In electron microscopy, several preparation methods have been developed to increase the contrast and improve the signal-to-noise ratio. The preparation techniques used here can be separated into stained and frozen-hydrated samples.

The negative staining preparation is frequently used for single particle analysis. A heavy metal solution e.g. uranyl acetate is applied to the specimen, in order to fix it and enhance the contrast. Although this technique can provide high contrast and protects, at least to some extent, the specimen from collapsing, the resolution is limited due to the granulation of the heavy metal used. Additionally, structural changes (e.g. flattening) can appear. This applies also to stained cells or tissues.

In Cryo-electron microscopy the specimen grid, on which an aqueous solution containing the specimen is applied, is rapidly plunged into liquid ethane, whereupon the thin water later vitrifies. The rapid cooling rate prevents the water from turning into cubic ice.

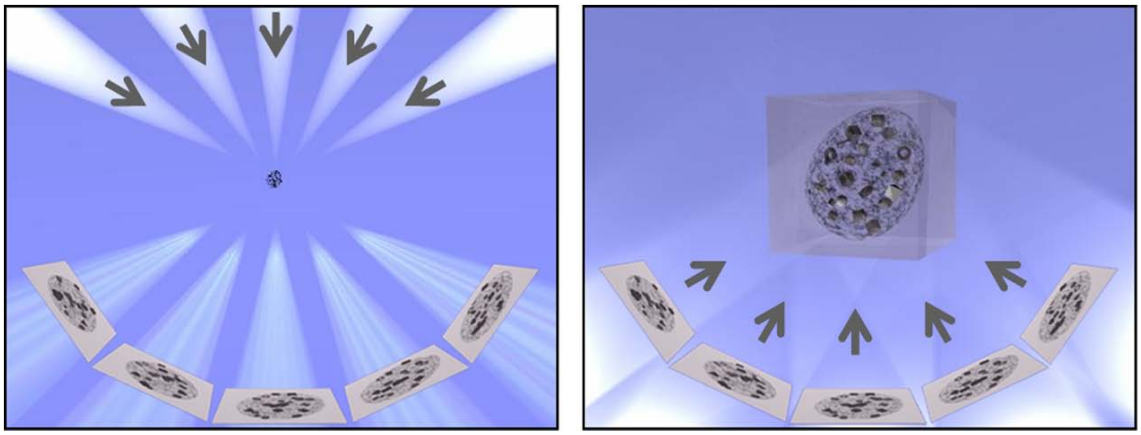

Figure 1.3: Principles of electron tomography: The reconstruction of an object from a series of transmission projections that are taken from different directions is commonly referred to as tomography. The picture is taken from [Nickell et al., 2006].

The grid is subsequently transferred to liquid nitrogen and mounted in the cryoholder of the electron microscope. The advantages of this technique are that the sample is kept in a near-to-native state and protected to some extent against radiation damage. However, the contrast of these samples is very low.

1.5 Electron Tomography

1.5.1 Projection Theorem

A transmission electron micrograph is essentially a projection of the specimen in the direction of view. As illustrated in Figure 1.3, in order to produce a three-dimensional representation of the structure, it is therefore necessary to combine information from a number of different projected views [Crowther et al., 1970].

The projection theorem [Hoppe and Hegerl, 1980] [Rosenfeld and Kak, 1982] states that the Fourier Transform of a two-dimensional projection of a three-dimensional object is identical to the corresponding (perpendicular to the projection's direction) central section of the three-dimensional transform of the object (Figure 1.4). The three-dimensional transform can therefore be built up plane by plane using the transforms of different projected views of the object.

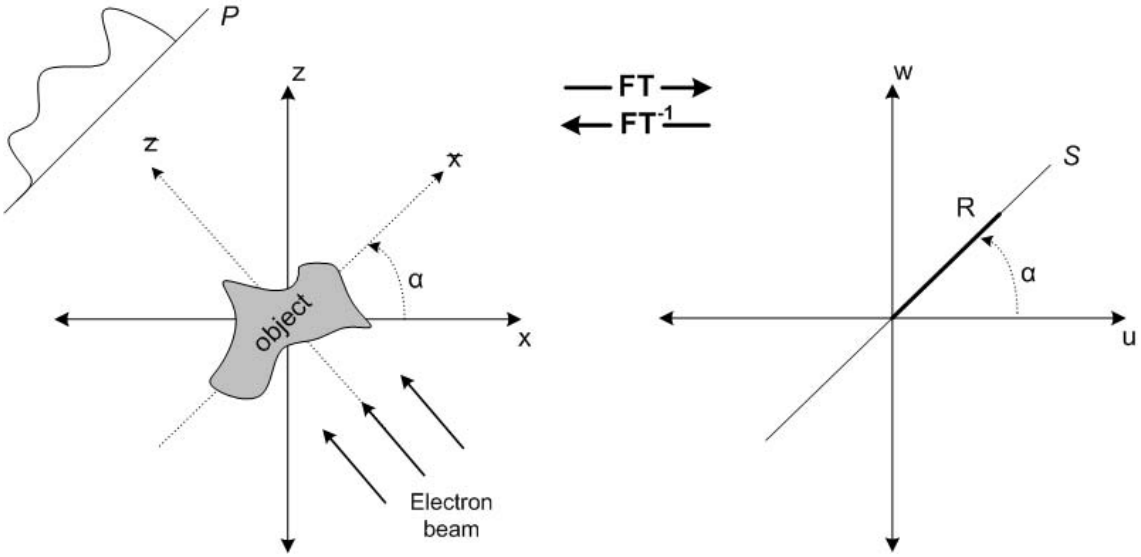

Figure 1.4: The projection P of an object in real space (left) corresponds to a central section S of the Fourier-Transformation of the object (right) and vice versa.

1.5.2 Tomographic reconstruction

The relationship between section and projection follows immediately from the form of the Fourier transform. The Fourier Transform of a single finite object f(x, y, z) is given by :

$$F(u,v,w) = \int_{-\infty}^{\infty}\int_{-\infty}^{\infty}\int_{-\infty}^{\infty} f(x,y,z)\cdot e^{-2\pi i(ux+vy+wz)}\mathrm{d}x\mathrm{d}y\mathrm{d}y \tag{1.3}$$

Tilting the object around the y-axis results in a translation invariance in the tomographic reconstruction, such that the reconstruction can be performed as a series of 2-D reconstructions in slices perpendicular to the tilt axis. The projection of the object along the z-axis when rotating the object in an angle α around the y-axis is given by :

$$p_\alpha(\overline{x}) = \int_{-\infty}^{\infty} f(\overline{x},\overline{z})\mathrm{d}\overline{z} \tag{1.4}$$

where

$$\begin{bmatrix} \overline{x} \\ \overline{y} \\ \overline{z} \end{bmatrix} = \begin{bmatrix} \cos\alpha & 0 & \sin\alpha \\ 0 & 1 & 0 \\ -\sin\alpha & 0 & \cos\alpha \end{bmatrix} \begin{bmatrix} x \\ y \\ z \end{bmatrix} \tag{1.5}$$

With $\mathrm{u} = \mathrm{R}\cos\alpha$ and $\mathrm{w} = \mathrm{R}\sin\alpha$ the Fourier Transformation of the projection is acquired :

$$P_\alpha(R) = \int_{-\infty}^{\infty} p_\alpha(\overline{x}) e^{-2\pi i R\overline{x}} \mathrm{d}\overline{x} = \int_{-\infty}^{\infty}\int_{-\infty}^{\infty} f(x,z) e^{-2\pi i R(x\cos\alpha + z\sin\alpha)} \mathrm{d}x\mathrm{d}z = F(R\cos a, R\sin a) \tag{1.6}$$

$$-\infty < R < +\infty, \quad 0 < \alpha < \pi$$

that corresponds to a plane in the Fourier space. By recording projections over the whole angle range $0 < \alpha < \pi$ it is possible to fully describe the object in the Fourier space and reconstruct it.

In practice, a different algorithm, namely weighted or filtered back-projection is mainly used for reconstruction in electron tomography, due to its simplicity and general applicability [Koster et al., 1998]. With this algorithm, the recorded images are multiplied with a ramp filter in the Fourier domain, transformed back into real space and inversely projected into the reconstructed volume. The reconstructed object is given by:

$$f(x,z) = \int_0^{2\pi}\int_0^{\infty} P_\alpha R e^{2\pi i R\overline{x}} \mathrm{d}R\mathrm{d}\alpha \tag{1.7}$$

For $-\infty < R < +\infty$ and $0 < \alpha < \pi$ the reconstructed object can be obtained from:

$$f(x,z) = \int_0^{\pi} \overline{P}_\alpha(x\cos\alpha + z\sin\alpha)\mathrm{d}\alpha \tag{1.8}$$

where

$$\overline{P}_\alpha(\overline{x}) = \int_{-\infty}^{\infty} P_\alpha |R| e^{2\pi i R\overline{x}} dR \tag{1.9}$$

In Figure 1.5 the 0° projection and a 2-D XY-slice of the tomographic reconstruction of a *Dictyostelium* cell are shown.

1.5.3 Dose Limitations

One of the main limitations in CryoET is the radiation damage of the biological specimens. Exposure of specimen to the electron beam leads to ionization, breaking of chemical bonds, and formation of free radicals. Although these processes are not temperature dependent, the resulting damage, loss of mass, and diffusion of free radicals is temperature dependent. For this reason the total electron dose has to be kept below a critical limit with the price of

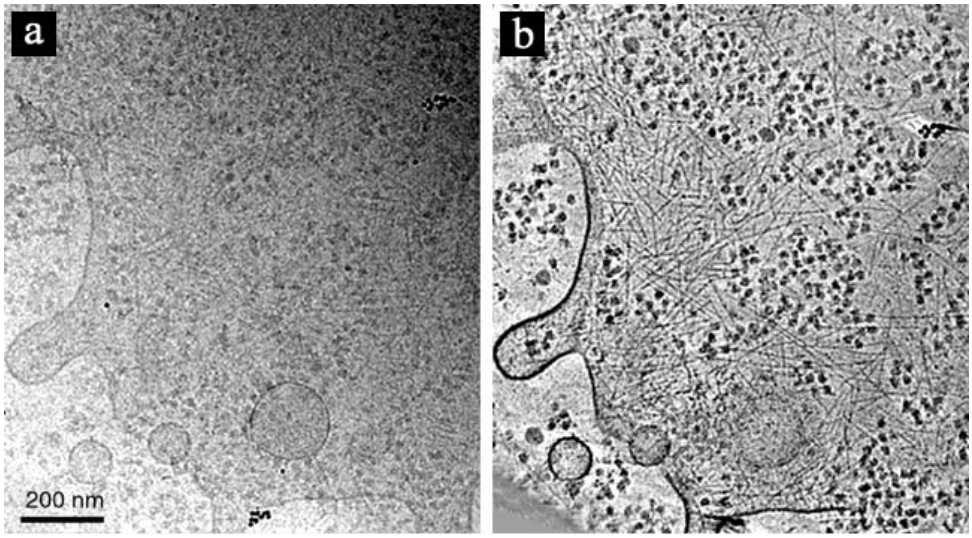

Figure 1.5: Tomogram of a *Dictyostelium* cell. *a*) 0° **projection, and** *b*) **2-D XY-slice of the reconstruction. The image is taken from [Medalia et al., 2002].**

a very low SNR that results in poor contrast. Radiation damage is greatly reduced when the specimen is investigated at liquid nitrogen temperature, −196°C. Further cooling to liquid He temperature (4 K) is advantageous for thin samples used in electron crystallography, but it is not clear yet if this also true for thicker icy layers used in CryoET [Dubochet et al., 1988]. In general, for our applications, a cumulative electron dose of approximately $50e^-/\text{Å}^2$ has turned out to be a reasonable choice.

Because of the large number of projections required for the reconstruction, one might suspect that a very high dose will accumulate during the collection of the data set. According to the dose fractionation theorem [Hegerl and Hoppe, 1976] the electron dose required to visualize structural details close to the resolution limit in a 3-D image is about the same as that for a 2-D image obtaining the equivalent information. This theorem was confirmed by McEwen [McEwen et al., 1995]. However, the advantages of a visualization in 3-D is that fine details become separated while they overlap in 2-D and thus will usually be obscured be other specimen features.

1.5.4 Missing Wedge

One of the biggest problems in CryoET is the problem of the "missing wedge". The computation of a distortion-free 3-D reconstruction from a single axis tilt series would require that

all projections of the sample over a full (±90°) tilt range are available [Barnard et al., 1992]. Unfortunately, physical limitations of the available holders allow a tilt range of ±70° with the result that the reconstruction will suffer from imperfections. The main distortion introduced by this limitation is the elongation of features in the direction of the angular gap (Figures 1.7 and 1.8). In the case of single axis tilting, the missing projections are arranged in Fourier space as a wedge of missing information that cannot be retrieved. This missing area in a sphere in Fourier space with radius r_o has a volume of :

$$V = \frac{8}{3} \cdot {r_o}^3 \cdot \theta_{max}$$

The missing wedge problem can be reduced by using a rotational holder. The idea is to merge two tilt series recorded at orthogonal tilt axis [Mannella et al., 1994] [Penczek et al., 1995]. After the recording of the first tilt series, the specimen is rotated 90° in the microscope and a second tilt series is recorded. The missing wedge now becomes a missing pyramid, reducing the amount of missing information.

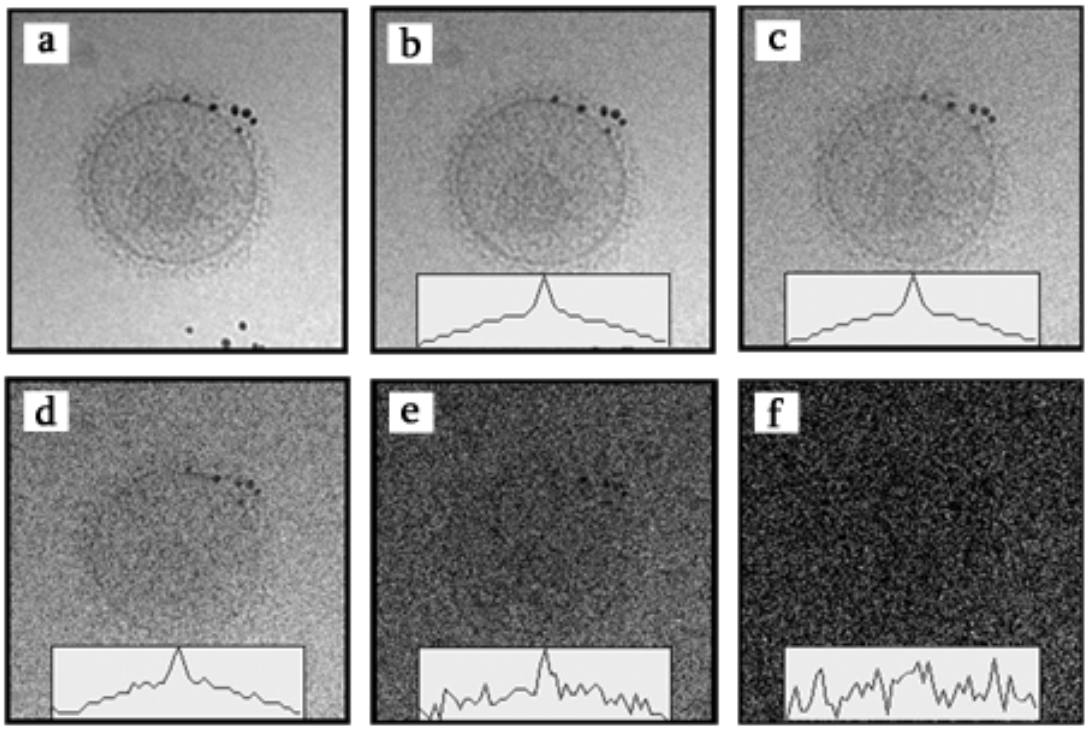

Figure 1.6: Scheme illustrating how the electron dose affects the signal-to-noise ratio. *a*) **original,** *b*) **using** $256e^-$ **per square pixel,** *c*) **using** $64e^-$ **per square pixel,** *d*) **using** $16e^-$ **per square pixel,** *e*) **using** $4e^-$ **per square pixel, and** *f*) **using** $2e^-$ **per square pixel.**

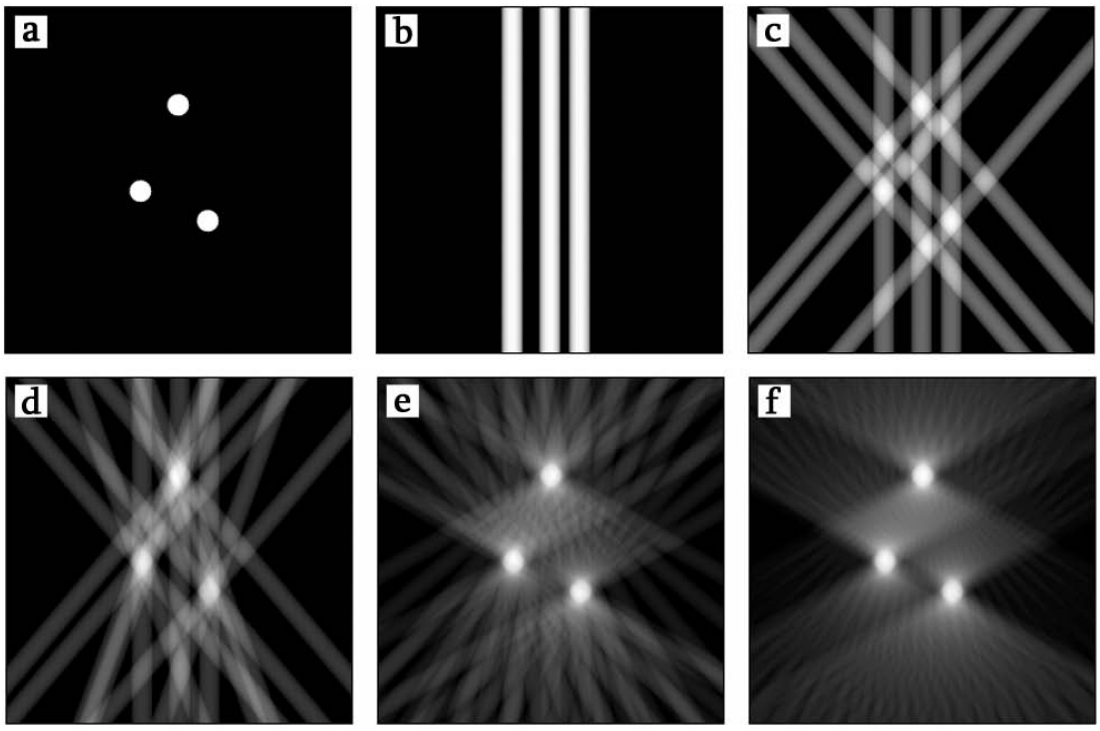

Figure 1.7: Reconstruction of the objects shown in (a) **by using** $b)$ **only 1 projection,** $c)$ **3 projections at angular steps of** $40°$**,** $d)$ **5 projection at angular steps of** $20°$**,** $e)$ **13 projections at angular steps of** $10°$**, and** $f)$ **25 projections at angular steps of** $5°$**.**

1.5.5 Automatic Data Acquisition

Due to mechanical imperfections of the goniometer, the tilt axis during the data acquisition is not completely stable and may move several hundred nanometers when the object is tilted. Because manual adjustment generally requires extensive exposure of the specimen to the electron beam, the automation of the acquisition process was crucial to acquiring tilt series under low-dose conditions.

In order not to lose the specimen area under investigation during recording of a tilt series, image shifts and focus changes have to be measured and corrected. The automated acquisition of a tilt series requires three basic steps [Dierksen et al., 1992]: tracking, autofocusing, and exposure (Figure 1.9). In the tracking procedure, a micrograph is recorded prior to the final exposure using a very low dose. Image shifts are measured by determining the

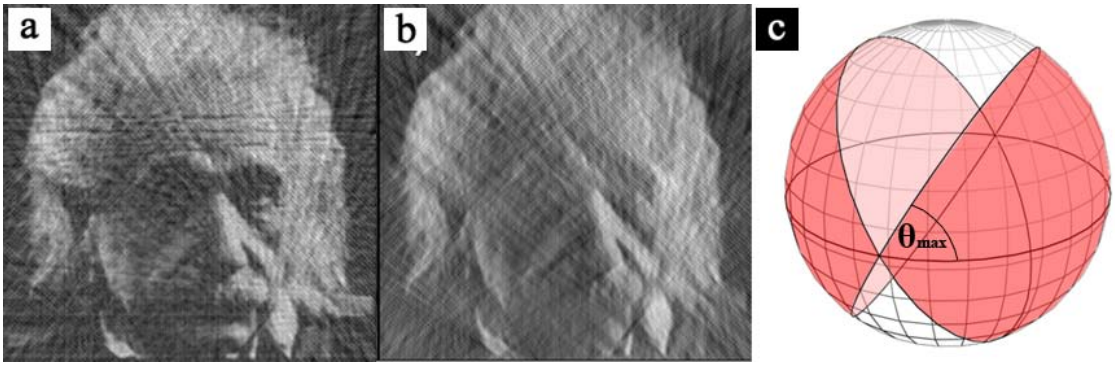

Figure 1.8: Reconstruction of the image of Einstein using a) **36 projections from** $-90°$ **to** $+90°$ **with angular step of** $5°$**,** b) **24 projections from** $-60°$ **to** $+60°$ **with angular step of** $5°$**,** c) **The missing projections build a wedge of missing information in Fourier space that cannot be retrieved.**

peak position in the cross-correlation function of the recorded micrograph with a reference image that was recorded previously. The autofocusing step compensates for the change of defocus because of specimen movement in the beam direction. The amount of image shift, measured by means of cross-correlation, is proportional to the defocus and can thus be used for focus correction [Koster et al., 1989][Koster and de Ruijter, 1992]. In the third step, a 2-D image, i.e. one projection of the tilt series is recorded. The three steps are repeated until the maximum permissible angular tilt range is covered.

1.6 Structure of this Thesis

In this thesis, three image processing techniques have been developed and implemented in the field of electron microscopy in order to improve the performance in terms of signal reconstruction, processing time and visualization. They are all based on the scaling index method, which is introduced and explained in the following chapter.

In Chapter 3 a new noise reduction (denoising) technique is proposed based on nonlinear anisotropic diffusion. Diffusion methods for signal reconstruction became widely applicable due to their well-established mathematical properties and their general well posedness. Several different methods have been proposed, mainly focused on edge detection and edge preservation, but none of them became applicable for highly degraded data. A new approach has been developed, which combines conventional diffusion methods with the scaling index method. The scaling index method in this approach is used as an alternative

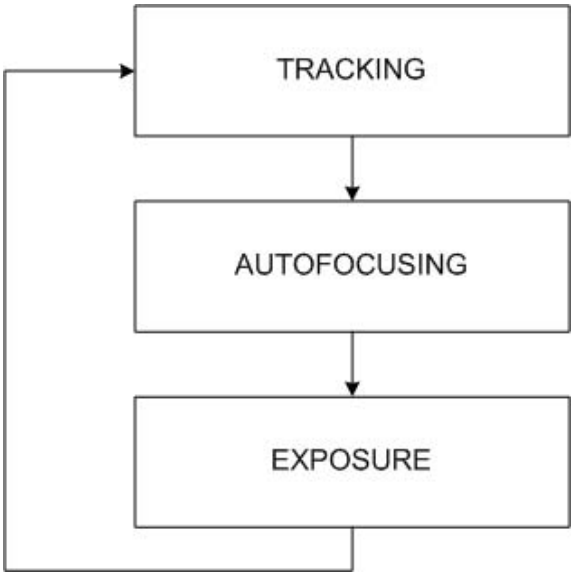

Figure 1.9: Scheme illustrating the steps followed during the automatic data acquisition.

to steer the diffusion process. This diffusion technique shows good performance compared to conventional methods typically applied in image processing (e.g. low pass filtering, median filtering). The SNR improvement is demonstrated by means of cross correlation and Fourier shell correlation functions.

In Chapter 4, SIBS (Scaling Index Based Segmentation) is presented as a novel approach for automatic image segmentation. Automatic grouping and segmentation is a challenging problem in the image-processing field. This technique is based on the structural information provided by the scaling index method. The scaling index is a number assigned to each voxel, which characterizes the dimensionality of the structural feature to which the voxel belongs [Jamitzky et al., 2001]. The large amount of noise present in the tomograms required further processing of the segmentation results with morphological operators. This method can be used either for 2-D images or for 3-D volumes. Additionally, there are not many parameters that have to be determined, so it is also suitable for non-experienced users. Application examples in 2D and 3D are presented.

It is one goal of tomography of whole cells to derive a cellular atlas of macromolecular complexes. Therefore, an approach is presented in Chapter 5 for detecting individual

macromolecules. This technique is also based on the information provided by the scaling index method. It shows equally good performance compared to existing cross correlation techniques with the advantage that it is much faster. Examples of artificial data are presented.

Chapter 2

Scaling Index Method

To interpret tomograms with maximum efficiency a decomposition of the data into their structural components is required. The information of the local structural properties in a tomogram, represented by a set of pixels/voxels, is of great importance and can be used in many different ways for further processing of microscopy data. It can be used as a noise identification tool that would be very useful for filtering noisy data, in order to enhance the signal. It can also be used as a segmentation tool for classifying objects present in an image/volume into different categories, according to the structure to which they belong.

The scaling index method (SIM) is a method to extract structural information from arbitrary data sets. Regarding electron tomography it can be used to characterize a voxel of a tomogram by its structural surroundings. In this chapter, the SIM is introduced and explained with simple examples. In addition to the classical scaling index [Jamitzky et al., 2001], the weighted scaling index [Räth et al., 2002] is presented as well.

2.1 Different Types of Scaling Index

2.1.1 Classical Scaling Index

The classical scaling index method originates from the theory of fractal geometry and is briefly explained as follows. Consider an image of size NxM pixels. For every point (x, y) in the range $0 < x < N$ and $0 < y < M$ there is defined a discrete gray value $g(x, y)$. Thus each pixel contains space and gray-value information that can be encompassed into a set of three-dimensional vectors $\mathbf{p} = [x, y, g(x, y)]$. The image can then be regarded as a set

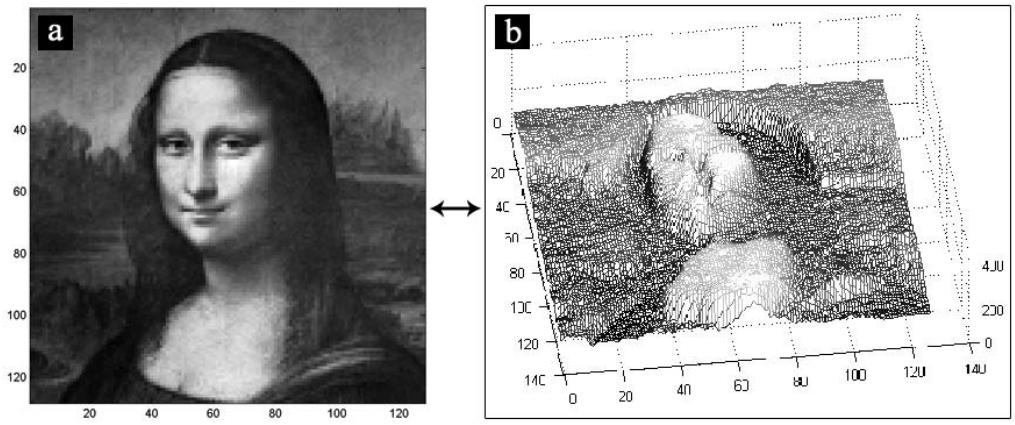

Figure 2.1: Conversion from a 2-D image to a 3-D representation in space.

of points p_i in 3-D space (Figure 2.1). In the case of 3-D data, volumes are converted to four dimensional (4-D) vectors.

A topological index, the scaling index α, is then defined for every point p_i in the space of corresponding higher dimensions by the following procedure : count the number N of points located inside a sphere with radius r around the point p_i :

$$N(p_i, r) = \sum_j \Theta(r - |p_j - p_i|) \tag{2.1}$$

In this equation Θ is the Heaviside function with:

$$\Theta(x) = \begin{cases} 1 & \text{if } x \geq 0 \\ 0 & \text{if } x < 0 \end{cases} \tag{2.2}$$

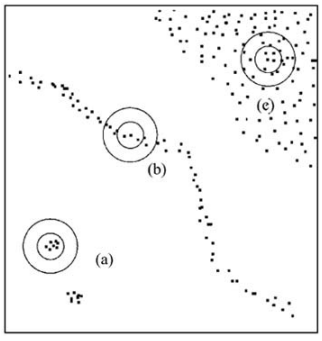

For many cases and wide scaling regions, one finds that as r increases, the number of points in the sphere is approximately given by the power law [Jamitzky et al., 2001]:

$$N(p_i, r) \propto r^{\alpha} \tag{2.3}$$

Figure 2.2: Scheme illustrating the different dimensionality of point distributions. *a*) **a point-like structure,** *b*) **a line-like structure, and** *c*) **an area-like structure. Image taken from [Jamitzky et al., 2001].**

In order to assess the value of α we consider two spheres with radii r_1 and r_2. Suppose there are N_1 points lying in the sphere with radius r_1 and N_2 points lying in the sphere with radius r_2 around p_i. If relation 2.3 is strictly valid, the power-law index α is given by the expression :

$$\alpha_i = \frac{log(N(p_i, r_2)) - log(N(p_i, r_1))}{logr_2 - logr_1} \tag{2.4}$$

This scaling index α measures the local topology of an image. By using an appropriate scaling range (r_1, r_2) it turns out that points which are part of clumpy structures will be represented by α-values close to 0. Points which are embedded in straight lines are identified by values of around 1, points in a flat distribution by values around 2, and so on.

N shows how different is the specified pixel from its surroundings, in relation to gray value differences and coordinate differences. The coordinate differences are for every pixel the same and thus can be described by a distance matrix (Figure 2.3). If N is big, this means that the gray values are similar. If N is small, this means that the specified pixel differs greatly from its surrounding pixels. In Figure 2.4, there are three test images (a, c, and e) and the corresponding calculated scaling indices (b, d, and f). Image (a) consists of constant gray-values. Consequently, only the coordinate distances contribute to the calculation of the scaling indices ($grayvalue_i - grayvalue_j = 0$) and the scaling index image also consists of constant values. Close to the borders of the image some artifacts can be observed, due to the limited neighborhood of the pixels used for the calculation of the scaling indices. In the particular example the scaling indices were calculated for $r_1 = 2$ and $r_2 = 4$, so Equation 2.4 becomes:

$$\alpha_i = \frac{log(N(p_i, 4)) - log(N(p_i, 2))}{log4 - log2} = \frac{log(49) - log(13)}{log4 - log2} = 1.9143$$

5√2					5					5√2
	4√2				4				4√2	
		3√2			3			3√2		
			2√2	√5	2	√5	2√2			
			√5	√2	1	√2	√5			
5	4	3	2	1	0	1	2	3	4	5
			√5	√2	1	√2	√5			
			2√2	√5	2	√5	2√2			
		3√2			3			3√2		
	4√2				4				4√2	
5√2					5					5√2

Figure 2.3: Distance matrix used for the calculation of the scaling indices.

As expected for other pairs of radii, the results were similar.

$[r_1, r_2]$	Value
$(2, 4)$	1.9143
$(3, 5)$	2.0108
$(3, 6)$	1.9622
$(5, 10)$	1.9685

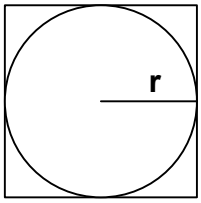

Assuming a uniform distribution, the number of points within a circle of radius r is proportional to $\pi \cdot r^2$

Points belonging to a uniform distribution take scaling index values around 2. This follows immediately from Equation 2.4 for $N = \pi \cdot r^2$:

$$\alpha_i = \frac{log(N_2) - log(N_1)}{log(r_2) - log(r_1)} = \frac{log(\pi) + 2log(r_2) - log(\pi) - 2log(r_1)}{log(r_2) - log(r_1)} = \frac{2 \cdot (log(r_2) - log(r_1))}{log(r_2) - log(r_1)} = 2$$

In the case of a line-like feature, N increases linearly with r. In Figure 2.5 as the window marked by a gray frame grows, the number of zeros contributing to the Scaling index value increases linearly. Each time we have $2r + 1$ zeros, so the scaling index α will have a value

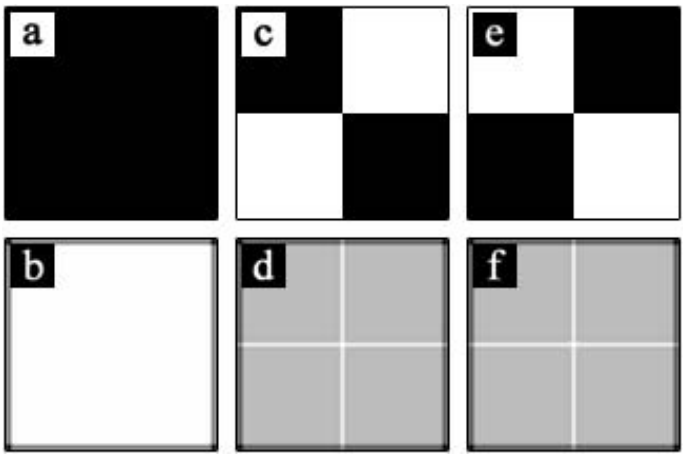

Figure 2.4: Simple SIM examples. Test images (a, c, e) and their calculated scaling indices (b, d, f), respectively.

255	255	255	0	255	255	255
255	255	255	0	255	255	255
255	255	255	0	255	255	255
255	255	255	0	255	255	255
255	255	255	0	255	255	255
255	255	255	0	255	255	255
255	255	255	0	255	255	255

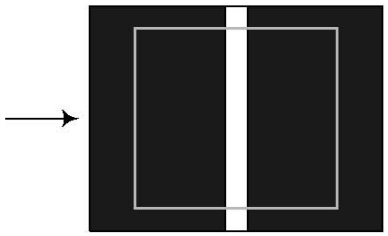

Figure 2.5: Image of a one pixel thick line.

around 1. Here are some values from the test image in Figure 2.5 for a pixel belonging to the white line with the following $[r_1, r_2]$ combinations :

$[r_1, r_2]$	Value
$(2, 4)$	0.8840
$(3, 5)$	0.8842
$(3, 6)$	0.9329
$(5, 10)$	0.9397
$(9, 13)$	0.9529

In the case of noisy pixels, the scaling index α takes a value > 2. This is explained in the following example : an image composed of constant gray-values (Figure 2.6a) is represented by a plane in 3-D space (Figure 2.6b). Assuming two spheres with radii r_1 and r_2 $(r_1 < r_2)$, the number of points included in the spheres is proportional to $\pi \cdot r^2$ (Figure 2.6c), thus the scaling index takes the value of 2. In the case where noise is added to the image (Figure

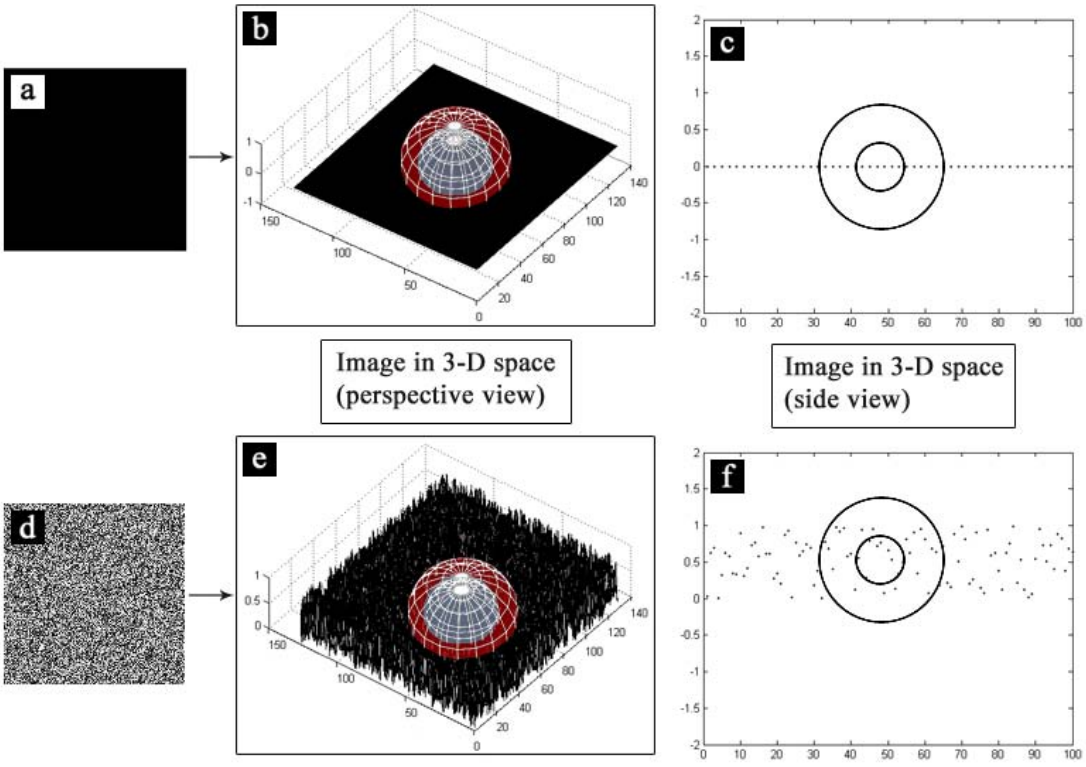

Figure 2.6: Scheme illustrating the influence of noise to the scaling index value.

2.6d), the variations of the gray-values correspond to translations of the points along the z-axis in 3-D space (Figure 2.6e). These translations have as a result that some points are excluded from sphere with radius r_1, while they are still included in the sphere with radius r_2 (Figure 2.6f). In that case the nominator in Equation 2.4 increases compared to the case of no noise ($\log N(p_i, r_1)$ decreases while $\log N(p_i, r_2)$ remains nearly unchanged), while the denominator remains constant and scaling index α takes values greater than 2.

Mona Lisa is used here as a test image. In Figure 2.7, the histograms of the calculated scaling indices are presented for selected pairs of radii. In Figure 2.8, the same example is presented, this time with Gaussian noise added, showing that the noise causes a shift of the histogram to the right. The values of the scaling index have increased, which is expected because of the presence of noisy pixels in the image.

General properties of Scaling Index

- **Reverse Contrast invariance**

  The scaling index algorithm does not take gray values into account, but only gray-

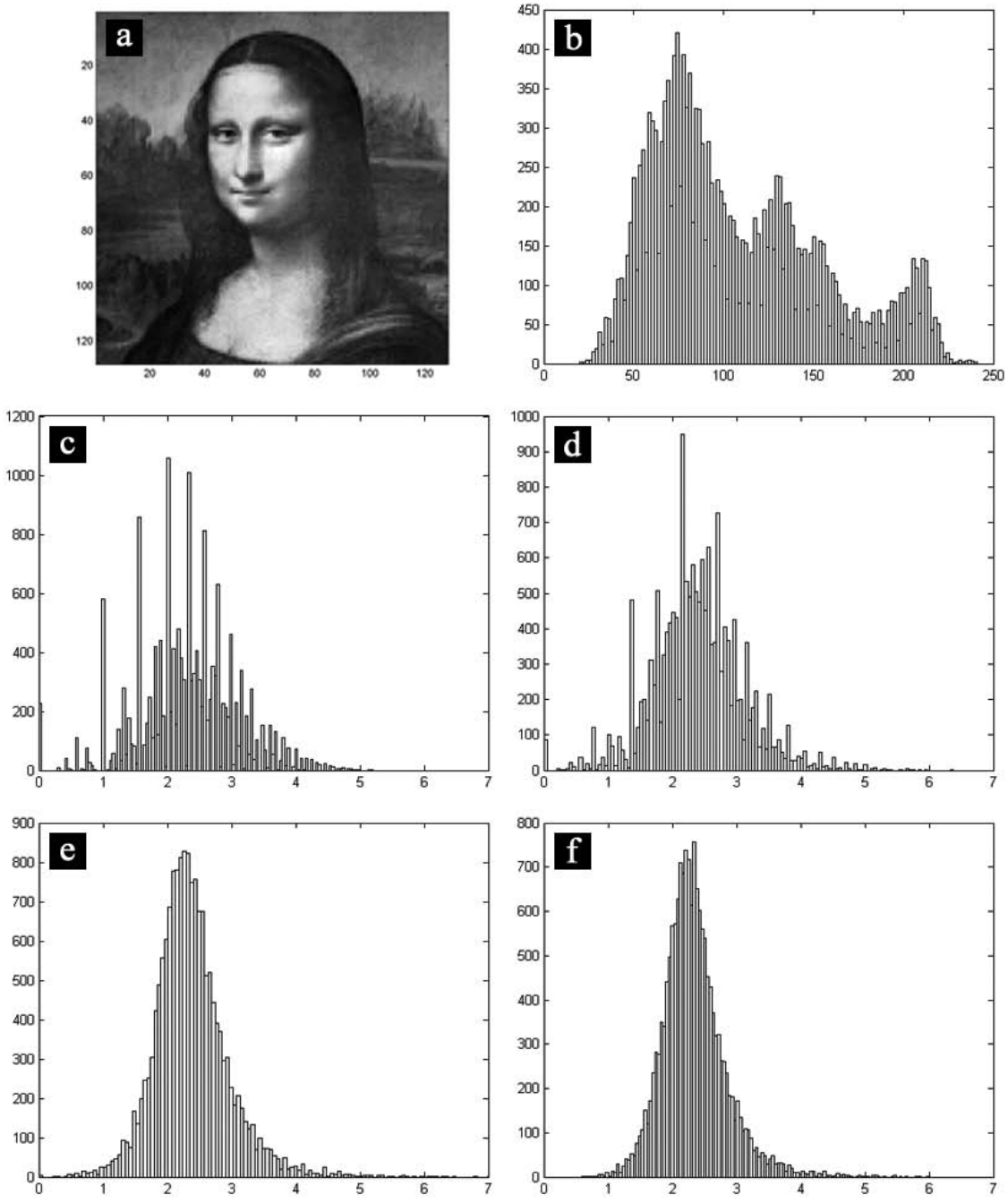

Figure 2.7: Calculated scaling indices for the test image, Mona Lisa a**) Mona Lisa image** b**) histogram of the gray values of the image in** (a)**. Histogram of scaling indices for** c**)** $[r_1,r_2]=[2,4]$**,** d**)** $[r_1,r_2]=[3,5]$**,** e**)** $[r_1,r_2]=[5,8]$**, and** f**)** $[r_1,r_2]=[5,10]$**.**

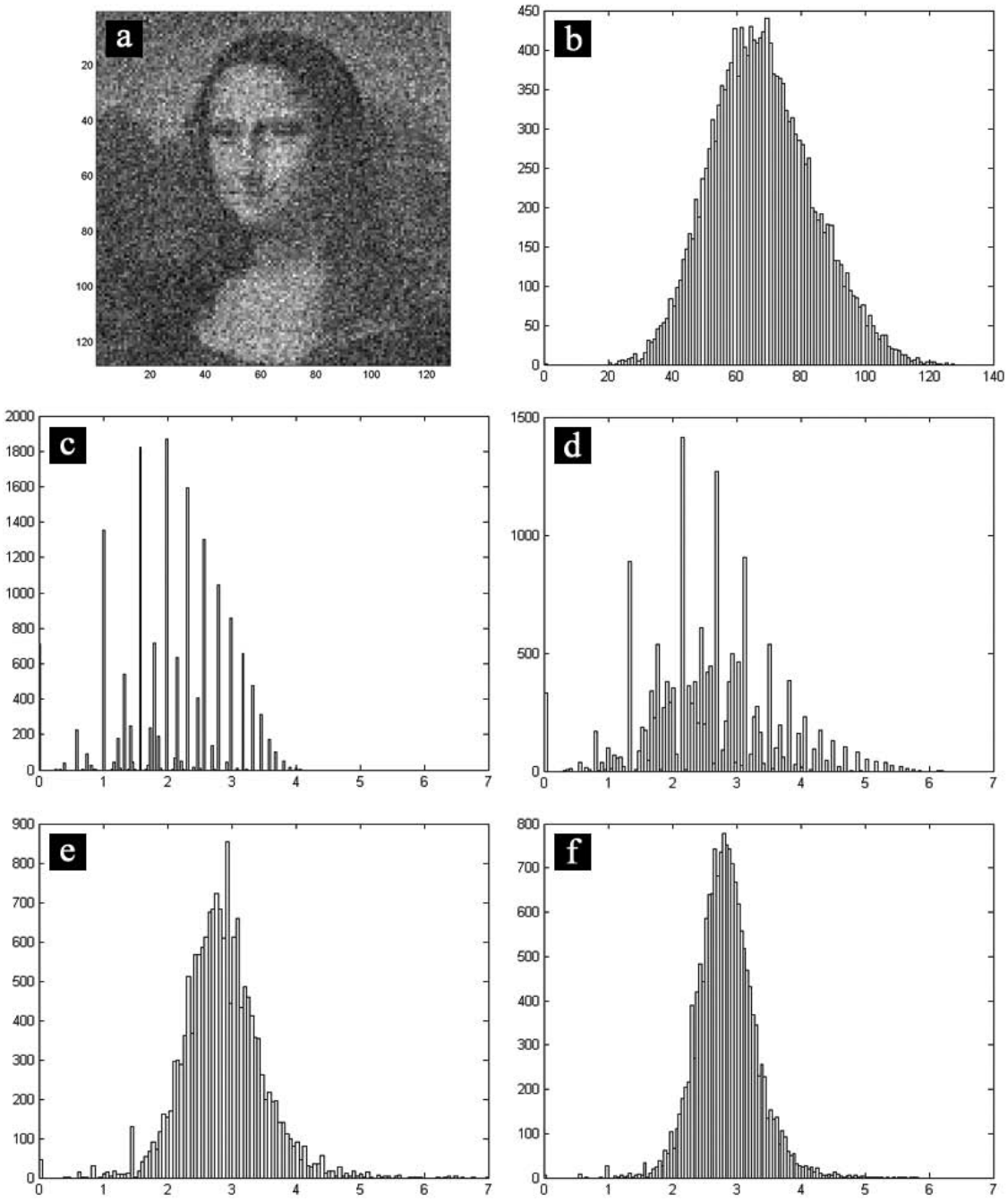

Figure 2.8: Calculated scaling indices for the test image Mona Lisa with gaussian noise added *a)* **Mona Lisa image with gaussian noise** *b)* **histogram of the gray values of the image in** (a)**. Histogram of the scaling indices for** *c)* $[r_1,r_2]=[2,4]$**,** *d)* $[r_1,r_2]=[3,5]$**,** *e)* $[r_1,r_2]=[5,8]$**, and** *f)* $[r_1,r_2]=[5,10]$**.**

value or contrast differences, therefore it is reverse contrast invariant. The pairs of images (c,d and e,f) in Figure 2.4 demonstrate that property.

- **Gray level shift invariance**

  The scaling index is gray level shift invariant. We may shift the grey level range by an arbitrary constant C, and the calculated scaling indices will remain unchanged.

- **Rotational invariance**

  The scaling index method classifies objects present in an image or a volume, according to the kind of structure to which they belong, and regardless of their orientation.

2.1.2 Weighted Scaling Index

The Weighted Scaling Index Method is a modified version of the Scaling Index, proposed by Räth [Räth and Morfill, 1997]. In this case the Heaviside function is replaced by a Gaussian distribution. Consider a set of N points $P = \{\overrightarrow{p_i}\}$,$i = 1, ..., N$. For each point, the local weighted cumulative point distribution ϱ is calculated. In general form this can be written as:

$$\varrho = (\overrightarrow{p_i}, r) = \sum_{j=1}^{N} s_r \left(d \left(\overrightarrow{p_i}, \overrightarrow{p_j} \right) \right) \tag{2.5}$$

where $s_r(\bullet)$ denotes a shaping function depending on the scale parameter r and $d(\bullet)$ is a distance measure.

The weighted scaling indices $\alpha \left(\overrightarrow{p_i}, r \right)$ are obtained if we set in Equation 2.4 $r_1 = r$ and $r_2 = r + \Delta r$ and take the limit for $\Delta r \to 0$:

$$\alpha \left(\overrightarrow{p_i}, r \right) = \lim_{\Delta r \to 0} \frac{\log(N(P, r + \Delta r)) - \log(N(P, r))}{\log(r + \Delta r) - \log(r)} \tag{2.6}$$

but

$$\log(r+\Delta r)-\log(r) = \log(r \cdot (1+\frac{\Delta r}{r}))-\log(r) = \log(r)+\log(1+\frac{\Delta r}{r})-\log(r) = \frac{\Delta r}{r} \tag{2.7}$$

for $\Delta r \ll r$, $\log(1 + \frac{\Delta r}{r})$ can be approximated by $\frac{\Delta r}{r}$

and

$$\begin{aligned}\log(f(r+\Delta r)) - \log(f(r)) &= \log(f(r) + \Delta r f'(r)) - \log(f(r)) = \\ &= \log(f(r) \cdot (1 + \frac{\Delta r}{f(r)} \cdot f'(r))) - \log(f(r)) = \\ &= \log(f(r)) + log(1 + \frac{\Delta r}{f(r)} \cdot f'(r)) - \log(f(r)) = \\ &= \frac{\Delta r f'(r)}{f(r)} \end{aligned} \tag{2.8}$$

from 2.7 and 2.8 Equation 2.6 can be rewritten:

$$\alpha\left(\overrightarrow{p_i}, r\right) = \lim_{\Delta r \to 0} \frac{\frac{\Delta r N'(r)}{N(r)}}{\frac{\Delta r}{r}} = \lim_{\Delta r \to 0} \frac{r \cdot N'(r)}{N(r)} = \frac{r}{N} \frac{\partial}{\partial r} N\left(\overrightarrow{p_i}, r\right) \tag{2.9}$$

In principle, any differentiable shaping function and any distance measure can be used for calculating α. In our experiments, we use the Euclidean norm as distance measure and a set of Gaussian shaping functions. So the expression for ϱ simplifies to:

$$\varrho = \left(\overrightarrow{p_i}, r\right) = \sum_{j=1}^{N} e^{-\left(\frac{d_i j}{r}\right)^q}, \quad d_i j = \|\overrightarrow{p_i} - \overrightarrow{p_j}\| \tag{2.10}$$

Now Equation 2.9 can be rewritten:

$$\alpha\left(\overrightarrow{p_i}, r\right) = \frac{\sum_{j=1}^{N} q \left(\frac{d_{ij}}{r}\right)^q e^{-\left(\frac{d_{ij}}{r}\right)^q}}{\sum_{j=1}^{N} e^{-\left(\frac{d_{ij}}{r}\right)^q}} \tag{2.11}$$

The exponent q controls the weighting of the points according to their distance to the point for which α is calculated. For small values of q, points in a broad region around $\overrightarrow{p_i}$ contribute significantly to the weighted local density $\varrho\left(\overrightarrow{p_i}, r\right)$. With increasing values of q, the shaping function becomes more and more a step-like function, counting all points with $d_{ij} < r$ and neglecting all points with $d_{ij} > r$. In this study, we calculate α for the case $q = 2$.

An advantage of the weighted version of the scaling index in comparison to the classical scaling index is that now the user has to define only one radius instead of two. The parameter r determines the length scale on which the structures are analyzed. Obviously the value of α strongly depends on the choice of r. If r approaches zero, each point "sees" no neighbors due to the sharp decrease of the shaping function with increasing distance $d_{ij} = \|\overrightarrow{p_i} - \overrightarrow{p_j}\|$, so each point forms a point-like structure ($\alpha = 0$) with itself as only member. If r has the length scale of the structures to be analyzed, one obtains the full spectrum of α values belonging to different structural elements. If r is further increased the differences of the structural elements become less pronounced whereas edge effects begin to play an important role. Thus the frequency distribution narrows and shifts to lower values of α (for a detailed example, refer to section 4.1). The second parameter that has to be determined is the gray-value range. It may be necessary to normalize the gray values g_i so that x, y, and g are within a comparable range. One possible normalization is given by $\tilde{g} = g(N/128)$. In all of the examples presented in this work, $\tilde{g}$ ranges from 0 to 128. A small or large scaling simply determines which is the most dominant feature in the vector d_{ij} (Equation 2.10). For a detailed example demonstrating the influence of the gray-value range on the scaling indices, the reader is referred to section 4.1.

Chapter 3

Nonlinear Anisotropic Diffusion

Although great effort has been made for tomographic data collection and three-dimensional reconstruction, visualization of tomograms is cumbersome due to the low-dosage and low contrast imaging conditions that can be used for the tomography. The consequences are that the signal is not directly accessible, since it is buried in noise (SNR$<$0 db). An interpretation of the 3D images using surface- and volume-rendering techniques is difficult due to the noise sensitivity of the rendering algorithms. A denoising algorithm suitable for such applications must be able to preserve as much signal as possible while reducing the noise sufficiently.

Anisotropic Nonlinear Diffusion (AND) is currently one of the most widely used noise reduction techniques in the field of computer vision [Weickert, 1998a]. This technique takes into consideration the local structure of the image/volume in order to perform noise reduction on the basis of global signal properties. Conceptually, AND can be considered as an adaptive gaussian-based filtering technique in which, for every voxel in the volume, an anisotropic 3D Gaussian function is computed whose sigmas and orientations depend on the local structure. AND has already been introduced and assessed in the field of CryoET [Frangakis and Hegerl, 2001] [Fernandez and Li, 2005], and in fact has been crucial in some of the most recent breakthroughs [Grünewald et al., 2003].

In this work a novel hybrid diffusion approach for AND-based denoising is presented that combines AND with the SIM. The scaling index is a number assigned to each voxel, which characterizes the dimensionality of the structural feature to which it belongs. The information provided by the SIM is used in order to drive the diffusion process. Qualitative and quantitative measures are used for assessing the spectral signal reconstruction perfor-

mance on synthetic and biomedical volumetric images. The method performed very well compared to conventional noise reduction methods (e.g. gaussian and median filtering) as well as to other different types of diffusion and to the bilateral filter.

3.1 Diffusion Types

The evolution of an image $I = I(\mathbf{x}, t)$ processed by a diffusion technique can be described with the following partial differential equation (PDE):

$$I_t = div(\mathbf{G} \cdot \nabla I) \tag{3.1}$$

where ∇I is the gradient with respect to the coordinate vector $\mathbf{x}$ in a space of arbitrary dimension N, I_t denotes the derivative related to the processing time t, and $\mathbf{G}$ is a tensor called diffusivity, designed to steer the direction of the diffusion process. The diffusivity is a quadratic, positive semidefinite matrix, with dimension N.

3.1.1 Linear Diffusion

In the simplest case, $\mathbf{G}$ is a diagonal matrix with equal and constant elements g and the equation becomes linear. The general diffusion equation (equation 3.1) can be rewritten for the linear case in the following form:

$$I_t = g\Delta I \tag{3.2}$$

The resulting linear isotropic diffusion corresponds to Gaussian real space filtering with a variance that increases with time $\sigma^2 = 2 \cdot g \cdot t$.

3.1.2 Nonlinear Isotropic Diffusion

In order to improve on the linear isotropic diffusion, especially with respect to edge preservation, Perona and Malik used a monotonically decreasing function $g(I)$ instead of a constant g, such that the diffusion flux was minimized over edges [P.Perona and Malik, 1990] [Perona and Malik, 1987]. This nonlinear, yet isotropic process results in intraregional smoothing between well-preserved edges and avoids the overall blurring that is typical for linear diffusion. They solved a partial differential equation (PDE) of the form:

$$I_t = div(g(\nabla I)\nabla I) \tag{3.3}$$

with a scalar diffusivity:

$$g(\nabla I) = \frac{1}{1 + \frac{|\nabla I|^2}{\kappa^2}} \tag{3.4}$$

where κ is user defined and contrast dependent.

Apart from discretization problems, this approach is still limited by the isotropy of the equation: only the intensity of diffusion flux can be controlled but not its direction. This results in a preservation of noise along the edges, a highly undesirable property.

3.1.3 Nonlinear Anisotropic Diffusion

In the nonlinear, anisotropic case the diffusivity $\mathbf{G}$ has non-diagonal elements different from zero. The direction information is gained from the structure tensor $\mathbf{J}_0 = \nabla I \cdot \nabla I^T$ or from its average over a small 3D volume $\mathbf{J}_{\sigma_T} = \mathbf{J}_0 * \mathbf{K}_{\sigma_T}$, where $\mathbf{K}_{\sigma_T}$ is a Gaussian filter with variance σ_T. The eigenvectors $\mathbf{v}_i$ of $\mathbf{J}$ and the corresponding eigenvalues μ_i characterize the local structural features of the image I within a neighborhood of size $O(\sigma_T)$. Each eigenvalue μ_i reflects the gray level variance in the direction of the eigenvector $\mathbf{v}_i$. The first eigenvector $\mathbf{v}_1$ corresponding to the eigenvalue μ_1 is a local average over the directions of maximum variance. The eigenvalues are non-negative since the structure tensor is positive semidefinite. In the case of a non-averaged structure tensor ($\sigma_T = 0$), the relations $\mathbf{v}_1 = \frac{\nabla I}{|\nabla I|}$ and $\mu_1 = |\nabla I|^2$ hold, while all other eigenvalues are equal to zero. The structural information expressed in the eigenvalues μ_i and eigenvectors $\mathbf{v}_i$ is used to define the diffusivity tensor.

$$\mathbf{G} = \begin{bmatrix} \mathbf{v}_1 & \mathbf{v}_2 & \mathbf{v}_1 \end{bmatrix} \cdot \begin{bmatrix} \lambda_1(\mu_1, \mu_2, \mu_3) & 0 & 0 \\ 0 & \lambda_2(\mu_1, \mu_2, \mu_3) & 0 \\ 0 & 0 & \lambda_3(\mu_1, \mu_2, \mu_3) \end{bmatrix} \cdot \begin{bmatrix} \mathbf{v}_1 & \mathbf{v}_2 & \mathbf{v}_1 \end{bmatrix}^{\mathbf{T}} \tag{3.5}$$

The parameters λ_i steer the diffusion flux in the direction of $\mathbf{v}_i$.

The major problem is how to define the diffusion tensor such that the basic structural features of the object are preserved. For instance, the question arises as to how to choose the λ_i values such that a line-feature is processed with a $1D$ diffusion flux and a surface-feature with a $2D$ diffusion flux. The application of the wrong flux would produce artifacts in the former case, such as a unidirectional broadening of the line (e.g., sword-like structures) and in the latter case, the shape of the surface would not be revealed. A solution to this problem could be given with the second eigenvalue μ_2, which is capable of detecting the kind of the local geometric feature. Unfortunately, in the case of very noisy data, this local

information is very uncertain. Therefore, only a $1D$ diffusion flux ($\lambda_1 = \lambda_2$) is applied [Frangakis and Hegerl, 2001].

3.1.4 Coherence and Edge Enhancing Diffusion

In his 2D setup, Weickert has proposed two different realizations of diffusion processes, namely coherence enhancing diffusion (CED) and edge enhancing diffusion (EED). Extending the CED method from 2D to 3D the parameters are chosen such that:

$$\lambda_1 = \lambda_2 = \alpha \quad and \quad \lambda_3 = \alpha + (1-\alpha) \cdot e^{-\frac{C}{(\mu_1 - \mu_3)^2}} \tag{3.6}$$

with user-defined global parameters α and C [Weickert, 1998b]. Usually a small value has to be assigned to α. For $\alpha \to 1$ the approach converges to Gaussian filtering, realized perfectly for $\alpha = 1$. The amount of flux in the orientation of smallest variations perpendicular to the gradient is determined by the difference $\mu_1 - \mu_3$. This difference is large for flowlike structures (e.g., parallel lines running in the same direction as in a fingerprint) due to a high variance in one direction and consequently such structures are extremely enhanced. Areas containing only noise are characterized by $\mu_1 \approx \mu_2 \approx \mu_3$ and therefore remain unmodified. With CED the diffusion flux can be steered in the preferred local orientation and can thus, as an example, be used to connect interrupted lines.
The second approach called edge enhancing diffusion (EED) is based on the eigenvectors of the non-averaged structure tensor $\mathbf{J}_0$ and uses

$$\lambda_1 = \lambda_2 = \frac{1}{1 + \frac{\mu_1}{\kappa^2}} \quad and \quad \lambda_3 = 1 \tag{3.7}$$

Due to $\mu_1 = |\nabla I|^2$, this approach is equivalent to the method proposed by Perona and Malik. Therefore, edges are preserved and smoothing the areas between these edges reduces the noise.

3.1.5 Scaling Index used for filtering

The scaling index can be thought of as a quality indicator for each pixel. According to its value, it could be possible to classify the pixels into different categories. This could lead to an improvement of the quality of the image by filtering only the noisy pixels and preserving the rest. The noisy pixels would be selected by thresholding the scaling indices appropriately. Experiments have shown that scaling indices above 2.4 refer to noisy pixels.

The first attempts to improve the quality of an image were made in the sense of selecting the noisy pixels by thresholding the scaling indices and then applying filter operations to the selected group of pixels. The selected pixels were filtered either by average or by median filter. The result of the filtering was cross-correlated with the original test image and the calculated cross-correlation coefficients were used as a criterion for the performance of the filtering operation. Figure 3.1 shows several filtered images created using different filters and different kernel sizes.

In the table below, the Cross-Correlation Coefficients (CCC) of the used filters are presented, and it is clear that the scaling index compared to the other filters did not perform so well. Although the same threshold was chosen for both scaling index methods (SIM and WSIM) during the filtering operations, WSIM performed a little better (CCC 0.9326, still not satisfactory). The reason is that the use of one radius allows more precise control over the method. The filtered images are shown in Figure 3.2.

Method	**Size of the neighborhood**	**CCC**
Wiener Filter	3x3	0.9111
Median Filter	3x3	0.9066
Lowpass Filter	-	0.9074
Scaling Index Average Filter	3x3	0.8461
Weighted Scaling Index Average Filter	3x3	0.9326

3.2 Scaling Index Based Diffusion

One of the very first experiments performed with the scaling index was its comparison to a gradient operator with respect to recognition of structures. For this experiment the image of Mona Lisa was used as a test image. As illustrated in Figure 3.3, while in the case of no noise both methods succeed in identifying the structural components of the image, in the case with noise, the scaling index method outperforms the gradient operator. Scaling index manages to detect features of the face of Mona Lisa even in the noisy image, whereas in the gradient image only the contour of the head is recognizable. Despite the unsuccessful combination of the scaling index information with basic filters, this experiment proved that scaling index could be used effectively for filtering.

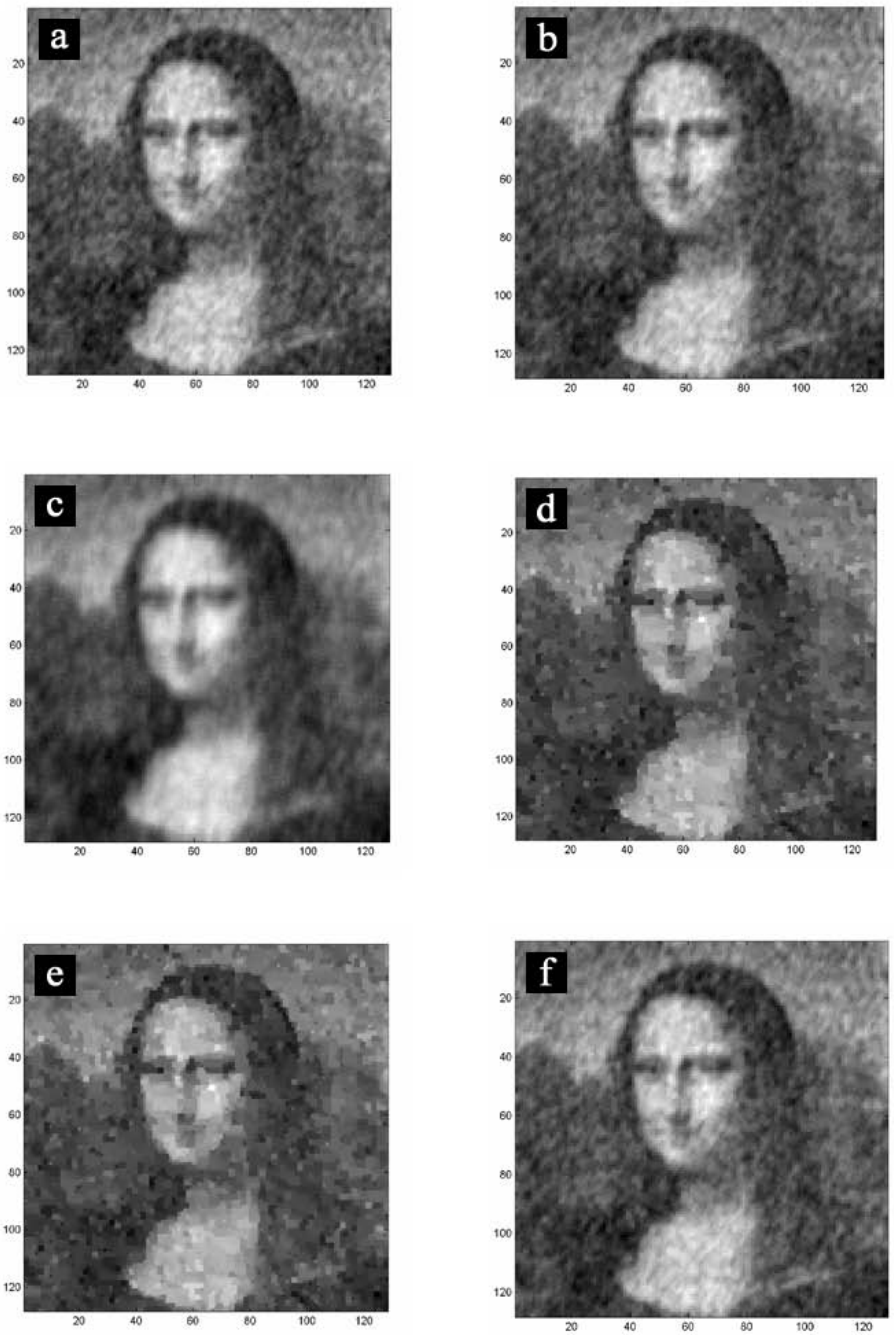

Figure 3.1: Different filters and threshold values applied to the noisy image of Mona Lisa *a)* **average filter with kernel 3x3 for [r_1,r_2]=[5, 10] and threshold > 3.6,** *b)* **average filter with kernel 3x3 for [r_1,r_2]=[5, 10] and threshold > 2.5,** *c)* **average filter with kernel 5x5 for [r_1,r_2]=[5, 10] and threshold > 3.6,** *d)* **median filter with kernel 3x3 for [r_1,r_2]=[5, 10] and threshold > 3.6,** *e)* **median filter with kernel 3x3 for [r_1,r_2]=[5, 10] and threshold > 2.2, and** *f)* **average filter with kernel 3x3 for [r_1,r_2]=[5, 10] and threshold < 0.5 & threshold > 2.2.**

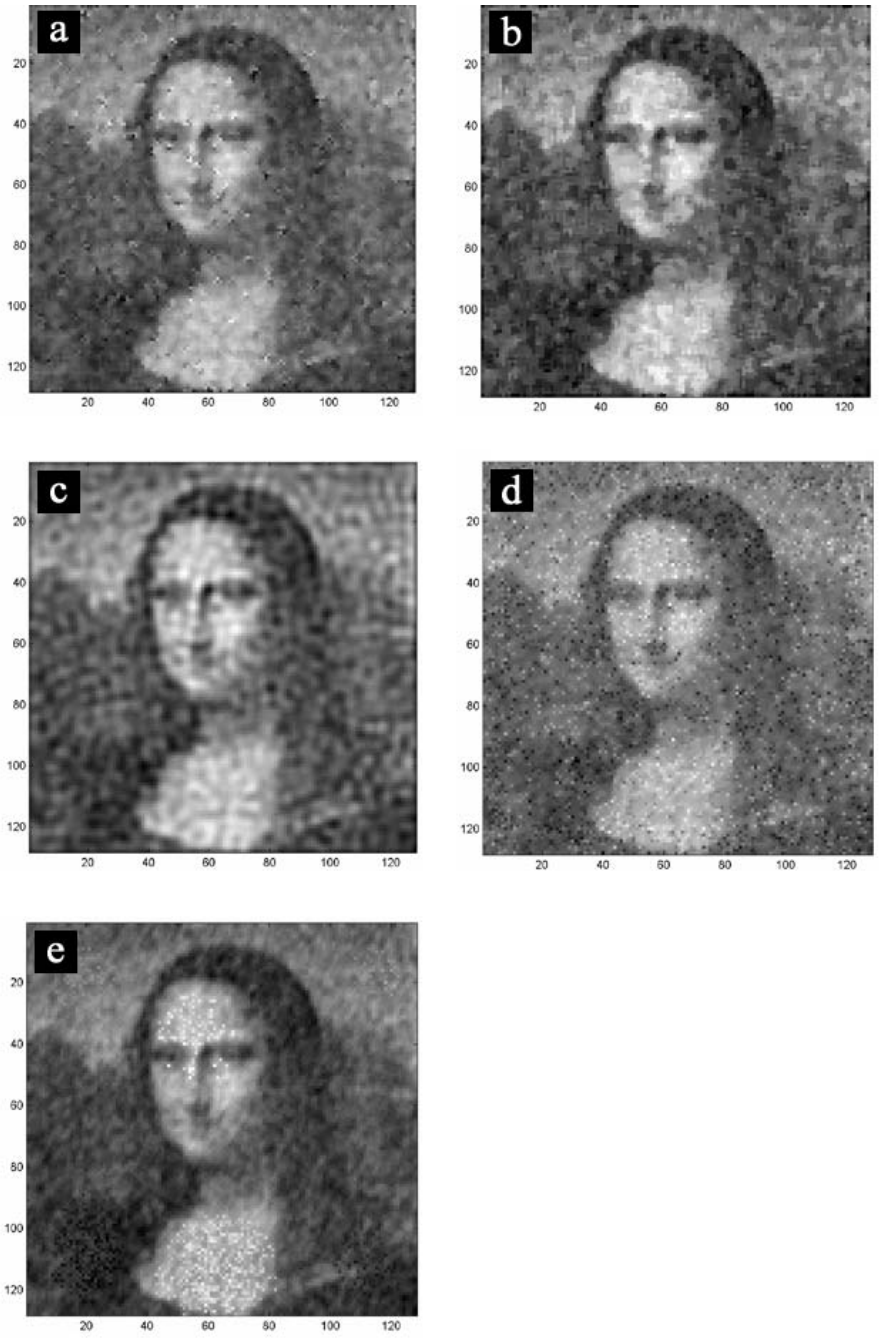

Figure 3.2: Mona Lisa image filtered by a) **wiener filter,** b) **median filter,** c) **low-pass filter,** d) **scaling index average filter for [r_1,r_2]=[5,10] and** $\alpha < 0.5$ **&** $\alpha > 2.2$**, and** e) **weighted scaling index average filter for** $r = 8$ **and** $\alpha < 0.5$ **&** $\alpha > 2.4$**.**

The information provided by the scaling index method was used for driving more complex filtering algorithms. Based on the idea of combining the advantages of EED and CED [Frangakis and Hegerl, 2001], a scaling index based approach of NAD was implemented and is explained as follows: since the scaling index classifies pixels according to the structure to which they belong, it can be used as a trigger for switching between the two diffusion versions. EED is applied when the scaling indices lie between 0.7 and 1.2, indicating that a line-like structure is present, and CED otherwise. In this way, edges will be preserved and enhanced, whereas homogeneous surfaces and noisy areas will be smoothed. For calculating the scaling index based diffusion, the program of Frangakis [Frangakis and Hegerl, 2001] was used, with the necessary modifications made for importing the scaling index criterion. The parameter setting for the hybrid diffusion, as well as for the scaling index based diffusion was done according to the suggestions presented in that paper. In all of the examples in this chapter, the presented images are normalized for $\pm 3\sigma$, where σ is the variance of the images.

3.3 Results

3.3.1 Simulated Data

In order to study the properties of the denoising algorithm, it was applied to a simulated tomographic reconstruction of a hollow sphere containing blobs of different size and a vertical thin line. Figure 3.4 shows slices through the tomogram, which was calculated by weighted back-projection from projection images in the angular range from $-60°$ to $+60°$ with an increment of $6°$. The thin line perpendicular to the XY-plane is represented as a dot. As can be seen in the 3-D representation of the dataset (Figure 3.7), deformation on the top and bottom of the sphere has been introduced, due to the missing wedge.

The scaling index based approach turns out to be superior to conventional filters, like Gaussian low-pass filter or median filter. The Gaussian filter produces a blurred image where fine details like the thin line inside the sphere disappear (Figure 3.5a), whereas the median filter preserves the line better than the Gaussian, but fails in smoothing the background (Figure 3.5b). With edge enhancing diffusion the edges are better preserved, as the diffusion flux is smaller in places with large gradients. Nevertheless, lines and curves

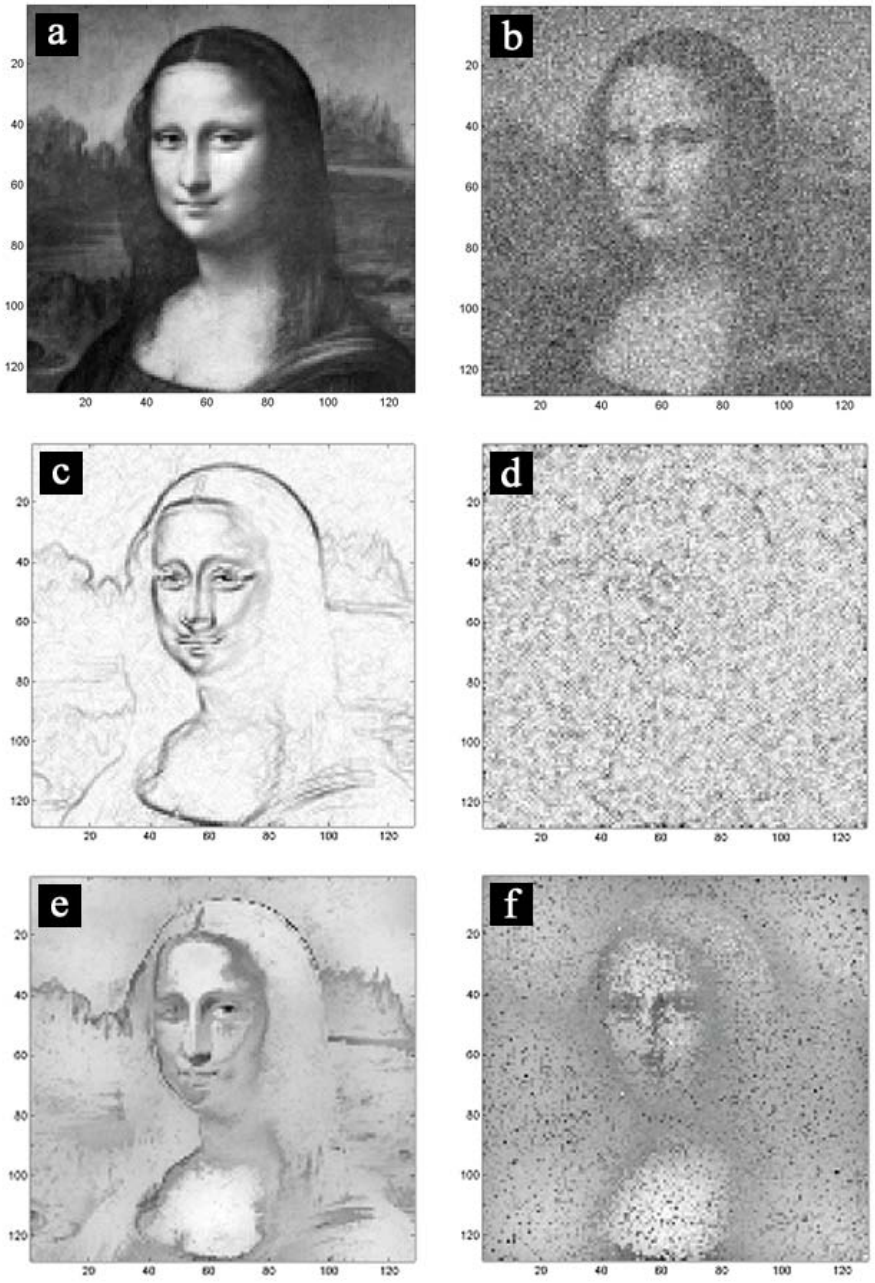

Figure 3.3: Comparison between Scaling Index and Gradient Operator $a)$ **image of Mona Lisa,** $b)$ **image of Mona Lisa with noise added,** $c, d)$ **gradient operator of the images a and b respectively,** $e, f)$ **weighted scaling indices for** $r = 8$ **of the images a and b, respectively.**

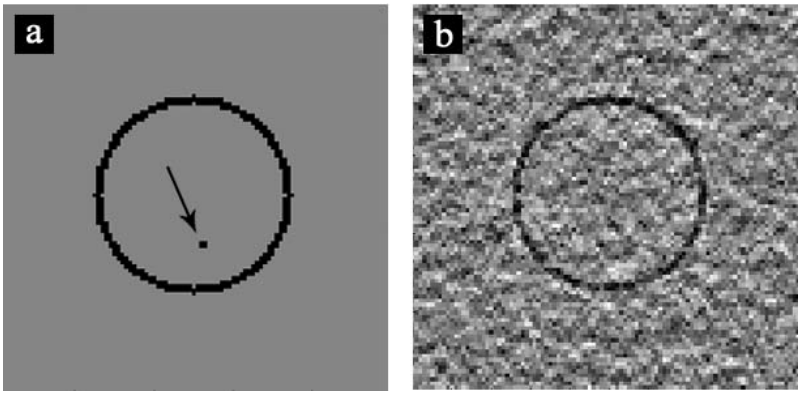

Figure 3.4: Simulation of tomographic data *a*) **original volume consisting of a hollow sphere containing a vertical thin line indicated by an arrow,** *b*) **Reconstruction calculated by weighted back-projection.**

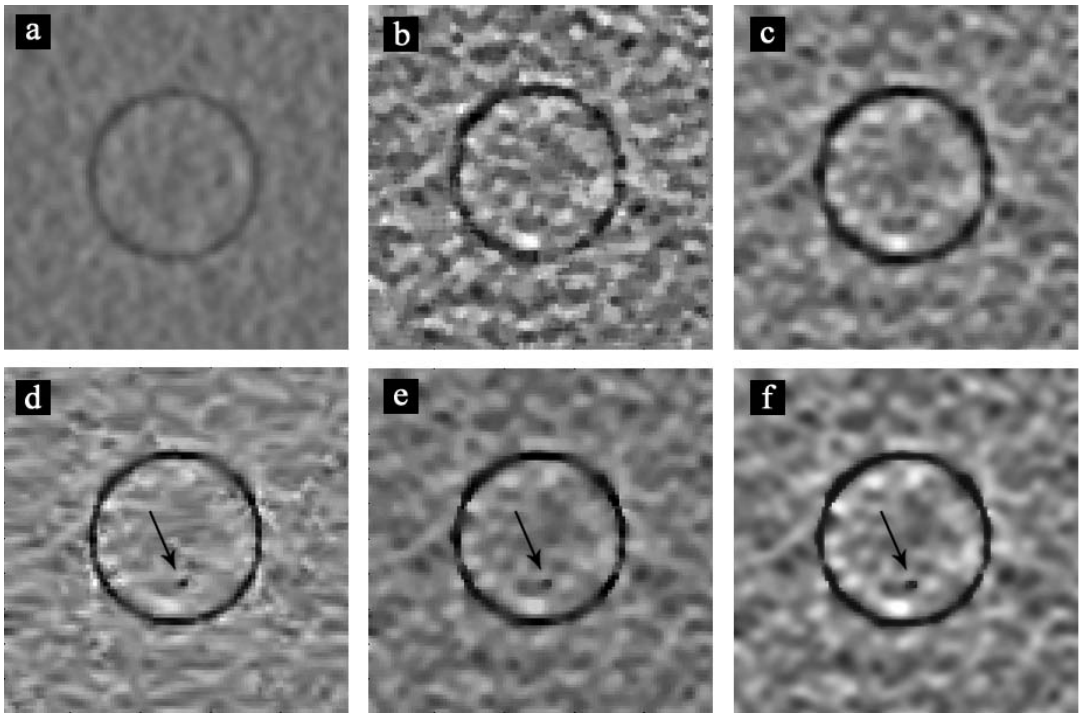

Figure 3.5: Simulated dataset filtered by *a*) **gaussian filter,** *b*) **median filter,** *c*) **EED,** *d*) **CED,** *e*) **hybrid diffusion. and** *f*) **scaling diffusion.**

tend to become thicker, losing their initial sharpness (Figure 3.5c). A "staircasing" effect is observed. Places with nearly the same gray value create a small plateau, which differs with a significant gradient from the environment. In the case of coherence enhancing diffusion the line features are preserved and enhanced, but the rest of the image is not smoothed enough (Figure 3.5d). The hybrid approach [Frangakis and Hegerl, 2001] combines the advantages of the latter two methods (Figure 3.5e). The scaling index based diffusion (Figure 3.5f) achieves a similar result. A significant noise reduction is achieved in the image with parallel preservation of high frequency features.

In order to measure the similarity between the original noise-free signal and the denoised version of the degraded signal, the Fourier Shell Correlation (FSC) was used. FSC compares two scenes i, j by the similarity of their correlation coefficients in rings or shells in the Fourier domain [Saxton and Baumeister, 1982]. This measure is aimed at deriving a score for similarity that is independent of the sampling density at each spatial frequency. The FSC is defined as:

$$FSC(f) = \frac{\sum\limits_{f' \in [f, f+\Delta f]} F_i F_j^*}{\sqrt{\sum\limits_{f' \in [f, f+\Delta f]} |F_i|^2 \sum\limits_{f' \in [f, f+\Delta f]} |F_i|^2}} \tag{3.8}$$

where f denotes the spatial frequency and Δf the thickness of the shell. $F_i(f')$ and $F_j(f')$ are the complex Fourier coefficients of the two images i and j in Fourier space and $*$ denotes the complex conjugate.

In Figure 3.6 the CCC for the different denoising methods are plotted and in Figure 3.7 a 3-D visualization of the denoising results is presented.

3.3.2 *Spiroplasma melliferum*

In the following, the scaling index based diffusion is applied to real tomographic data. The first example for the applicability of the hybrid diffusion approach is a *Spiroplasma melliferum* cell, the cytoskeleton of which consists of filamentous structures. The qual-

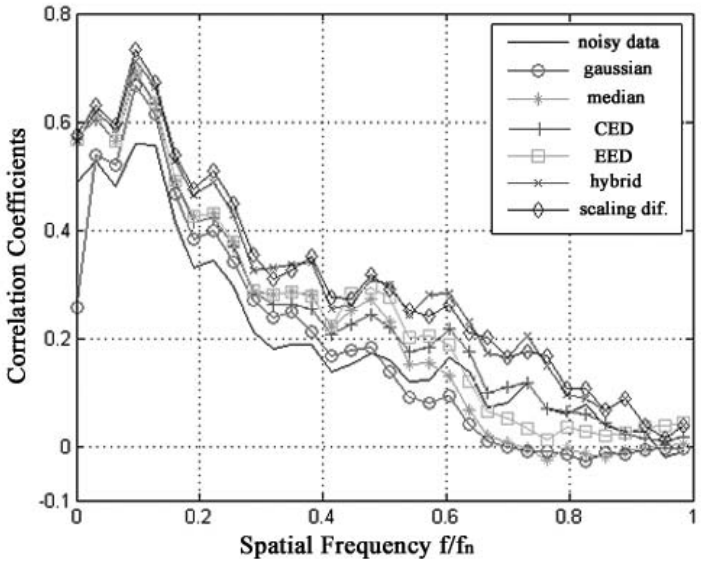

Figure 3.6: Plot of the FSC coefficients for the different denoising methods applied to the simulated dataset. f_n is the Nyquist frequency.

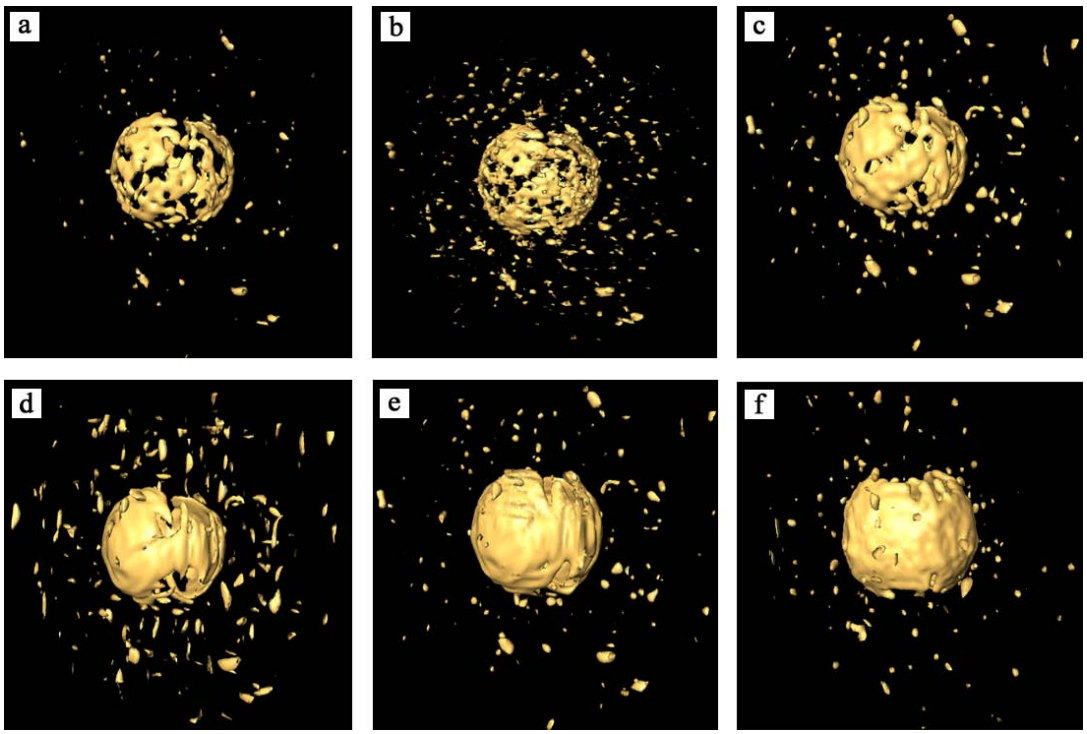

Figure 3.7: Iso-surface representation of the simulated data filtered by a) Gaussian filter, b) median filter, c) EED, d) CED, e) hybrid diffusion, and f) scaling index based diffusion.

ity of representation of the filaments will be used as a criterion for the judgement of the performance of the respective method. CED, EED, and the hybrid model are used for comparison.

The results after application of either EED or CED confirm the properties described in the previous example. As seen in Figure 3.8, EED produces the typical staircase effects, and the connectivity of the filaments is not improved or even preserved. It shows a behavior basically opposite to CED. In this case, almost no noise reduction has taken place; nevertheless, the connectivity of the filaments is improved significantly. The hybrid model combines a very good noise reduction of the background with a good representation of the filaments. The scaling index diffusion does not smooth the background so much, but it preserves the thin parallel filaments inside the cell better. 10 iterations were performed for each diffusion process.

3.3.3 Comparison of Scaling Diffusion with the Bilateral Filter

The Bilateral Denoising Filter was first proposed for denoising of electron tomograms by Jiang [Jiang et al., 2003]. The kernel of a bilateral filter is composed of an inner product of two low-pass filters in real space [Tomasi and Manduchi, 1998]. The first of these filters is a normal low-pass filter, which basically averages the neighboring pixel intensity values with decreasing weights for pixels at larger distances. The second one is also a type of low-pass filter, except that the weights for the neighboring pixels are derived from the pixel intensity value differences to the center pixel intensity value instead of geometric distances. Therefore, the larger the pixel value difference, the smaller the pixel's contribution during averaging. This second filter component characterizes the bilateral filter as non-linear, thereby distinguishing it from conventional Gaussian filters.

The scaling index method and the bilateral filter have one thing in common: both use the same similarity or affinity criterion between pixels. Affinity weights between two pixels (voxels) with index i and j are given by :

$$w_{ij} = exp\left\{-\frac{\|\mathbf{x_i} - \mathbf{x_j}\|^2}{2\sigma_D^2}\right\} exp\left\{-\frac{\|I_i - I_j\|^2}{2\sigma_I^2}\right\} \tag{3.9}$$

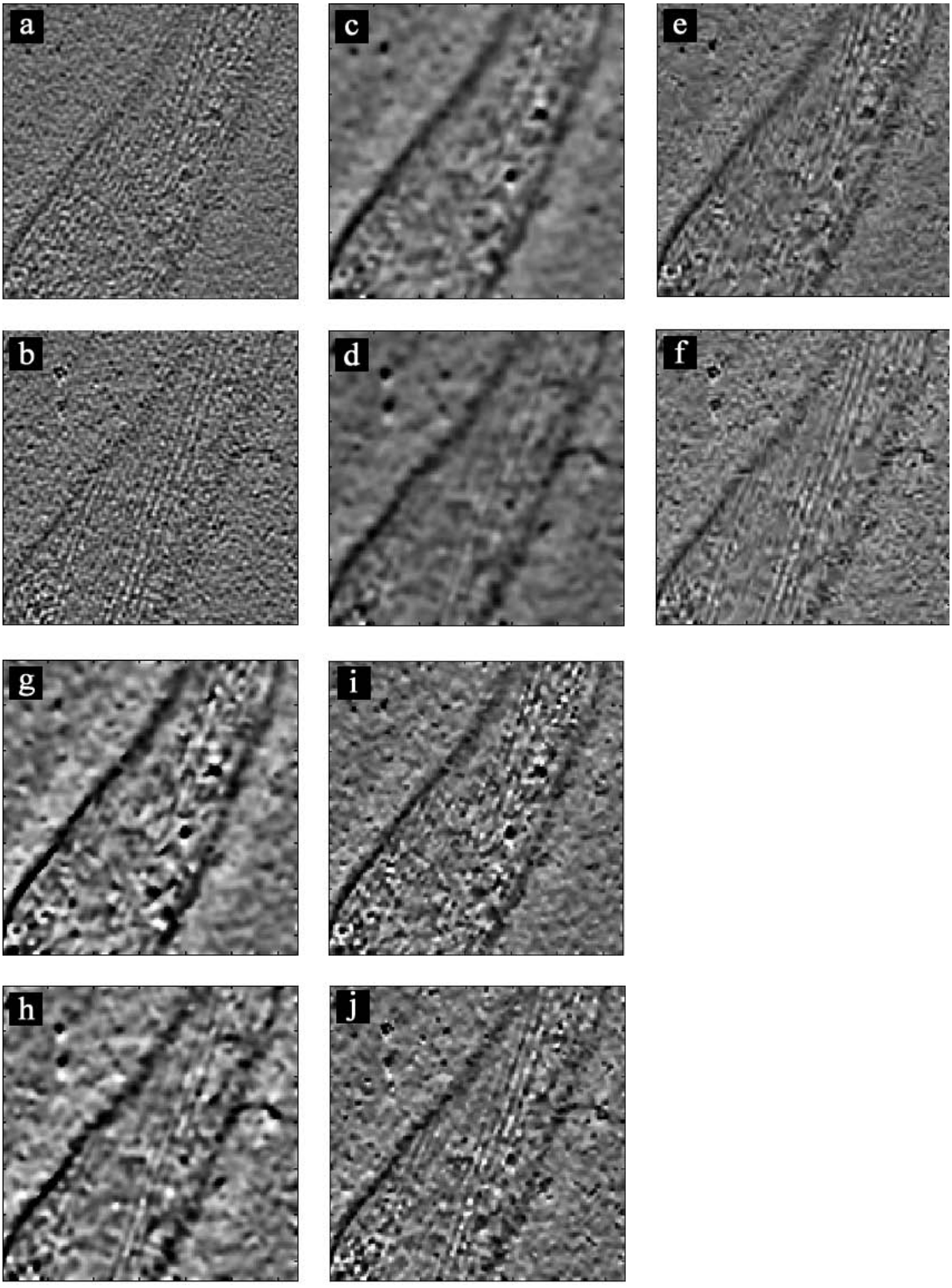

Figure 3.8: Filtering of *S. melliferum*. 2-D XY-slices of the original tomogram (a, b) filtered by $c, d)$ EED, $e, f)$ CED, $g, h)$ hybrid model, and $i, j)$ scaling diffusion.

where $\mathbf{x_i}$ = position, I_i = intensity of pixel i, σ_D and σ_I are range parameters for space and intensity to be defined by the user.

Scaling index can be realized with the use of these affinity weights (Equation 3.10). Scaling Index, as a filter response, could be considered as the locally weighted distance in 4-D space. On the other hand, the bilateral denoising filter also makes use of the same affinity weights in order to calculate the locally weighted intensity as filter response (Equation 3.11).

$$\alpha_i = \frac{\sum_{j=1}^{N} 2\left[\frac{\|\mathbf{x_i}-\mathbf{x_j}\|^{\mathbf{2}}}{2\sigma_D^2} + \frac{\|I_i - I_j\|^2}{2\sigma_D^2}\right] w_{ij}}{\sum_{j=1}^{N} w_{ij}} \tag{3.10}$$

$$\hat{I}_i = \frac{\sum_{j=1}^{N} I_j w_{ij}}{\sum_{j=1}^{N} w_{ij}} \tag{3.11}$$

Synapses

For the comparison of the two algorithms, two tomograms of excitatory synapses from a synaptosomal fraction were used. The reconstructions were calculated by weighted back-projection from projection images in the angular range from $-54°$ to $+62°$ with an increment of $2°$. In Figure 3.9 a 2-D XY slice of each tomogram is shown as are their respective filtered versions processed with the bilateral filter and scaling diffusion. In both examples, the filtered images processed with the scaling diffusion have sharper edges than the ones processed with the bilateral filter. The background appears to be much smoother in the case of scaling diffusion compared to the case of the bilateral filter. The bilateral filter calculations were done using the EMAN package with parameters $\sigma_1 = 2$ and $\sigma_2 = 0.12$.

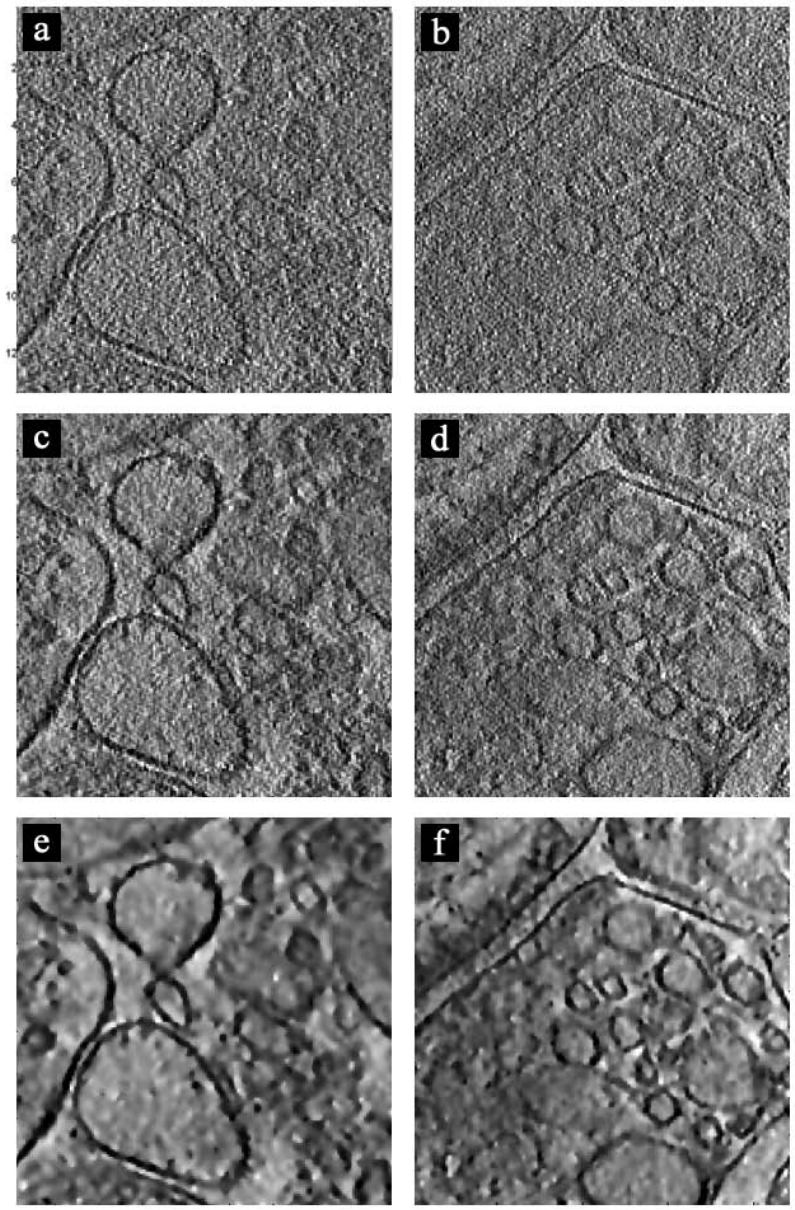

Figure 3.9: a, b)**XY-slices of two tomograms containing synapses,** c, d) **XY-slices of the tomograms processed with the bilateral filter, and** e, f) **XY-slices of the tomograms processed with scaling index based diffusion.**

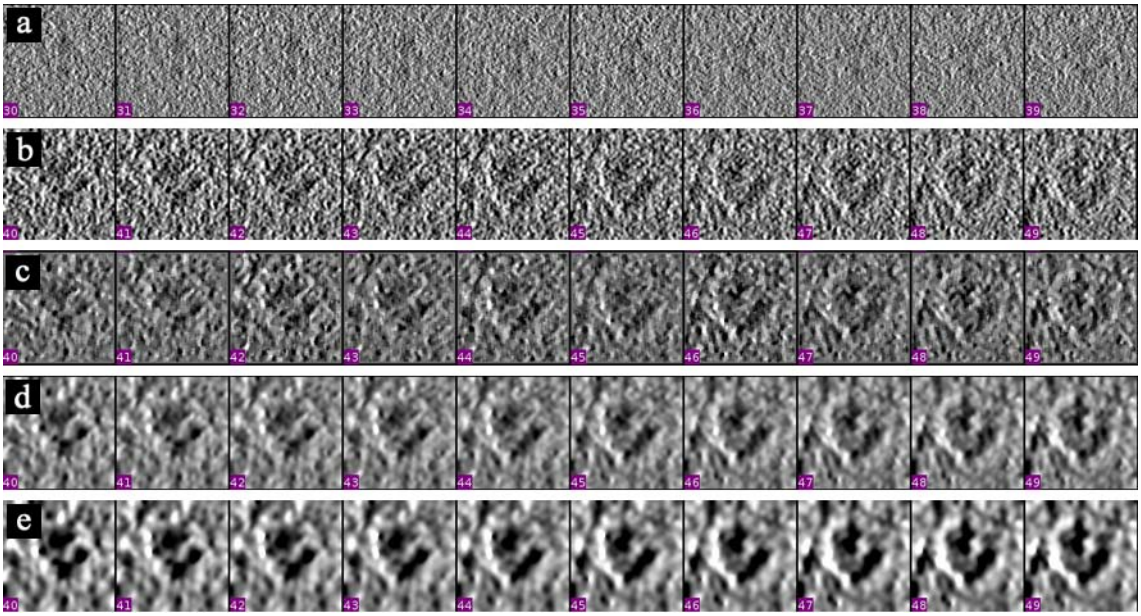

Figure 3.10: Consecutive 2-D XY-slices (numbers 40-49) from an individual ribosome complex denoised by different methods *a*) **original,** *b*) **Gaussian filter,** *c*) **median filter,** *d*) **bilateral filter, and** *e*) **scaling diffusion.**

Ribosome Complex

Direct measurement of the performance of denoising methods on real data is not possible because the true signal is unknown. Therefore, an indirect method to obtain quantitative comparisons is utilized. A certain class of biological specimen can be identically reproduced (such as specific macromolecular assemblies). In order to reveal the structural information of the specimen, a noise reduction procedure based on averaging is used. Instead of referring to a single copy of the specimen, a high number of identical copies of it (up to several thousand) is recorded. Averaging over multiple instances (after registering them to a common coordinate system) reveals the structural information (reference Saxton 1982). Each individual instance is considered as a single realization of the same statistical process. Therefore, adding n equivalent signals increases the SNR by a factor of $\sqrt{n}$ when assuming additive, signal-independent noise. The averaging technique can be considered as an ideal, artifact-free noise reduction method. However, the averaging method is not applicable to unique structures (e.g. cells). Nevertheless, reproducible structures in conjunction with averaging can be used in order to evaluate the performance of the denoising methods.

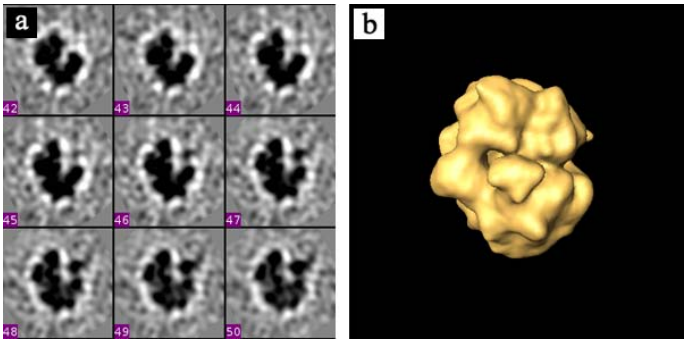

Figure 3.11: Reference of a ribosome complex created by averaging 400 chosen particles *a*) **consecutive 2-D XY-slices (numbers 42-50) of the averaged template,** *b*) **isosurface representation of the averaged template.**

In this example an individual ribosome complex was selected and denoised with Gaussian filter, median filter, bilateral filter and scaling diffusion filter (Figure 3.10). As reference, a ribosome complex that was created from averaging around 400 particles was used (Figure 3.11).

The denoised ribosomes were correlated to the averaged template and the FSC is presented in Figure 3.12. The scaling index based anisotropic diffusion outperforms the other denoising methods for almost all frequency signal components, and mainly for the range from 0.3 to 0.5.

3.4 Discussion

Imaging methods in biology can suffer from a high noise level, severely aggravating the visualization and interpretation of these data. Especially in CryoET, filtering techniques are necessary to allow visualization and interpretation of the information about the supramolecular organization of biological specimens. In this work, an algorithm for filtering cryotomograms based on AND has been described. The approach is based on a hybrid combination of EED/CED denoising that is driven by the structural information obtained with the scaling index method.

In all of the examples, the method performed very well in enhancing the signal. Edges were preserved while the background was smoothed, increasing the contrast. It clearly outperformed conventional methods like Gaussian filtering or median filtering. Since the

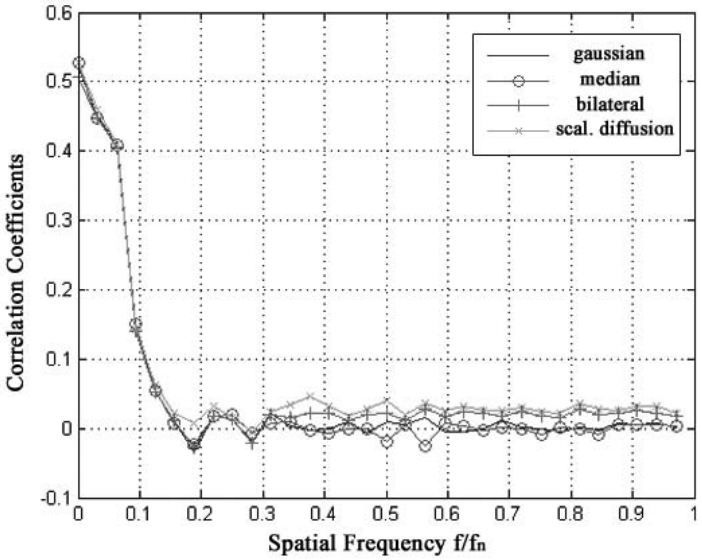

Figure 3.12: Plot of the FSC coefficients for the different denoising methods applied to the ribosome complex. f_n is the Nyquist frequency.

hybrid diffusion and the scaling index based diffusion are both are based on a combination between CED and EED, they performed equally well. Their difference is the way in which the decision for switching between the two types of diffusion is made. In the case of the hybrid model, a noise estimation is required from the user by defining a subvolume of the input volume that contains only noise. The decision about which diffusion type is going to be used is then based on the variance of this subvolume. The advantage in the case of the scaling index based diffusion is that this decision does not require any user interaction and is based on the local properties of the image/volume. All pixels/voxels with a scaling index value above a fixed threshold are identified as noisy pixels/voxels. In all of the examples presented in this work, the threshold value for the scaling index was set to 2.4 (the reader is refered to Section 3.1.5). As seen in the FSC diagrams, for the case of scaling diffusion, the best performance is obtained on data that predominantly contain low frequency signal components. The bilateral filter also outperformed the conventional methods, but compared to the scaling diffusion, produced poorer results as far as the contrast and edge preservation are concerned.

Chapter 4

Automated 3-D Image Segmentation using the Scaling Index Method

The segmentation of an image can be defined as its partition into different regions, such that the affinity between pixels belonging to the same region is higher than that between pixels of different regions [Russ, 1995]. Thereby, affinity must be quantified by defining adequate measures based on pixel properties. In a segmented image, the elementary picture elements are no longer pixels or voxels but connected sets of pixels. Once the image has been segmented, measurements are performed on each region and relationships between adjacent regions can be investigated. Image segmentation is therefore a key step towards the quantitative interpretation of image data.

The most straightforward and perhaps easiest way to perform two-dimensional image segmentation is to do it manually. Manual segmentation refers to the process whereby a user delineates by hand the desired Regions Of Interests (ROI) in an image. The human eye's ability to deliver information to the brain and the brain's capacity to process this information and make decisions based on it, enables manual segmentation to deal successfully with multiple selection criteria like continuity or similarity between objects. Except for the fact that such a procedure is very time consuming, it lacks reproducibility and objectivity. Especially in electron tomography, where the low-dose imaging conditions hamper the visualization capabilities, a manual segmentation may fail, especially with respect to the third dimension. Due to the high amount of noise or other overlapping objects, objects present in a tomogram can be distorted and no longer recognizable. This is why a computer-based 3D image segmentation is an important task in the context of electron tomography.

Denoising techniques are of great importance for any processing of cryo-electron tomograms. In the case of a very low SNR, any segmentation attempt must be preceded by a noise reduction procedure of the original map [Frangakis and Hegerl, 2002]. Segmentation can, in principle, also work on non-denoised tomograms but due to the difficulty to set correctly the segmentation parameters on noisy data, the segmentation result appears to be very noisy and contains many unwanted features.

Image segmentation techniques can be classified into two broad families: the contour-based and the region based approaches. The major difference between these techniques is the decision criterion: local vs. global. Contour-based techniques make local decisions (e.g. merge/split, stop/evolve), that can be proven premature. Region-based techniques make the decision by defining a global objective function. The advantage thereby is that decisions are made when information from the whole image is taken into account at the same time.

The use of scaling indices for segmenting 2D and 3D images is a new approach in the field of electron microscopy. This technique classifies the objects present in an image into different categories, according to the structure to which they belong. The traditional method of object separation is histogram thresholding, commonly used for surface rendering. Unfortunately there are many images in which no clear-cut definition of the histogram peaks corresponds to distinct objects in the image. With scaling index, not only are gray values and contrast between the feature and the environment taken into account, but also the structural surrounding, in order to improve the segmentation result.

The following paragraphs present an introduction to the segmentation algorithm and the efficient controlling of its parameters, a report on applications of the method to the structural analysis of frozen-hydrated cellular specimens, and a discussion concerning the handling and efficiency of the method.

4.1 Algorithm

4.1.1 Concept

A Scaling Index Based Segmentation method is proposed in order to improve visualization and interpretation of data obtained by electron tomography. Based on the interpretation of the scaling index as a measure for dimensionality, the pixels/voxels of an image/volume are subdivided into different categories according to the kind of structure to which they belong. In this case the weighted version of the scaling index [Räth et al., 2002] was preferred over the classical scaling index because of its simplicity with respect to parameter setting. Using the weighted scaling index method in conjunction with morphological operators, the approach was adapted to the field of electron microscopy, especially the 3-D density maps resulting from tomographic reconstructions of frozen-hydrated specimens, the latter with low-signal-to-noise ratio and missing-wedge distortions.

After the calculation of the scaling indices, appropriate thresholding creates binary masks for each object group. It can be possible that one has to calculate the scaling indices more than one time for different radii, if objects of different sizes are present. The selected radius determines each time the length scale on which the structures are analyzed and thus should be associated with the size of the structures to be identified. Unfortunately, the scaling-index values were influenced by the large amount of noise present in our data, such that many small and spurious features were created in the binary masks. A refinement in the resulting selection could be achieved by using morphological operators. By applying a subsequent combination of geodesic openings and closings it was possible to remove most of the unwanted objects that are present because of the very low SNR. The choice of the structuring elements used for the morphological operations depends on the structural characteristics of the objects to be segmented.

Controlling the parameters

The scaling indices depend on two parameters that must be defined by the user: i) the radius r and ii) the gray-value range of the image.

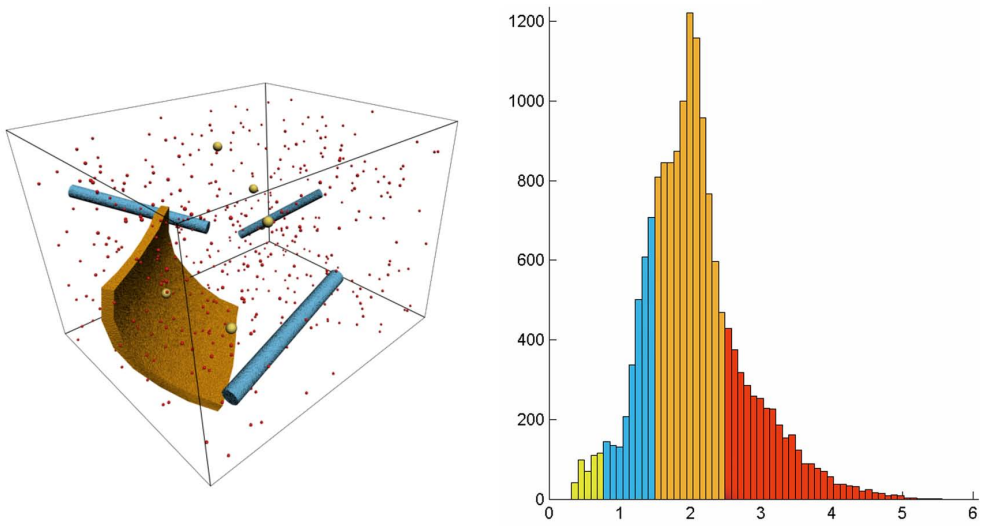

Figure 4.1: Objects are characterized and classified according to which kind of structure they belong. Different regions in the histogram correspond to different categories of objects.

The parameter r determines the length scale on which the structures are analyzed. Thus the selection of r should be chosen to match the size of the structures to be identified. The next example demonstrates the influence that the selection of r can have on the calculated scaling indices. The test data-set consists of a volume that contains linear structures of different thickness (Figure 4.2).

In Figure 4.3 the calculated scaling indices in both cases (with and without noise) are presented for $r = 2 \ldots 15$. It can be clearly seen that, in the beginning, when the radius is small, only the small and thin objects are identified as lines. (Lines assume a scaling index value around 1, and compared to the rest of the pixels, they appear darker). The remainder of the thicker objects were identified as homogeneous surfaces. As the radius increases, the thin objects are treated as small, noisy structures (high scaling index values) and the thicker objects are progressively recognized as broad lines.

By thresholding the scaling indices, it is possible to classify the objects according to their thickness. In the case of no noise, a threshold from 0.8 to 1.3 was selected for $r = 2$. As expected, only the thinnest lines were selected (Figure 4.4a). For the case with noise, a threshold from 0.8 to 1.3 was selected for $r = 6$ (Figure 4.4b). The two thick lines were

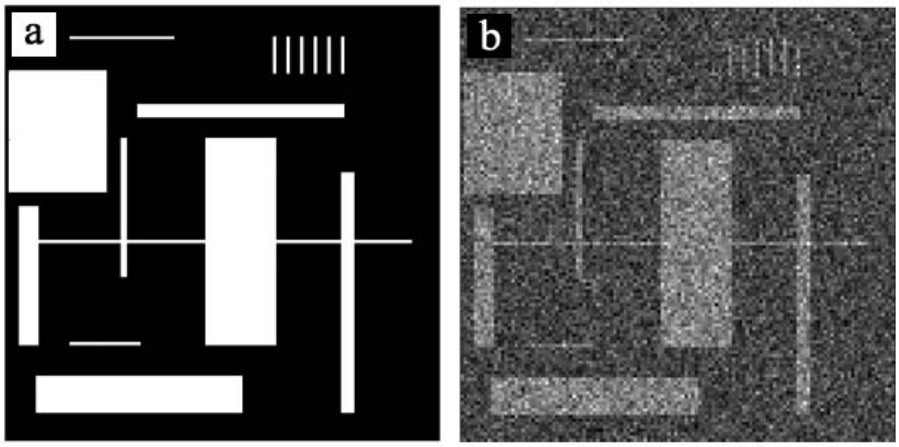

Figure 4.2: Test data-set that contains rectangular objects with different thicknesses.

identified correctly but the performance of the identification procedure is unsatisfactory. The borders of the objects seem to be poorly defined and there are also other, isolated pixels present in the image, identified falsely as similar objects. The solution to noisy cases is filtering of the data prior to calculating the scaling indices. By doing so in the particular example (nonlinear anisotropic diffusion was used for filtering) it was possible to acquire a more representative segmentation of the lines.

The second parameter is a scaling factor for the density values. As illustrated in Figure 4.6, the scaling factor could be described as a smoothing factor. In our applications, the whole range of density values was scaled to values ranging from 0 to 128. This choice is a compromise between WSI-maps that are smoothed too much, and those with too many details, obtained by smaller or larger scaling, respectively.

4.1.2 Morphological Operators

Morphological operators aim at extracting relevant structures of the image considered as a set through its subgraph representation [Soille, 2003]. This is achieved by probing the image with another set of known shape called structuring element (SE). The shape of the SE is usually chosen according to some *a priori* knowledge about the geometry of the relevant and irrelevant image structures. "Irrelevant structures" implies either noise or

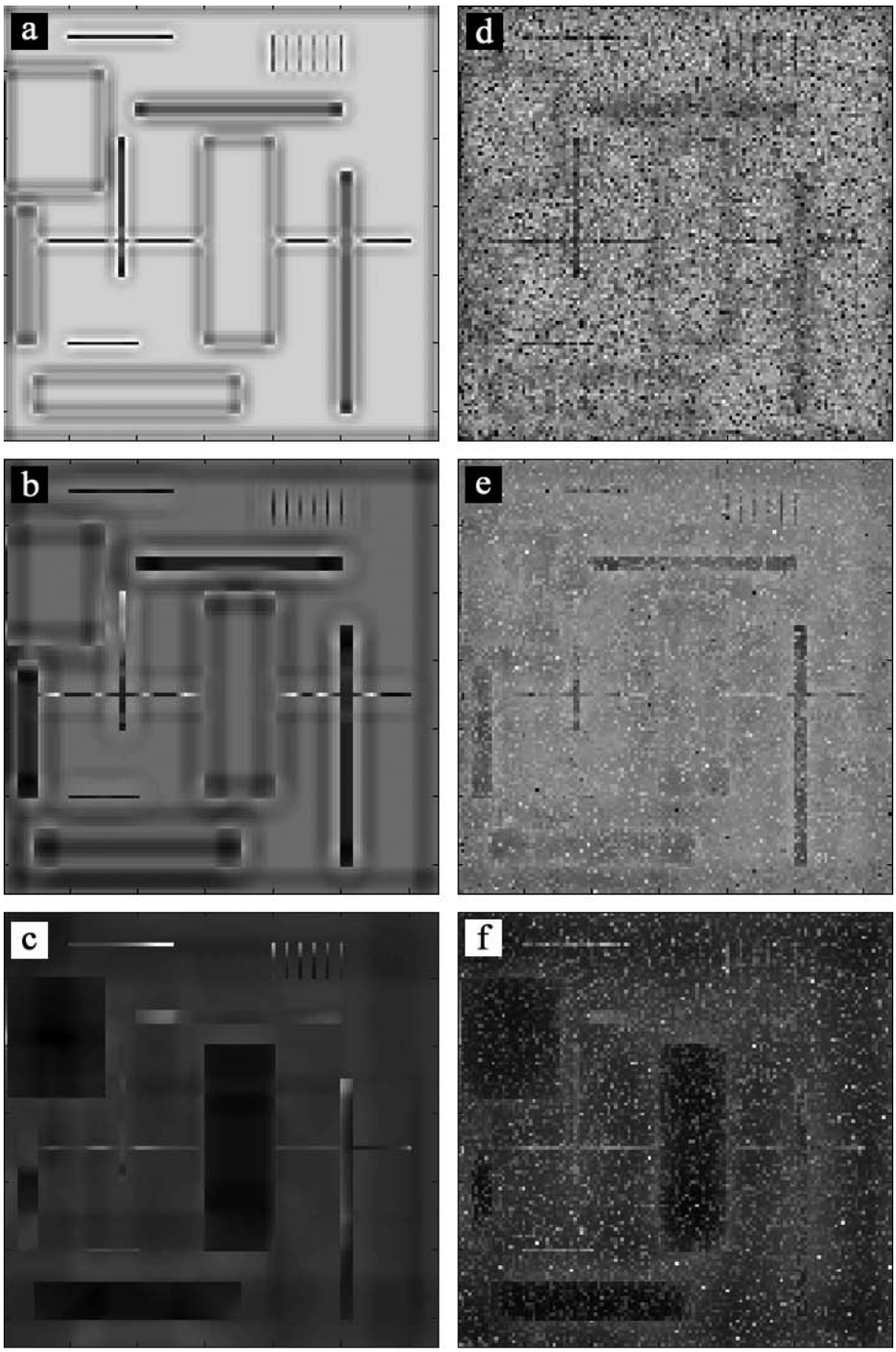

Figure 4.3: Calculated scaling indices of the image 4.2a for radii $a)$ $r = 2$, $b)$ $r = 6$, $c)$ $r = 15$, **and for image 4.2b for the same radii.**

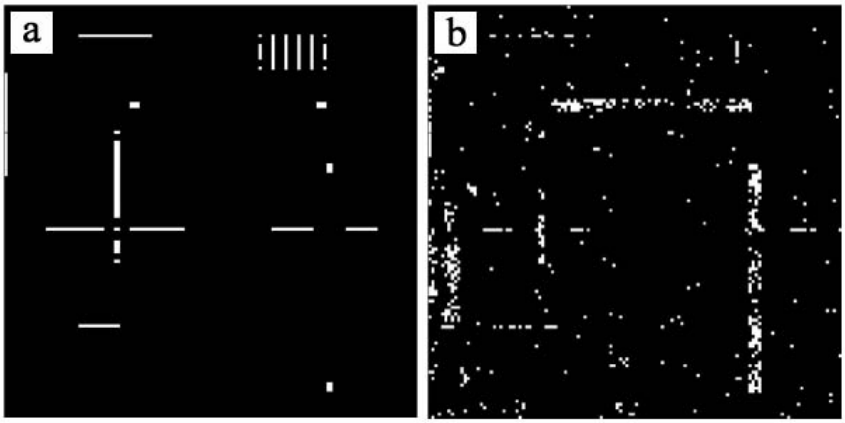

Figure 4.4: By calculating the scaling indices for $r = 2$ and thresholding them from 0.8 to 1.3 it was possible to segment the thin lines. In the case of noise the result is quite unsatisfactory.

Figure 4.5: Filtering of the data prior to calculating the scaling indices improves the detection ability of the algorithm and refines the segmentation result.

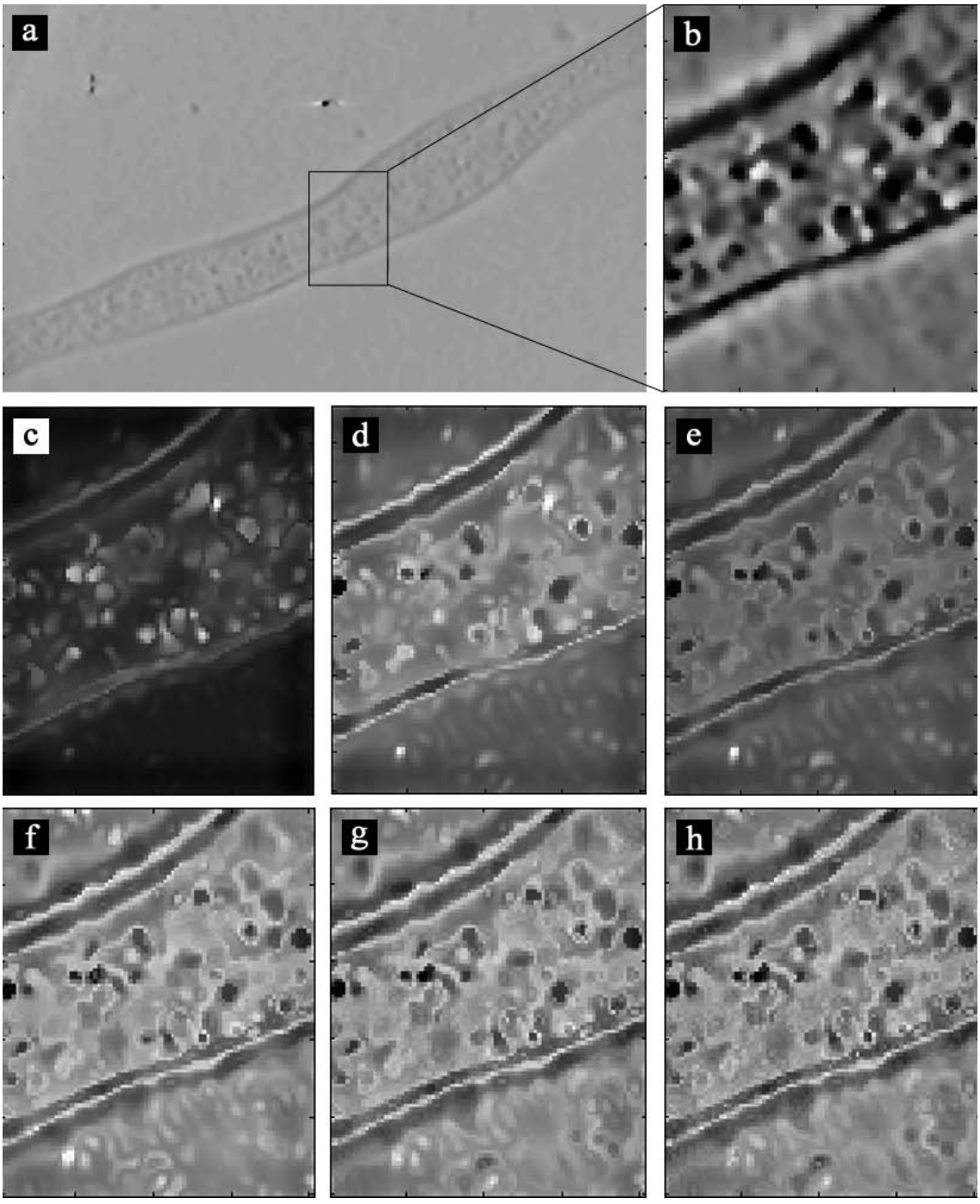

Figure 4.6: Different scalings affect the calculated scaling indices *a*) **2-D XY slice from a *Spiroplasma melliferum* tomogram,** *b*) **2-D XY-slice of a smaller subvolume of the tomogram filtered heavily with N.A.D. Calculated scaling indices with** $r = 10$ **for scaling** *c*) **[0...32],** *d*) **[0...64],** *e*) **[0...128],** *f*) **[0...256],** *g*) **[0...512], and** *h*) **[0...1024].**

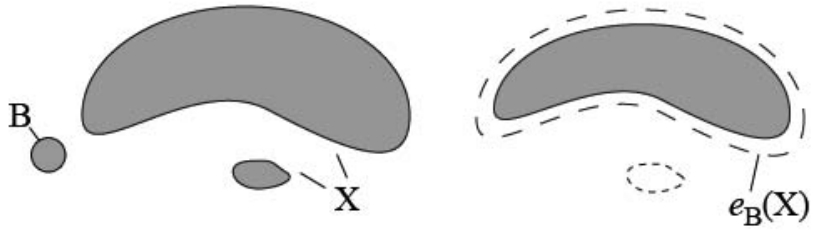

Figure 4.7: Erosion ε of a set X by a disc B. The smallest component of X disappeared since B never fits this component.

objects we would like to suppress. A SE is simply a small set used to probe the image under study. Most morphological operators require the definition of an origin for each SE. this origin allows the positioning of the SE at a given point or pixel : a SE at point x means that its origin coincides with x. In our case binary, or so-called flat SE's were used, which means that no weights are associated with pixels of the SE's. The shape and size of the structuring element must be adapted to the geometric properties of the image objects to be processed.

Erosion

The erosion of a set X by a structuring element B is denoted by $\varepsilon_B(X)$ and is defined as the locus of points $\mathbf{x}$ such that B is included in X when its origin is placed at $\mathbf{x}$:

$$\varepsilon_B(X) = \{\mathbf{x} | B_{\mathbf{x}} \subseteq X\} \tag{4.1}$$

This is illustrated in Figure 4.7 for a 2-D image. Equation 4.1 can be rewritten in terms of an intersection of set translations, the translations being determined by the SE:

$$\varepsilon_B(X) = \bigcap_{\mathbf{b} \in B} X_{-\mathbf{b}} \tag{4.2}$$

Dilation

The dilation is the dual operator of the erosion. The dilation of a set X by a structuring element B is denoted by $d_B(X)$ and is defined as the locus of points $\mathbf{x}$ such that B hits X

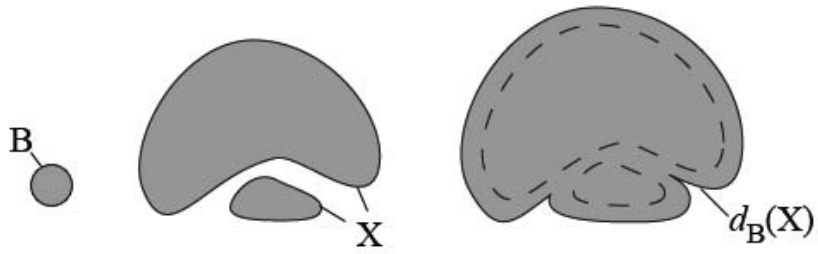

Figure 4.8: Dilation d of a set X by a disc B. The two connected components of X are connected by dilation: B always hits X when it is placed in the channel separating the particles.

when its origin coincides with $\mathbf{x}$:

$$d_B(X) = \{\mathbf{x} | B_{\mathbf{x}} \bigcap X \neq \emptyset\} \tag{4.3}$$

This is illustrated in Figure 4.8 for a 2-D image. Equation 4.3 can be rewritten in terms of a union of set translations, the translations being determined by the SE:

$$d_B(X) = \bigcup_{\mathbf{b} \in B} X_{-\mathbf{b}} \tag{4.4}$$

According to the geometric properties of the objects to be processed in the image, a suitable choice of the SE would lead to the classification of the objects according to their shape and size. Erosion with the suitable SE would suppress all objects that are irrelevant to the SE and then dilation with the same SE would reconstruct the eroded objects. Sometimes after the dilation, the objects of interest are bigger than they were before performing any morphological operators. In order to avoid creating such artifacts, geodesic dilation can be used [Soille and Talbot, 2001]. Geodesic dilation involves two images: a marker image and a mask image. By definition, both images must have the same definition domain, and the mask image must be greater than or equal to the marker image. In a geodesic dilation, the image if first dilated with the SE and then the result is forced to remain below the mask image. The mask image acts therefore as a limit to the propagation of the dilation of the marker image.

4.1.3 Implementation of the Algorithm

For the calculation of the scaling indices, a self-developed program in language C was used. In the case of very big tomograms (with dimensions at least 512x512x256 voxels), a

parallelized version of this program was developed by using the Message Parsing Interface (MPI). All morphological operations, the watershed segmentation, as well as the texture analysis were performed with the use of MATLAB.

4.2 Segmentation Results

In electron tomography, there are mainly two tasks for segmentation. The first task is to achieve a foreground-background separation, e.g. when a whole cell has to be separated from its environment (ice, carbon foil, gold bead, etc.). The second task is to achieve the separation of a 3D image into distinct groups with similar properties e.g. gray values, or in other words, to group pixels or voxels into subsets that correspond to meaningful regions or objects.

The proposed method for automatic segmentation, according to the size chosen for the parameter r, can be used either in the sense of a foreground-background segmentation (example: *Spiroplasma melliferum* segmentation), or with hierarchically descending r, for the segmentation of smaller features down to a molecular level (example: *Dictyostelium* segmentation).

4.2.1 Simulated Tomographic Data

In order to study the properties of the segmentation algorithm, it was applied to a simulated tomographic reconstruction of a hollow sphere with blobs of different size inside the sphere. The gallery in Figure 4.9a shows consecutive slices along the z-axis through the tomogram which was calculated by weighted back-projection from projection images in the angular range from $-60°$ to $+60°$ with an increment of $6°$. Deformation and contrast fading on the top and bottom of the sphere are due to the missing wedge. For these data, separating the sphere from its contents would be a typical task for segmentation corresponding to the segmentation of the membrane of a cell. Thresholding the gray levels of the reconstructed density map does not provide the desired result. However, appropriate thresholding of the calculated scaling indices clearly separates the sphere from its contents (Figure 4.9d). By calculating the scaling indices for a radius that matches the size of the smaller objects, the internal objects are correctly segmented. In Fig. 4.9e,f the tomogram is shown by surface

rendering. Due to the missing wedge, the sphere is open on its top and bottom and slightly deformed.

4.2.2 *Spiroplasma melliferum*

This new approach to image segmentation was applied to a tomographic reconstruction of an ice-embedded cell of the bacterium *Spiroplasma melliferum* [Kürner et al., 2005] with the aim to separate the body of this bacterium from its environment. The intensity values of the body of the bacterium were distributed over the same range as those of the environment and simple thresholding of the tomogram even after denoising could not result in an acceptable segmentation (see Figure 4.10a,b). The result was a map of islands with higher occurrence inside of the bacterium but no compact volume defining the body of the bacterium as a whole. However, appropriate thresholding of the corresponding scaling index image clearly separates the body, although many small spurious features are still visible outside the cell as shown in Figure 4.10c. Most of these can be removed by subjecting the scaling index map to four cycles of combined erosion and dilation operations (Figure 4.10d). The few remaining structures outside are concentrated on the top and bottom of the tomogram, reflecting the well-known missing wedge problem of electron tomography. After the separation of the bacterium from its environment, further processing was performed in order to segment the membrane. By using erosion and dilation with an anisotropic structuring element, in our case a linear structure in many different orientations, the membrane could be isolated from the rest of the bacterium body (Figure 4.10e,f). The resulting mask could then be used to segment the bacterium for iso-surface representation (Figure 4.11).

In order to demonstrate the efficiency of SIBS, the electron tomogram was also subjected to alternative segmentation methods, namely watershed segmentation and an approach based on texture analysis. In Fig. 1g the calculated label matrix is shown, identifying the watershed regions. Due to the high amount of noise present in the tomogram, the result of the watershed segmentation is the partition of the tomogram into a great number of segmented labels. Thresholding of those labels (Figure 4.12a,b) will not produce the desired result, which is separating the bacterium body. Although watershed segmentation is a powerful technique for the separation of touching objects, is not so suitable for foreground-

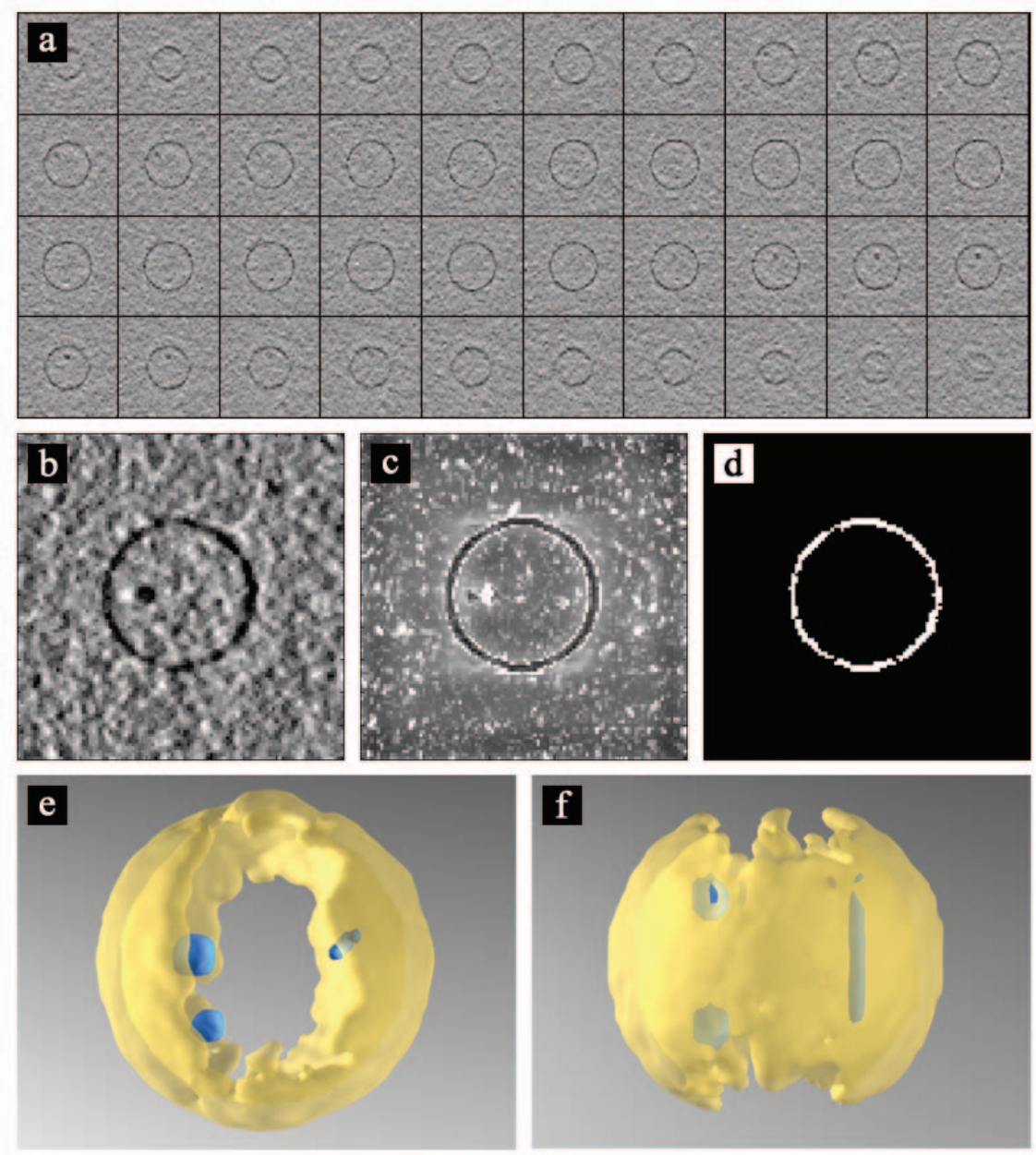

Figure 4.9: Segmentation applied to a simulated electron tomogram of hollow sphere with two blobs and a line inside. *a*) **the gallery of slices through the 3D reconstruction exhibits the artifacts arising from the missing wedge,** *b*) **slice of the filtered tomogram,** *c*) **calculated scaling indices,** *d*) **mask obtained by thresholding the scaling indices, and** *e*) **surface-rendered representation of the segmented volume and the separated features that were contained inside.**

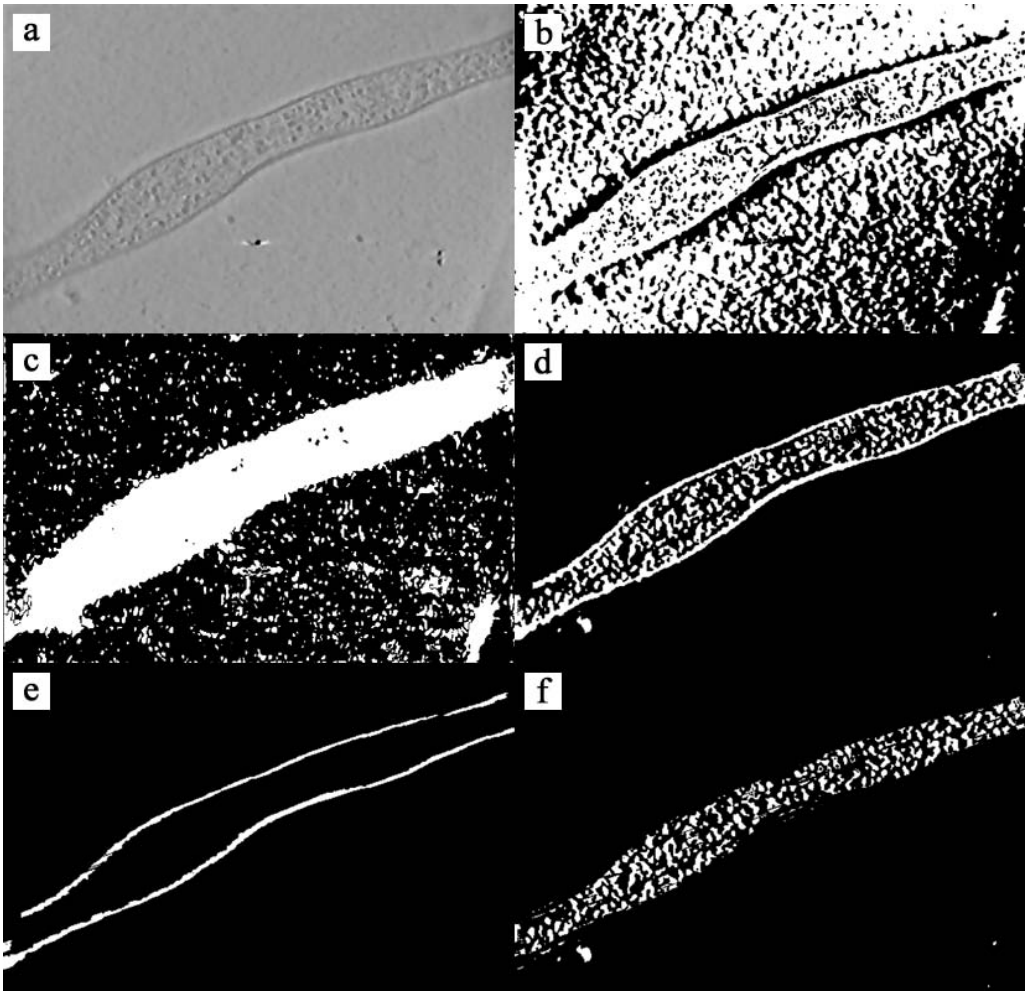

Figure 4.10: Segmentation of *S. melliferum* a) 2-D XY-slice of the original tomogram after denoising with N.A.D., b) segmentation by simple thresholding of the gray-values, c) calculation of the scaling indices for $r = 20$, d) binary mask after thresholding of the scaling indices and processing with morphological operators, e, f) further processing with anisotropic morphological operators in order to isolate the membrane from the rest of the bacterium body.

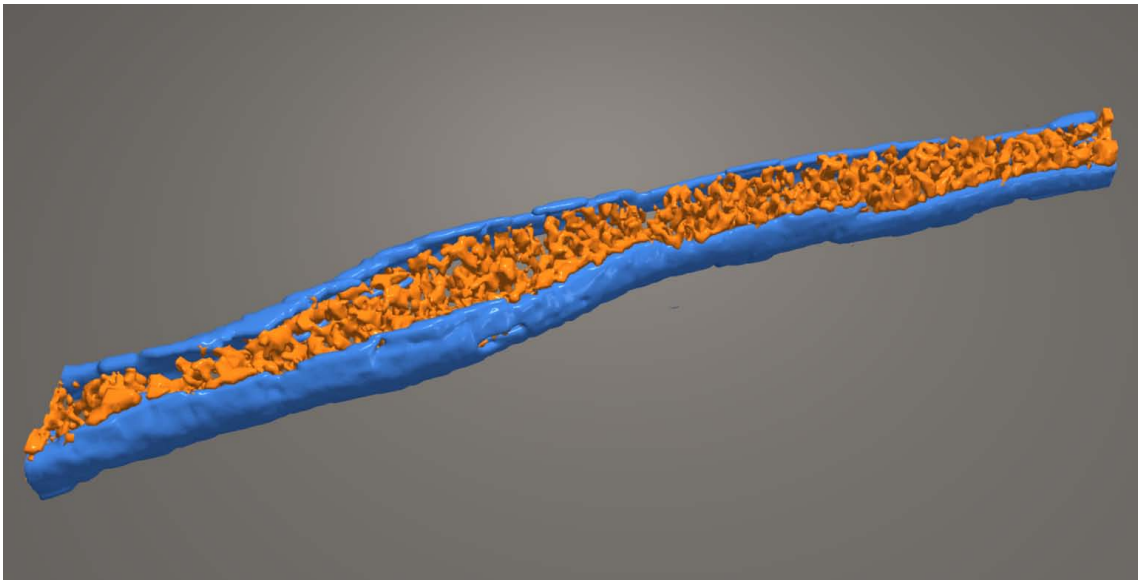

Figure 4.11: Iso-surface representation of *Spiroplasma melliferum*.

background segmentation of whole cells.

Finally we tried to segment the bacterium by using texture analysis. In our case a technique was used that is based on the local range of the intensities of the image. Such statistical measures provide information about the local variability of the intensity values of pixels in an image or voxels in a volume. As previously stated, simple thresholding does not separate the bacterium body from its environment because many gray levels that describe the bacterium body occur also in the background, due to the low contrast. On the other hand, the texture of the background appears much smoother when compared to the rough texture of the bacterium body, which means that the local range of values in the neighborhood of a background pixel will be smaller than that in areas of rough texture. As shown in Figure 4.12c, the bacterium body is separated from its environment, but the selection is not as compact as when processed with the scaling index. The presence of small spurious features in the background can be explained in terms of the high amount of noise present in the tomogram. Again, these random features can easily be eliminated by processing the selection with morphological operators, as shown in Figure 4.12d. The analysis was performed in 3-D.

Two further *S. melliferum* tomograms were segmented successfully by SIBS. The first

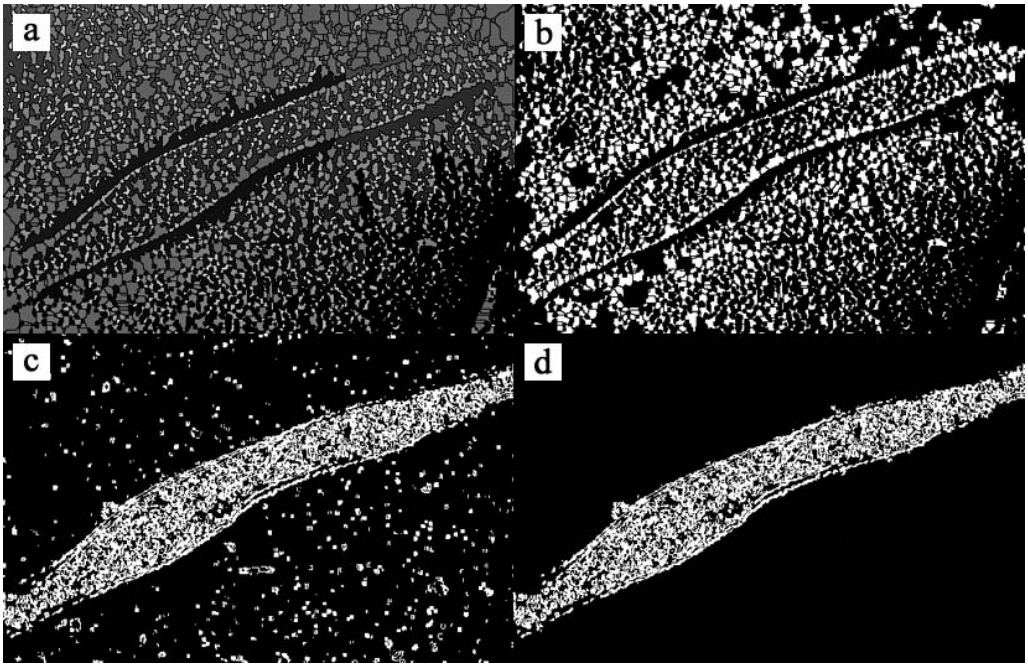

Figure 4.12: Alternative segmentation algorithms for *S. melliferum* a) calculated watersheds, b) binary mask from image in (a), c) texture analysis based on the local range of the intensities of the volume, d) binary mask after processing with morphological operators.

tomograms shows two *S. melliferum* cells adjacent to each other (Figure 4.13). By following the same segmentation strategy, the cells were separated from their environment and then, by using anisotropic morphological operations, the membranes could be isolated from the rest of the bacterium bodies. Finally, the segmented bacteria were visualized by iso-surface representation (Figure 4.14). In the second tomogram, there were two segmentation tasks. First, to isolate the membrane from the remaining body of the bacterium (Figure 4.15b), which was done by using a similar segmentation procedure as in the previous examples, and second to identify the globular complexes that were located in the inner part of the body of the bacterium [Ortiz et al., 2006] (Figure 4.15c). The complexes could be identified by calculating the scaling indices with a radius that would match their size ($r \approx 5$ voxels). The number of the ribosomes identified was very useful to get an overview of approximately how many ribosomes are located in the bacterium and can be used as input for other methods like template matching and cross correlation.

Figure 4.13: Segmentation of *S. melliferum* a) **2-D XY-slice of the original tomogram after denoising with N.A.D.,** b) **segmentation by simple thresholding of the gray-values,** c) **calculation of the scaling indices for** $r = 15$, d) **thresholding of the scaling indices, and** e) **final segmentation mask.**

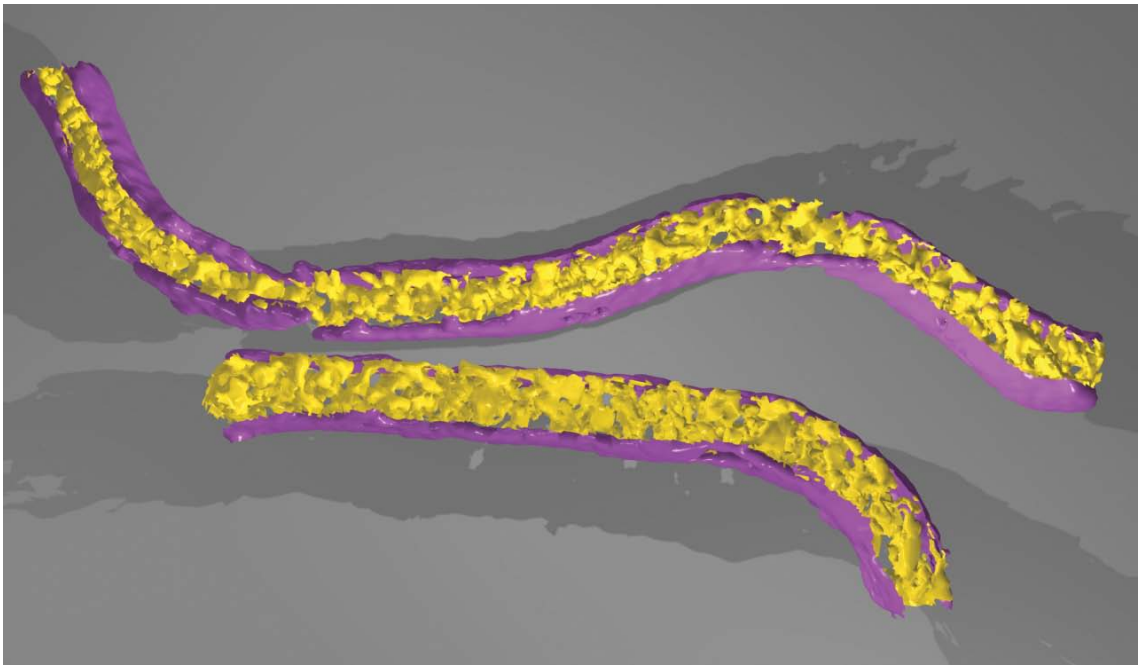

Figure 4.14: Iso-surface representation of the *S. melliferum* presented in Figure 4.13.

4.2.3 *Dictyostelium discoideum*

The second example presents the segmentation of a peripheral region of a *Dictyostelium discoideum* cell as obtained by tomographic reconstruction of a frozen-hydrated specimen (Figure 4.16). Peripheral region of such cells were successfully studied by cryo-electron tomography, with the aim to visualize the cytoskeleton in such regions [Medalia et al., 2002]. Since the cortical regions of this slime-mold are mainly enriched with actin filaments it is likely that most of the filamentous structures visualized are composed of actin. The globular molecular structures embedded within the cytoplasm are consistent with the size of ribosomes, although independent proof is lacking. Automatic segmentation aims to separate the complexes from filamentous structures.

A semi-automatic but fully parameter-controlled segmentation of the same data was performed in three steps (Figure 4.19). There were mainly three categories of objects present in the tomogram: vesicles, globular complexes and filaments. By calculating the scaling indices with radii that would match their dimensions, we obtained three different masks, one for each category. Small spurious features or false identified objects could easily be

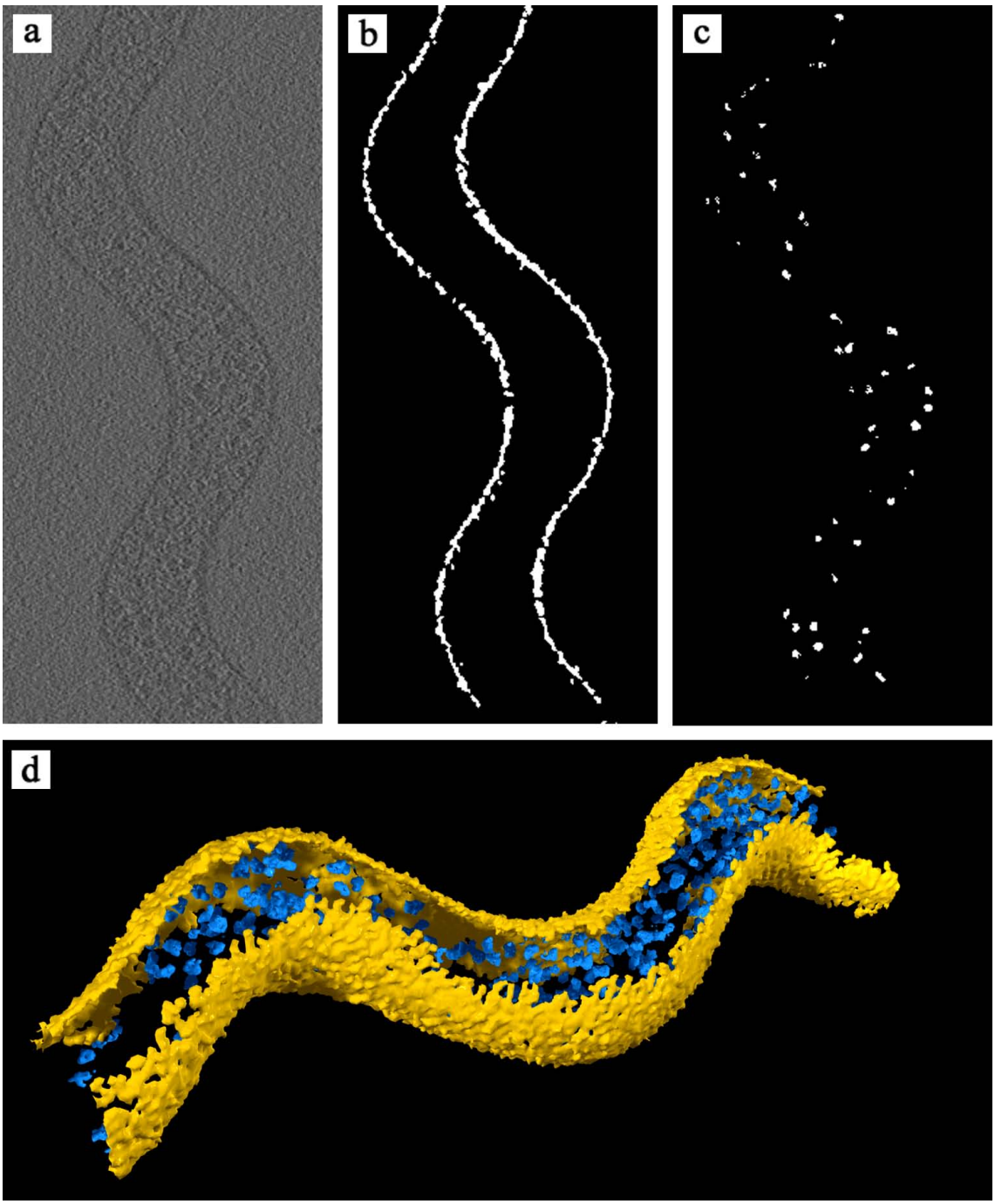

Figure 4.15: Segmentation of *S. melliferum*. *a*) **2-D XY-slice of the original tomogram after denoising with N.A.D.,** *b*) **segmentation of the membrane by SIBS,** *c*) **localization of the complexes present in the tomogram by SIBS, and** *d*) **iso-surface representation of the segmented bacterium.**

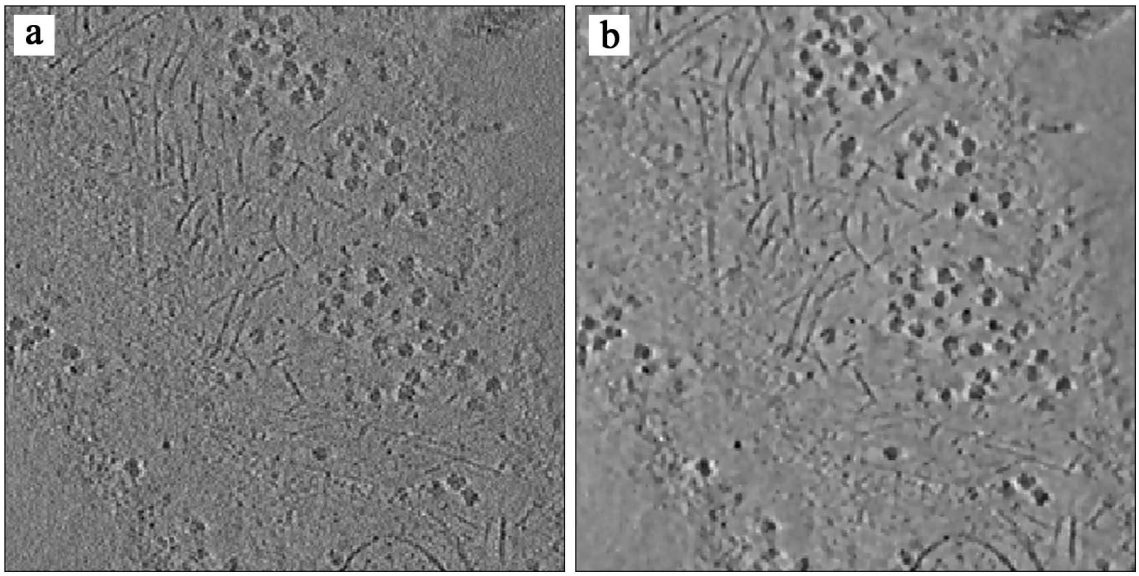

Figure 4.16: XY-Slice of the tomographic reconstruction of *D. discoideum* a) original data, b) after denoising with non-linear anisotropic diffusion.

removed by anisotropic morphological operators, because of the different dimensionality of the objects (linear structures for filaments, point-like structures for globular complexes and surface structures for vesicles).

In the case of manual segmentation, where it would be extremely time consuming to segment separately every filament and every complex present in the tomogram, an area segmentation was preferred. The binary mask of the filaments obtained by manual segmentation is actually a 2-step process. The first step consists of a general selection of the area, where filaments can be visually detected. In the second step, the filaments are segmentted by simple thresholding. On the other hand, the mask generated by SIBS is a feature-specific segmentation. As seen in Figure 4.17, in the case of the manual segmentation, additional complexes that are included in the selection area will be visualized, whereas in the automatic segmentation case, only linear structures are segmented and visualized. In Figure 4.18, a 3D visualization of both segmentations is shown, where a close similarity between the manual and the automated segmentation is evident.

Astonishing aspects of the potential given with the scaling index method are demonstrated by further processing of the mask separating the filaments. Calculating the scaling index

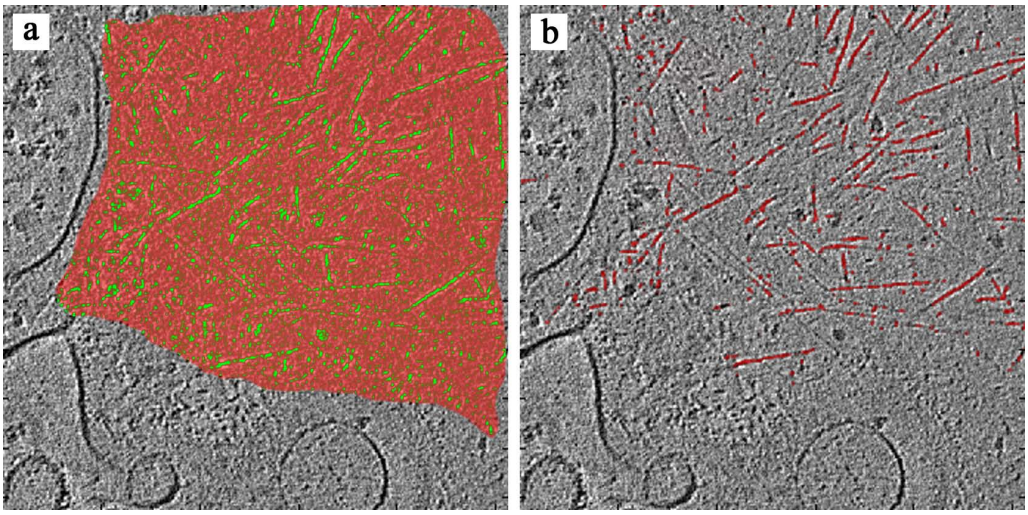

Figure 4.17: General selection compared with specific feature selection *a)* **the red marked area corresponds to the manually selected mask of the filaments. Appropriate gray-value thresholding results in the final segmentation of the filaments (area marked with green color),** *b)* **automatically selected mask of the filaments.**

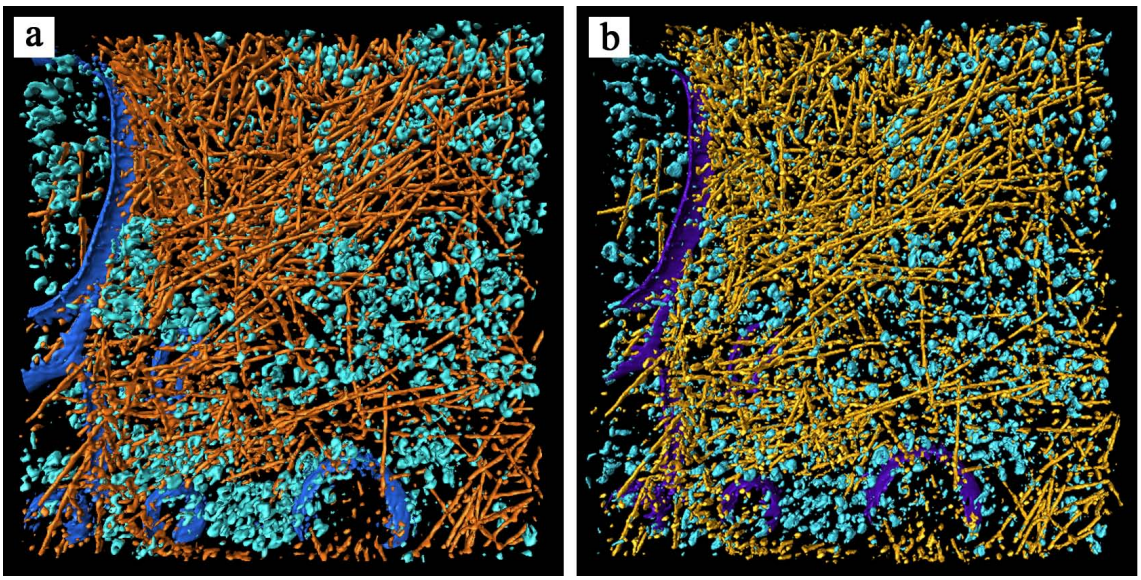

Figure 4.18: Iso-surface representation of the segmentation of *D. discoideum*. *a)* **manual segmentation, and** *b)* **SIBS.**

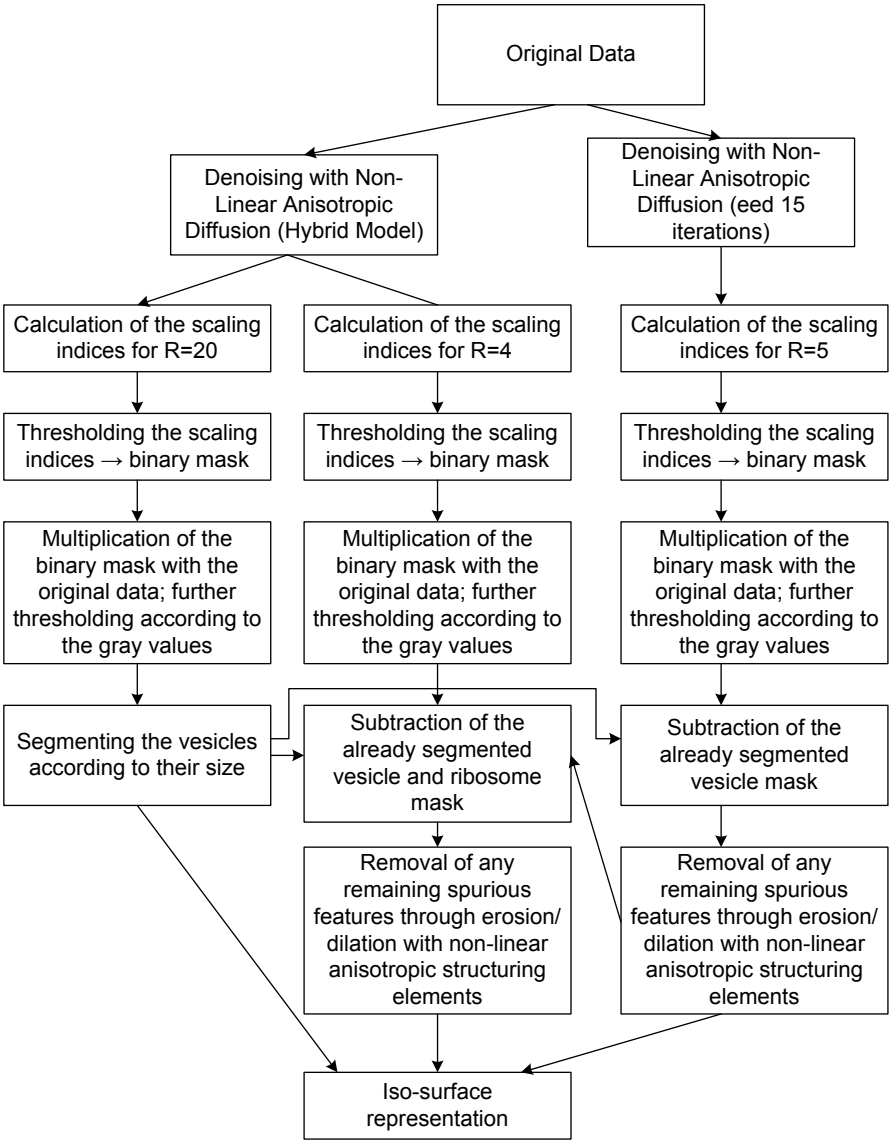

Figure 4.19: Flow Diagram of the segmentation of *D. discoideum*.

Figure 4.20: Iso-surface visualization of the branches and cross-links detected.

of a scaling index map may appear peculiar. In the present case however, the result is very useful because this "second order" map presents the structural features with higher fidelity. As expected, the scaling indices had the value of one ($\alpha \approx 1$ along lines originally defined by the filaments, but at points where two filaments are connected, the scaling index values were higher. By setting an appropriate threshold, we could isolate the connections. We found a total of 76 connections and all the connected filaments are visualized by an iso-surface representation in Figure 4.20. By analyzing the neighborhood of all connections in the planes defined by the pairs of connected filaments, we classified them into 24 branches and 52 crossings. Regarding the 8 neighboring pixels around a connection point, branches are defined by 3 or less pixels and crossings by 4 or more pixels, each with a value of one. This analysis could be extended by a further investigation of the angles occurring for these connections. The existence of a variety of connections controlled by corresponding protein complexes is well known in biology. The procedure described here could help to localize and classify such structures in an automatic and more reproducible manner.

4.2.4 *Ignicoccus*

SIBS was used in order to process a tomogram where a *Nanoarchaeum equitans* cell is closely placed to a *Ignicoccus* cell [Briegel, 2005] (Figure 4.21). It is believed that these two cells interact via thin filaments that traverse their membranes.

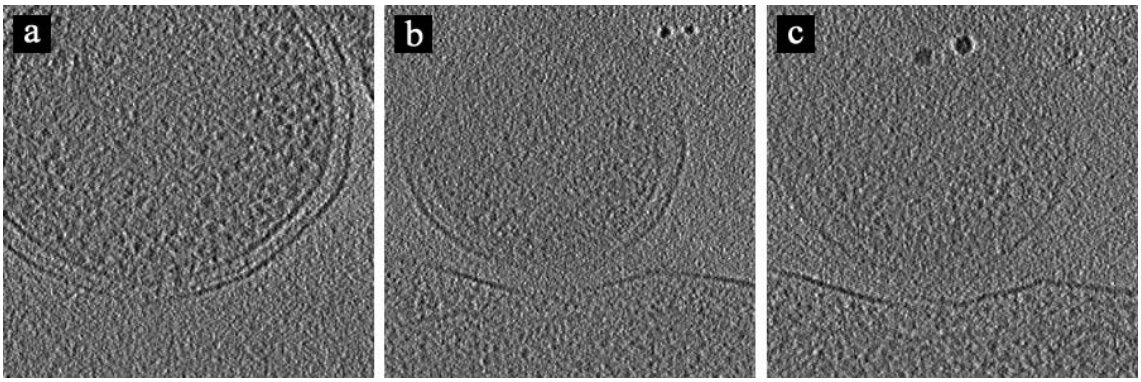

Figure 4.21: Different XY-slices of the tomogram showing in a) the double membrane of the *Nanoarchaeum equitans* cell and in b, c) the membrane of the *Ignicoccus* cell.

In order to study the interactions between these two cells, it was very important to locate and separate their membranes. Due to the missing wedge the borders were diffusing in some points and, hence the need for an automatic computer-based method in order to segment them. By calculating and thresholding the scaling indices, we could isolate the objects that had a surface-like structure (membranes) from the rest. The created binary masks were then multiplied with the original data and visualized by iso-surface representation as shown in Figure 4.22.

4.2.5 *Rhodopseudomonas viridis*

Rhodopseudomonas viridis is an anaerobic, photosynthetic bacterium which forms lamellar, partially stacked intracytoplasmic membranes (ICMs) called thylakoids, that contain the photosynthetic core complexes. According to the amount of time that the bacterium is exposed to light, these thylakoids change their shape and size. CryoET was performed in order to visualize and study the formation of the thylakoid membranes.

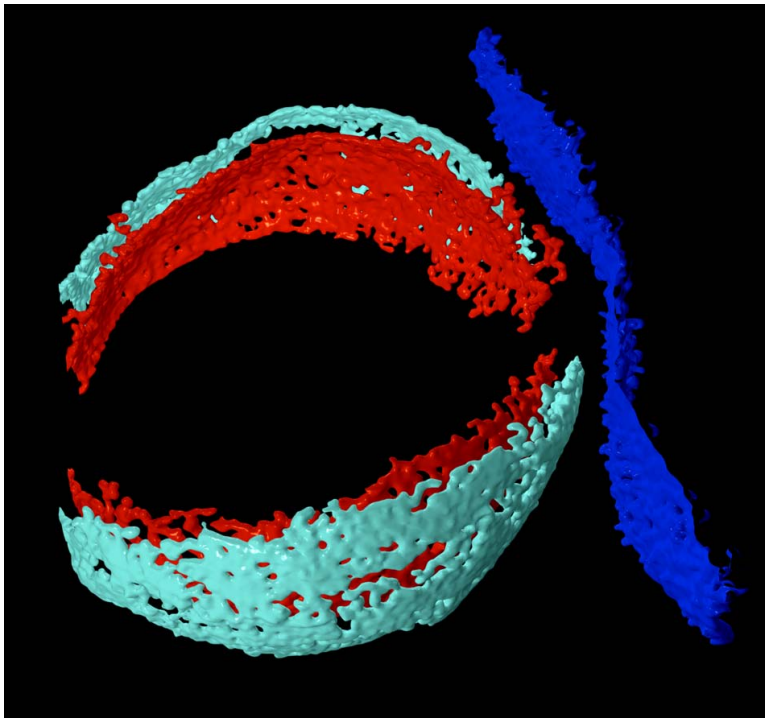

Figure 4.22: Iso-surface representation of the segmented membranes. *Nanoarchaeum equitans* with red and turquoise color and *Ignicoccus* with blue color iso-surface.

The task of segmentation in this example was to isolate and segment the bacterial thylakoid membranes. Calculation of the scaling indices for a radius that would match their thickness, followed by thresholding, resulted in a mask that not only showed the arrangement of the thylakoids in space, but also revealed connection between the thylakoids and the inner membrane. The same segmentation concept was followed in the case of the outer membrane. This time, the scaling indices were calculated for a bigger radius, since the outer membrane is thicker than the thylakoids. Because of the noisy nature of the data, any small, spurious features present in the segmentation masks were removed by anisotropic morphological operators. The created binary masks were then multiplied with the original data and visualized by iso-surface representation as shown in Figure 4.24.

4.3 Discussion

SIBS turned out to be a robust method for the segmentation of structural features in electron tomograms, in spite of the low signal-to-noise ratio inherent in such 3-D density maps.

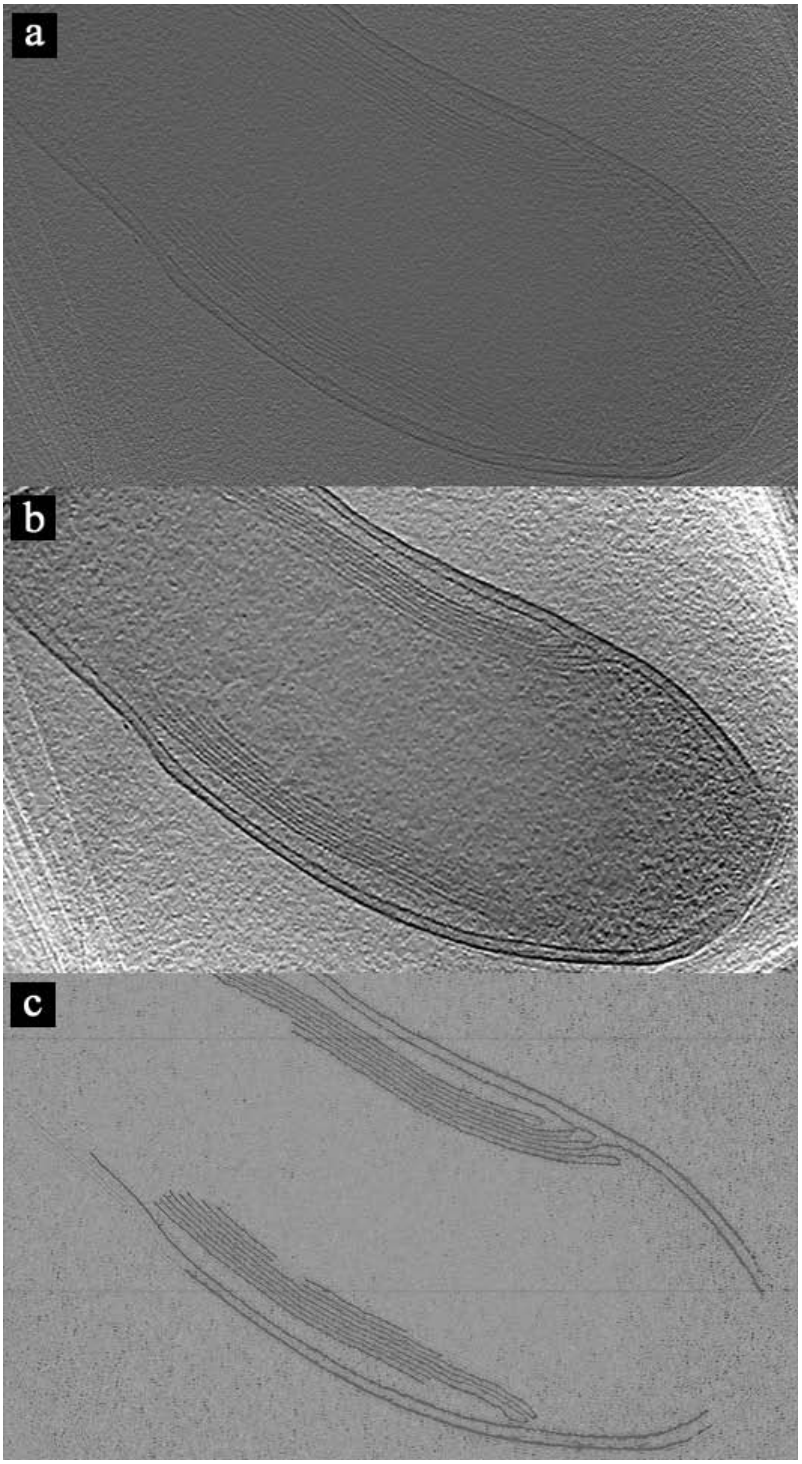

Figure 4.23: 2D XY-slice from the reconstruction of *R. viridis* a) original tomogram, b) denoised with N.A.D., and c) calculated scaling indices.

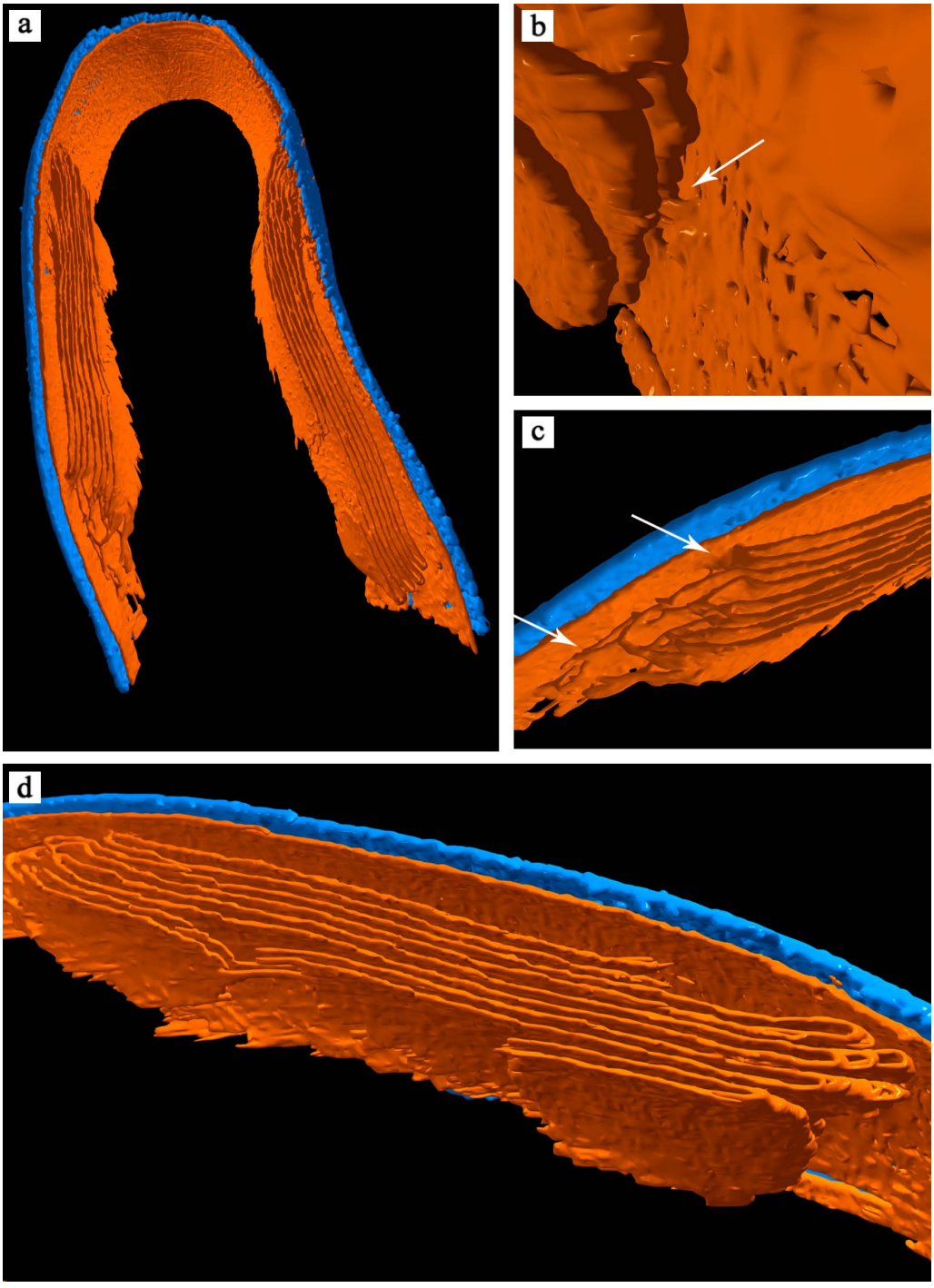

Figure 4.24: Iso-surface representation of the segmented thylakoid membranes. The arrows indicate connections between the thylakoids and the inner membrane.

Its great advantage is the flexibility in separating objects of different size. According to the size parameter r chosen, it can be used either in the sense of a foreground-background segmentation, e.g. when a whole cell has to be separated from its environment (example: *S. melliferum*), or with hierarchically descending r for the segmentation of smaller features down to a molecular level (example: *Dictyostelium*). In other words, the decision made for the classification of each pixel/voxel during the segmentation is based on information either of a local neighborhood for a small r, or of a more global neighborhood for a big r.

SIBS proved to be a very practical segmentation tool for membranes. The time consuming and subjective manual segmentations could be replaced by an automatic or a semi-automatic but fully parameter-controlled scaling index based segmentation. Especially at points, where due to the missing wedge the membrane seems to diffuse with the background, or where a membrane is connected to another membrane, SIBS could clearly define its borders and separate one from the other.

It is also easy to handle because, for calculating the WSI, only two parameters have to be defined by the user: the size parameter r and a scaling factor for the density values. In our applications, the whole range of density values was scaled to values from 0 to 128. This choice is a compromise between WSI-maps with too much smoothing and such maps with too many details, obtained by smaller or larger scaling, respectively. The choice of adequate morphological operators may require more experience and has to be directed by the type of structure to be segmented.

Chapter 5

Automated detection of macromolecules from electron tomograms using the Scaling Index Method

Electron tomography is the only technique available that allows us to visualize the three-dimensional structure of unfixed and unstained cells. Currently, the resolution obtained in electron tomography of cellular structures is in the range of 4 to 6 nm. Nevertheless, the goal of cellular electron tomography is not to obtain a high-resolution structure of a particular macromolecule; the goal is to identify a molecule by virtue of its structural signature and to locate it in the context of its cellular environment. The detection of macromolecules is confronted with two major problems [Böhm et al., 2000]: i) The electron tomograms suffer from a very low SNR. Electron microscopic images of individual biological macromolecules are usually not directly accessible to structural interpretation because strong noise obscures the details of the objects examined. There are image processing techniques that can be used for the enhancement of the signal. However, these denoising techniques, although they improve the SNR, also modify the signal in a nonlinear way, precluding quantitative postprocessing [Frangakis et al., 2001]. ii) The cytoplasm is densely populated with molecules that often touch each other or overlap [Ellis, 2001].

In the case of single particle analysis, particles have to be detected in 2-D projection images. This is usually done interactively, though automatic detection procedures are in development . Here however, it is highly impractical to perform a particle detection based

on visual inspection of the 3-D tomographic volumes, except for some large-scale structures. Due to the very low SNR that characterizes the electron tomograms, a visual detection of particles may fail, especially with respect to the third dimension. Furthermore, it would also lack reproducibility and objectivity.

For this reason automated detection methods are preferred. These should be robust with respect to a low SNR, varying object orientation, object deformations, background variations, and image distortions, and they should be able to cope with multiple occurrence of the object. Template matching is a well known technique in image processing and has already been used in CryoET for identifying macromolecular complexes. Provided that a high resolution structure of the macromolecule is available, this structure can be used as a template to perform a systematic search of reconstructed volumes for matching structures. The search is based on cross-correlation and is entirely machine based, not requiring manual intervention. However, cross correlation is not rotationally invariant and requires scanning of the whole angular range. This is a computationally ineffective approach, especially in the case of searching 3D targets in extended volume data.

A novel approach for identification of macromolecular complexes is proposed in this chapter. The identification technique is not based on the similarity of the density values between input and target volume, as is the case in template matching, but on the similarity of the calculated scaling indices. The big advantage of this method is that it is very fast, since scaling index is rotationally invariant.

In the first part of this chapter, the template matching technique is presented, with emphasis on different correlation functions and the creation of templates from X-ray crystallography data. The next section describes the scaling index based correlation approach. Finally, results calculated on simulated data are presented, followed by a discussion concerning the applicability and efficiency of the method.

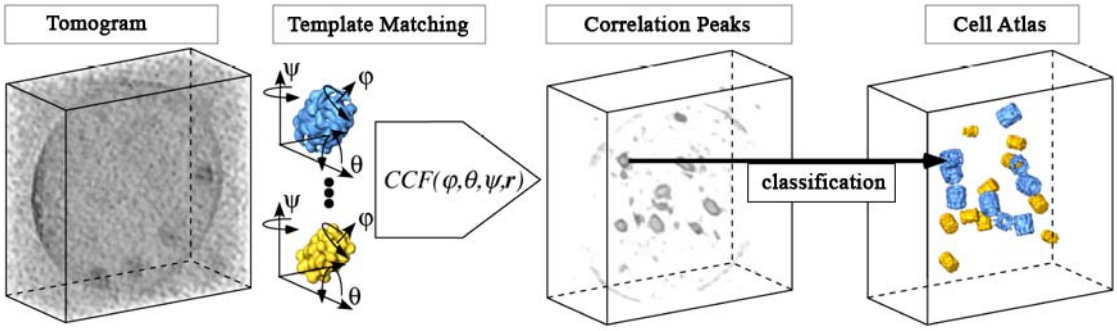

Figure 5.1: Scheme illustrating the strategy followed for identification of macromolecular complexes in cryo-electron tomograms.

5.1 Template matching

Cross-correlation is a mathematical operation that involves two signals with the intention to measure the degree to which the two signals are similar. Suppose that we have two, two-dimensional discrete signals $f(i,j)$ and $g(i,j)$. The cross-correlation of $f(i,j)$ and $g(i,j)$ is defined as:

$$R_{f,g}(x,y) = \sum_i \sum_j f(i,j) \cdot g(x-i, y-j) \tag{5.1}$$

In template matching, cross correlation techniques are used to measure the degree of overall similarity of the particles under scrutiny to structurally well-defined templates. These templates are created from high-resolution structural data obtained by techniques as X-ray crystallography, and nuclear magnetic resonance (NMR) spectroscopy. In the case of electron tomograms of cellular structures, the orientation of the particles is expected to be random. To yield the maximum of all cross-correlation coefficients, the whole angular range needs to be scanned with each template. Therefore, the templates are rotated with a 10° increment to account for every possible combination of Eulerian angles [Böhm et al., 2000]. The process is fully automated. After the detection of the particles, they are aligned and averaged [Förster et al., 2005]. The consecutive steps in the template matching procedure are illustrated by the scheme shown in Figure 5.1.

In CryoET, the analysis of a whole tomographic volume containing several hundred particles that need to be compared with an array of different templates would require a huge

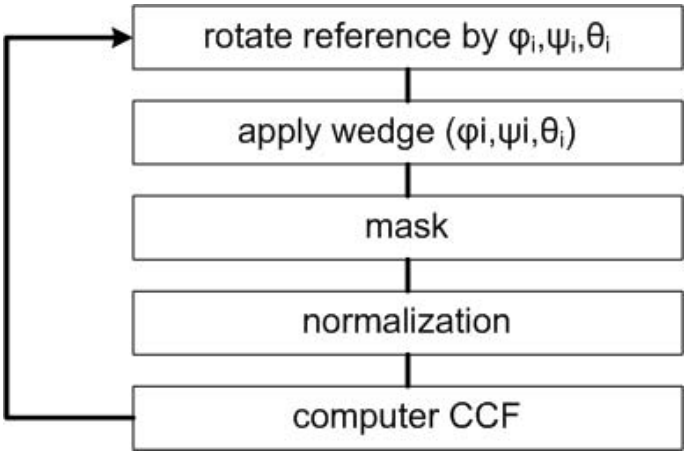

Figure 5.2: Individual steps of reference preparation.

amount of computation time. For this reason, parallelized versions of correlation algorithms are usually used. The correlation process can also be speeded up by an interesting feature of the correlation function. The correlation function can be efficiently expressed and computed in the Fourier space. If the Fourier transform of $f(i,j)$ and $g(i,j)$ are $F(u,v)$ and $G(u,v)$ respectively, then the correlation operation in Fourier domain is simply a point-by-point multiplication. The previous, time-consuming operation with high complexity is now replaced by two Fourier transforms, one multiplication and an inverse Fourier transform.

5.1.1 Influence of the Missing Wedge

The missing wedge causes a serious problem for templates matching as it distorts the shape of the observed macromolecules and introduces anisotropic resolution. In order to overcome this problem a "constrained correlation function" is used [Förster et al., 2005]. Figure 5.2 illustrates the individual steps of reference preparation before the correlation is performed. First the reference is rotated into an orientation (ϕ, ψ, θ). Then it is Fourier transformed and a wedge-shaped function is multiplied, corresponding to the imaging conditions of the tomogram under scrutiny. Back in real space, the reference and the subtomograms are masked. Then the mean value is subtracted and normalization according to the standard deviation with the masked area is performed. Eventually, the cross-correlation function is computed.

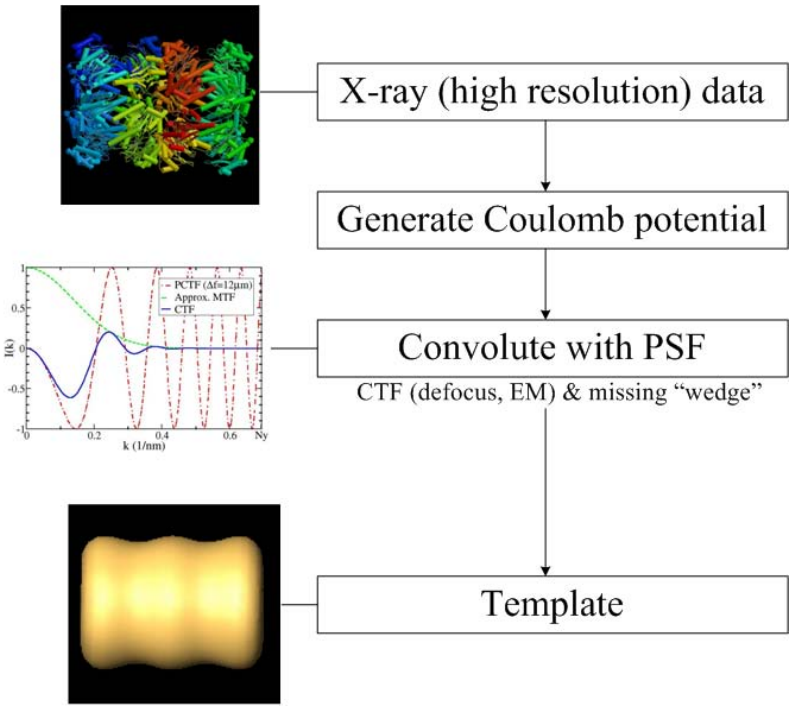

Figure 5.3: Scheme illustrating the creation of a template from X-ray crystallography data.

5.1.2 Template Creation

In order to correlate a structure obtained by other high-resolution imaging techniques with electron microscope data, it is essential to approximate how this structure would appear in an electron tomogram. A template is usually taken from an atomic-scale model of the complex derived either by X-ray or electron crystallography, NMR, single particle reconstructions, or any combination of these methods. To construct a template, the approximate electrostatic potential has to be calculated from the atomic coordinates by summing the total atomic numbers Z in each volume element. The resulting density is then convoluted with the appropriate Contrast Transfer Function (CTF) and low-pass filtered at a spatial frequency corresponding to the first zero crossing of the CTF of the electron microscope (Figure 5.3).

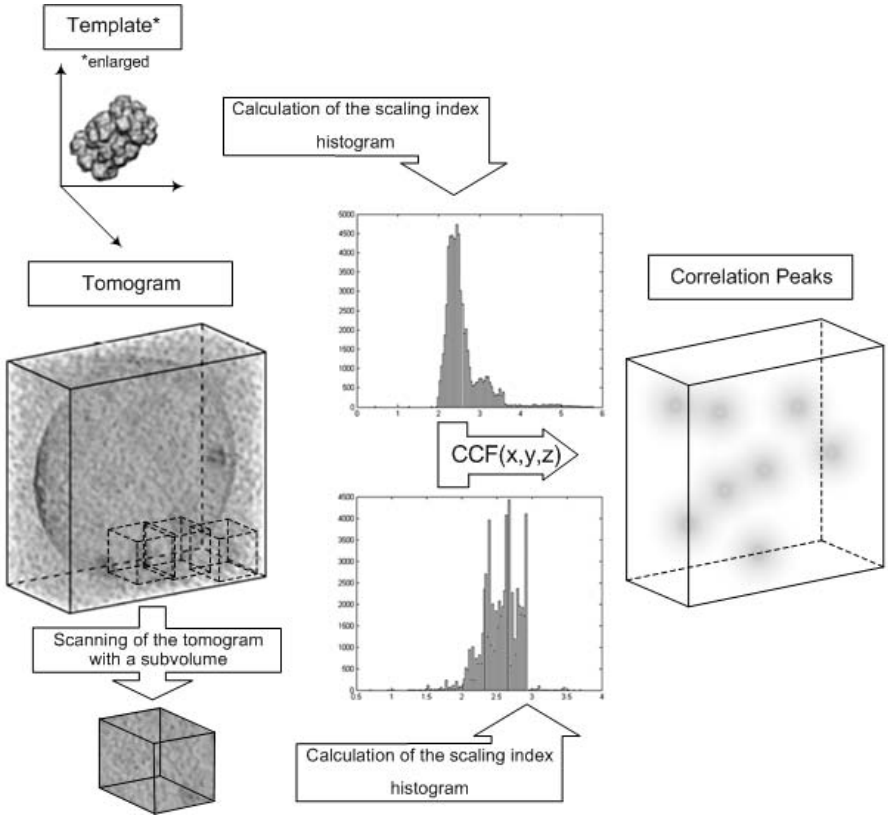

Figure 5.4: Scheme illustrating the scaling index based correlation. The correlation peaks indicate the positions of the identified particles.

5.2 Scaling Index Based Correlation

The scaling index method classifies objects present in an image or a volume, regardless of their orientation, according to the kind of structure to which they belong. A line will be identified as a line-like structure regardless of whether it is horizontally or vertically placed inside a volume. In this approach, instead of the gray values of an input and a target image, the histograms of the calculated scaling indices are used for performing correlation. The process is briefly explained as follows. The scaling indices are calculated using the same radius for the input and target (template) volume. A subvolume with the size of the target volume and centered at voxel k_i is cut out from the input volume. The scaling index histograms of the subvolume and the target volume are calculated and correlated. This is repeated for all voxels of the input volume, such that a CCC is assigned to each voxel of the tomogram. The main difference to template matching is that the 3-D correlation of the intensity values between target and input volume for every possible orientation is replaced

by a 1-D correlation between the histogram signals of the scaling indices of the input and target volume. By comparing the histograms, it is not necessary to rotate the target in different angles, since SIM can be considered as a rotationally invariant transformation. This approach is very fast since only one correlation coefficient needs to be calculated for each position.

5.3 Results

In order to explore the applicability of the algorithm in the field of electron tomography, it was applied to a simulated tomographic reconstruction. The simulated data were generated by randomly positioning and orienting low-frequency filtered molecular structures obtained by X-ray crystallography within a test volume. Two data-sets were produced by weighted back-projection from projection images in the angular range of $-70°$ to $+70°$ with $1.5°$ increment for the first data-set, and of $-55°$ to $+55°$ with $5°$ increment for the second one. Pink noise was added to the volumes in order to decrease the SNR. Slices through the simulated volumes containing the two types of molecules are shown in Figure 5.5.

Two test molecules of similar size and shape were used: the 20S proteasome (721 kDa [Groll et al., 1997]) and the thermosome (933 kDa [Nitsch et al., 1998]). Figure 5.6 shows iso-surface representations of the crystal structures of the test molecules, as well as the histograms of the calculated scaling indices.

In this example the scaling indices were calculated for a radius $r = 8$. This corresponds to a size of 13 nm (pixel size equal to 1.6 nm), which approximately matches the dimenions of the particles. The scaling index histograms of the target volume (template) was correlated with the scaling index histograms of subvolumes of the input volume. The cross-correlation coefficients assigned to each voxel are plotted in Figure 5.7a for the case of the proteasome template and in Figure 5.7b for the case of the thermosome template. These figures are again histograms, however, they display the frequency of the CCC values. The pixels could be classified according to the CCC into three groups: Group I consisting of pixels that correspond to the molecular complex used for searching, Group II consisting of pixels

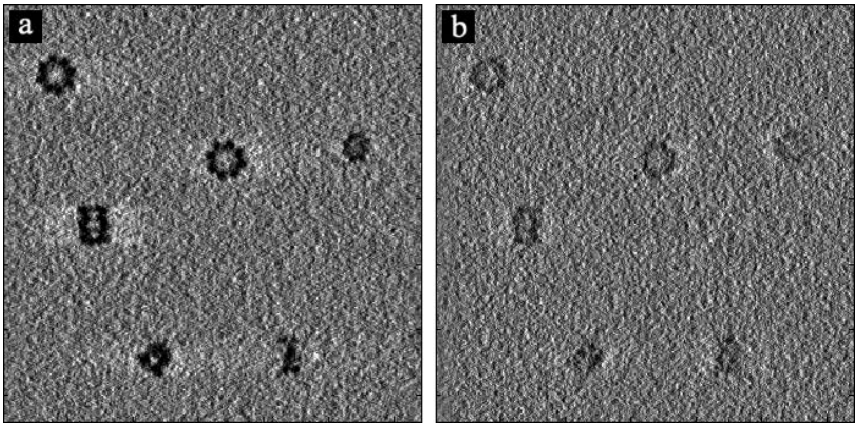

Figure 5.5: 2-D XY-slice from simulated tomograms containing thermosomes and proteasomes. a) volume created by weighted back-projection from projection images in the angular range of -70° to $+70^\circ$ with 1.5° increment, b) volume created by weighted back-projection from projection images in the angular range of -55° to $+55^\circ$ with 5° increment.

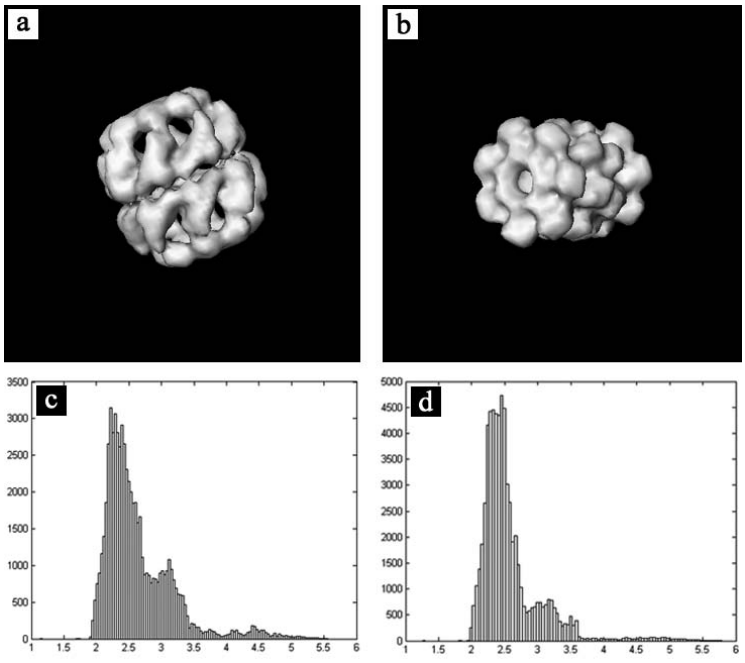

Figure 5.6: Iso-surface representation of a $a)$ thermosome, $b)$ proteasome, and $c, d)$ their histograms of the scaling indices, respectively.

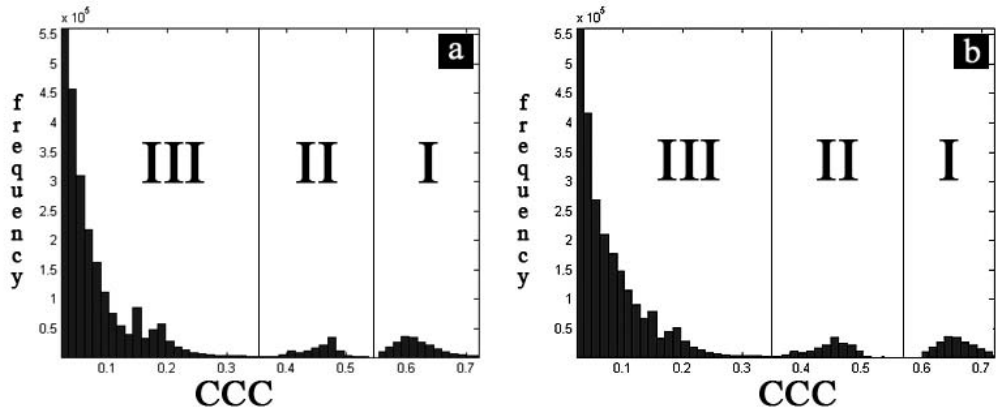

Figure 5.7: Diagram showing the CCC's derived from the correlation between the histograms of the template and the subvolumes of the input volume for the case of *a*) **proteasome, and** *b*) **thermosome.**

that correspond to a molecular complex, but not the one used for searching, and Group III consisting of noisy pixels without any structure. Since Group I and Group II are clearly distinguishable and not overlapping, the particles were identified correctly and clearly classified. This was controlled by comparing the particle coordinates in Group I with the coordinates of the particles pasted in the test-volume. All particles in Group I were correct. The correlation process lasted only 3 minutes on a HP c8000 workstation.

This was not the case in the second example, where the missing wedge effect was stronger (simulated data-set with angular range from $-55°$ to $+55°$ with $5°$ increment) and the method did not perform so well. In Figure 5.8, the histogram of the calculated CCC is plotted for the case of the thermosome template. Although the algorithm succeeded in localizing the particles, it failed to classify them into thermosomes and proteasomes, since the CCC's were not arranged into three distinct groups, as occurred in the previous example, but were merged into two groups, corresponding to background-like and particle-like voxels. Similar results were obtained using the proteasome template.

5.4 Discussion

Inevitably, the missing wedge is a limitation for this method. The arbitrary orientation of the particles inside the tomogram lead to the consequence that each particle is differently

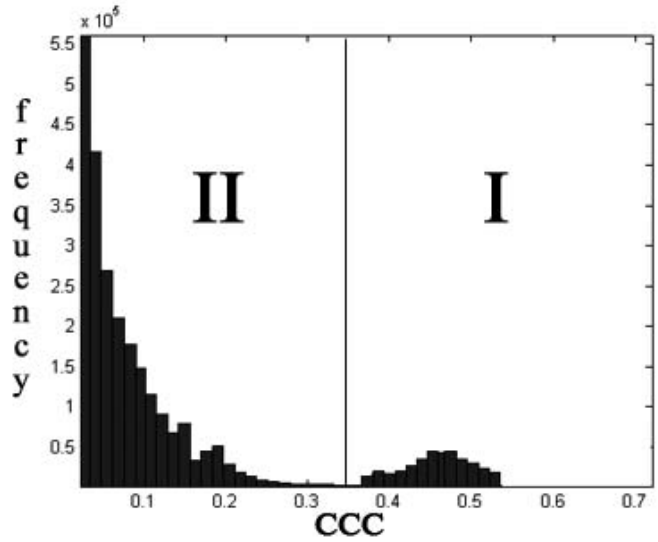

Figure 5.8: Diagram showing the CCC's derived from the correlation between the histograms of the template and the subvolumes of the input volume for the case of thermosome.

affected by the missing wedge. For each particle, the missing information in Fourier space causes, according to its orientation, different distortions in real space. Under these circumstances, using a rotationally invariant correlation for a single template has little chance of fulfilling its task. An improvement in the performance of the method could be achieved by using double tilt-axis data, where the missing wedge becomes a missing pyramid, reducing the amount of missing information.

Another limitation for the algorithm is the current resolution of the electron tomograms. The 4-5 nm resolution that can be achieved nowadays with CryoET, in conjunction with a pixel size of approximately 2-3 nm after binning, would result in the representation of a macromolecule having the size of a proteasome by only 5x5x5=125 voxels in the tomogram. This number of voxels is not sufficient for performing histogram correlation.

Since the scaling index based correlation is unable to determine the angles of the detected particles, it cannot be used directly for template matching. It could be used prior to correlation as a fast way to determine approximately the number of the particles present. Nevertheless, one advantage of the method is that high contrast points cannot affect the correlation result, since it is the scaling indices and not the gray values that are correlated.

In the correlation algorithms used for template matching in CryoET, a common problem is that membranes or other high contrast points are also treated as particles and a high CCC is assigned them. Such detections are considered as false positives and have to be manually removed after the correlation. In the case of the scaling index based correlation, such structures would not affect the correlation process, since their structural dimensionality is different from the one of the templates.

Despite the current limited applicability of the algorithm in the field of electron tomography, it would play an important role if the missing wedge problem could be minimized and if the prediction for improved resolution (2 nm, [Nickell et al., 2006]) can realized. Nevertheless,it could be ideal for locating objects in Magnetic Resonance Images (MRI), or Computed Tomography (CT) images. Another field that this method could be applied is the field of facial recognition. According to basic characteristics of a face (that are unique for each face), it could be used to identify different faces.

Bibliography

[Alberts, 1998] Alberts, B. (1998). The cell as a collection of protein machines: preparing the next generation of molecular biologists. *Cell*, 92:291–294.

[Barnard et al., 1992] Barnard, D., Turner, J. N., Frank, J., and McEwen, B. F. (1992). A 360 single-axis tilt stage for the high-voltage electron microscope. *Journal of Microscopy*, 167:39–48.

[Baumeister, 2002] Baumeister, W. (2002). Electron tomography towards visualizing the molecular organization of the cytoplasm. *Current Opinion in Structural Biology*, 12:679–684.

[Baumeister and Steven, 2000] Baumeister, W. and Steven, A. (2000). Macromolecular electron microscopy in the era of structural genomics. *Trends Biochem. Sci.*, 25(12):624–631.

[Böhm et al., 2000] Böhm, J., Frangakis, A. S., Hegerl, R., Nickell, S., Typke, D., and Baumeister, W. (2000). Toward detecting and identifying macromolecules in a cellular context: Template matching applied to electron tomograms. *PNAS*, 97(26):14245–14250.

[Briegel, 2005] Briegel, A. (2005). *Strukturuntersuchungen an Prokaryonten mit Kryo-Elektrontomographie*. PhD thesis, Technical University of Munich.

[Crowther et al., 1970] Crowther, R. A., Derosier, D. J., and Klug, A. (1970). The reconstruction of a three-dimensional structure from projections and its application to electron tomography. pages 319–340. Proc. Roy. Soc. Lond.

[Deisenhofer et al., 1984] Deisenhofer, J., amd K. Miki, O. E., Huber, R., and Michel, H. (1984). X-ray structure analysis of a membrane protein complex. electron density map

at 3Å resolution and a model of the chromophores of the photosynthetic reaction center from rhodopseudomonas viridis. *Journal of Molecular Biology*, 180(2):385–398.

[Deisenhofer et al., 1985] Deisenhofer, J., Epp, O., Miki, K., Huber, R., and Michel, H. (1985). Structure of the protein subunits in the photosynthetic reaction centre of rhodopseudomonas viridis at 3Å resolution. *Nature*, 318:618–624.

[DeRosier and Klug, 1968] DeRosier, D. J. and Klug, A. (1968). Reconstruction of three-dimansional structures from electron micrographs. *Nature*, 217:130–134.

[Dierksen et al., 1993] Dierksen, K., Typke, D., Hegerl, R., and Baumeister, W. (1993). Towards automatic electron tomography ii. implementation of autofocus and low-dose procedures. *Ultramicroscopy*, 49:109–120.

[Dierksen et al., 1992] Dierksen, K., Typke, D., Hegerl, R., Koster, A., and Baumeister, W. (1992). Towards electron tomography. *Ultramicroscopy*, 40:71–87.

[Dierksen et al., 1995] Dierksen, K., Typke, D., Hegerl, R., Walz, J., Sackmann, E., and Baumeister, W. (1995). Towards electron tomography. *Biophysical Journal*, 68(4):1416–1422.

[Donoho, 1993] Donoho, D. L. (1993). Nonlinear wavelet methods for recovery of signals, images, and densities from noisy and incomplete data. *American Mathematical Society, Defferent Perspectives on Wavelets*, 1:173–205.

[Donoho, 1995] Donoho, D. L. (1995). De-noising by soft-thresholding. *IEEE Transactions on Information Theory*, 41(3):613–627.

[Dubochet et al., 1988] Dubochet, J., Adrian, M., Chang, J. J., Homo, J. C., Lepault, J., McDowall, A. W., and Schultz, P. (1988). Cryo-electron microscopy of vitrified specimens. *Q Rev. Biophys.*, 21(2):129–228.

[Ellis, 2001] Ellis, R. J. (2001). Macromolecular crowding: obvious but underappreciated. *Trends Biochem. Sci.*, 26:597–604.

[Fernandez and Li, 2005] Fernandez, J. J. and Li, S. (2005). Anisotropic nonlinear filtering of cellular structures in cryoelectron tomography. 7(5):54–61.

[Frangakis and Hegerl, 2001] Frangakis, A. S. and Hegerl, R. (2001). Noise reduction in electron tomographic reconstructions using nonlinear anisotropic difussion. *Journal of Structural Biology*, 135:239–250.

[Frangakis and Hegerl, 2002] Frangakis, A. S. and Hegerl, R. (2002). Segmentation of two- and three-dimensional data from electron microscopy using eigenvector analysis. *Journal of Structural Biology*, 138:105–113.

[Frangakis et al., 2001] Frangakis, A. S., Stoschek, A., and Hegerl, R. (2001). Wavelet transform filtering and nonlnear anisotropic diffusion assessed for signal reconstruction performance on multidimensional biomedical data. *IEEE Trans. on Biomed. Eng.*, 48(2):213–222.

[Förster et al., 2005] Förster, F., Medalia, O., Zauberman, N., Baumeister, W., and Fass, D. (2005). Retrovirus envelope protein complex structure in *situ* studied by cryo-electron tomography. *PNAS*, 102(13):4729–4734.

[Grimm et al., 1997] Grimm, R., Baermann, M., Haeckl, W., Typke, D., Sackmann, E., and Baumeister, W. (1997). Energy filtered electron tomography if ice-embedded actin and vesicles. *Biophysical Journal*, 72:482–489.

[Grimm et al., 1996] Grimm, R., Koster, A. J., Ziese, U., Typke, D., and Baumeister, W. (1996). Zero-loss energy filtering under low-dose conditions using a post column energy filter. *Journal of Microscopy*, 183:60–68.

[Grimm et al., 1998] Grimm, R., Singh, H., Rachel, R., Typke, D., Zillig, W., and Baumeister, W. (1998). Electron tomography of ice-embedded procaryotic cells. *Biophysical Journal*, 74:1031–1042.

[Grünewald et al., 2003] Grünewald, K., Desai, P., Winkler, D. C., Heymann, J. B., Belnap, D. M., Baumeister, W., and Steven, A. C. (2003). Three-dimansional structure of herpes simplex virus from cryo-electron tomography. *Science*, 302:1396–1398.

[Groll et al., 1997] Groll, M., Dietzel, L., Lowe, J., Stock, D., Bochtler, M., Bartunik, H. D., and Huber, R. (1997). Structure of the 20s proteasome from yeast at 2.4Å resolution. *Nature*, 386:463–471.

[Hart, 1968] Hart, R. (1968). Electron microscopy of unstained biological material: the polytropic montage. *Science*, 159:1464–1467.

[Hegerl and Hoppe, 1976] Hegerl, R. and Hoppe, W. (1976). Influence of electron noise on three-dimensional image reconstruction. *Z. Naturforschung*, 31a:1717–1721.

[Hoppe and Hegerl, 1980] Hoppe, W. and Hegerl, R. (1980). *Three-dimensional structure determination by electron mixroscopy (nonperiodic specimens)*, volume 13 of *Topics in Current Physics : Computer Processing of Electron Microscope Images*. Springer-Verlag, Berlin Heidelberg New York.

[Ikeda-Yamasaki et al., 1998] Ikeda-Yamasaki, I., Odahara, T., Mitsuoka, K., Fujiyoshi, Y., and Murata, K. (1998). Projection map of the reaction center-light harvesting 1 complex from rhodopseudomonas viridis at 10Å resolution. *FEBS Lett.*, 425(3):505–508.

[Jamitzky et al., 2001] Jamitzky, F., Stark, R. W., Bunk, W., Thalhammer, S., Räth, C., Aschenbrenner, T., and Morphill, G. E. (2001). Scaling-index as an image processing tool in scanning-probe microscopy. *Ultramicroscopy*, 86:241–246.

[Jiang et al., 2003] Jiang, W., Baker, L. M., Wu, Q., Baraj, C., and Chiu, W. (2003). Applications of bilateral denoising filter in biological electron microscopy. *Journal of Structural Biology*, 144:114–122.

[Koster and de Ruijter, 1992] Koster, A. J. and de Ruijter, W. J. (1992). Practical autoalignment of transmission electron microscopes. *Ultramicroscopy*, 40:89–107.

[Koster et al., 1989] Koster, A. J., de Ruijter, W. J., van den Bos, A., and van der Mast, K. D. (1989). Autotuning of a tem using minimum electron dose. *Ultramicroscopy*, 27:251–272.

[Koster et al., 1998] Koster, A. J., Grimm, R., Typke, D., Hegerl, R., Stoschek, A., Walz, J., and Baumeister, W. (1998). Perspectives of molecular and cellular electron tomography. *Journal of Structural Biology*, 120:276–308.

[Kürner et al., 2005] Kürner, J., Frangakis, A. S., and Baumeister, W. (2005). Cryo-electron tomography reveals the cytoskeletal structure of spiroplasma melliferum. *Science*, 302:436–438.

[Lang and Oesterhelt, 1989] Lang, F. S. and Oesterhelt, D. (1989). Gene transfer system for rhodopseudomonas viridis. *J. Bacteriol.*, 171:4425–4435.

[Lucic et al., 2005] Lucic, V., Foerster, F., and Baumeister, W. (2005). Structural studies by electron tomography: From cells to molecules. *Annu. Rev. Biochem.*, 74:833–865.

[Mannella et al., 1994] Mannella, C. A., Marko, M., Penczek, P., Barnard, D., and Frank, J. (1994). The internal compartmentation of rat-liver mitochondria : Tomographic study using high-voltage transmission electron microscope. *Microsc. Res. Tech.*, 27:278–283.

[McEwen et al., 1995] McEwen, B., Downing, K., and Glaeser, R. (1995). The relevance of dose-fractionation in tomography of radiation-sensitive specimens. *Ultramicroscopy*, 60:357–373.

[Medalia et al., 2002] Medalia, O., Weber, I., Frangakis, A., Nicastro, D., Gerisch, G., and Baumeister, W. (2002). Macromolecular architecture in eukaryotic cells visualized by cryoelectron tomography. *Science*, 298(5596):1209–1213.

[Nickell et al., 2006] Nickell, S., Kofler, C., Leis, A. P., and Baumeister, W. (2006). A visual approach to proteomics. *Narure Reviews: Molecular Cell Biology*, 7:225–230.

[Nitsch et al., 1998] Nitsch, M., Walz, J., Typke, D., Klumpp, M., Essen, L., and Baumeister, W. (1998). Group ii chaperonin in an open conformation examined by electron tomography. *Nat. Struct. Biol.*, 5:855–857.

[Ortiz et al., 2006] Ortiz, J., Förster, F., Kürner, J., Linaroudis, A., and Baumeister, W. (2006). Mapping 70s ribosomes in intact cells by cryo-electron tomography and pattern recognition. *Journal of Structural Biology*, in press.

[Penczek et al., 1995] Penczek, P., Marko, M., Buttle, K., and Frank, J. (1995). Double-tilt electron tomography. *Ultramicroscopy*, 60:393–410.

[Perona and Malik, 1987] Perona, P. and Malik, J. (1987). Scale space and edge detection using anisotropic diffusion. pages 16–22. IEEE Comp. Soc. Workshop on Computer Vision, IEEE Comnputer Society Press.

[P.Perona and Malik, 1990] P.Perona and Malik, J. (1990). Scale space and edge detection using anisotropic diffusion. *IEEE Transactions on Pattern Analysis and Machine Intelligence*, 12(7):629–639.

[Radon, 1917] Radon, J. (1917). Über die bestimmung von funktionen durch ihre integralwerte längs gewisser mannigfaltigkeiten. *Berichte Sächsische Akademie der Wissenschaften, Leipzig, Math.-Phys.*, 69:262–277.

[Rosenfeld and Kak, 1982] Rosenfeld, A. and Kak, A. (1982). *Digital Picture Processing*. Morgan Kaufmann.

[Räth et al., 2002] Räth, C., Bunk, W., Huber, M., Morfill, G., Retzlaff, J., and Schuecker, P. (2002). Analysing large scale structures: weighted scaling indices and constrained randomization. *Mon. Not. R. Astron. Soc.*, 337(2):413–421.

[Räth and Morfill, 1997] Räth, C. and Morfill, G. (1997). Texture detection and texture discrimination with anisotropic scaling indices. *J. Opt. Soc. Am.*, 14(12):3208–3215.

[Russ, 1995] Russ, J. C. (1995). *The Image Processing Handbook*. CRC Press, Inc, second edition.

[Saxton and Baumeister, 1982] Saxton, W. O. and Baumeister, W. (1982). The correlation averaging of a regularly arranged bacterial cell envelope protein. *Journal of Microscopy*, 127:127–138.

[Scheuring et al., 2003] Scheuring, S., Seguin, J., Marco, S., Lévy, D., and Rigaud, B. R. J. (2003). Nanodissection and high-resolution imaging of the rhodopseudomonas viridis photosynthetic core complex in native membranes by afm. *PNAS*, 100(4):1690–1693.

[Schweikert, 2004] Schweikert, G. (2004). Quantitativer vergleich der strahlschädigung biologischer proben im transmissions-elektronenmikroskop bei stickstoff und helium temperatur. Diploma thesis, Technical Univercity of Munich.

[Soille, 2003] Soille, P. (2003). *Morphological Image Analysis*. Springer, second edition.

[Soille and Talbot, 2001] Soille, P. and Talbot, H. (2001). Directional morphological filtering. *IEEE Transactions on Pattern Analysis and Machine Intelligence*, 11(23):1313–1329.

[Tomasi and Manduchi, 1998] Tomasi, C. and Manduchi, R. (1998). Bilateral filtering for gray and color images. pages 59–66. IEEE Inter. Conf. on Computer Vision, IEEE Comnputer Society Press.

[Typke et al., 1991] Typke, D., Dierksen, K., and Baumeister, W. (1991). Automatic electron tomography. pages 544–545. 49th Annual Meeting EMSA, San Francisco Press.

[Weickert, 1998a] Weickert, J. (1998a). *Anisotropic Difussion in Image Processing*. Taubner.

[Weickert, 1998b] Weickert, J. (1998b). Coherence enhancing diffusion filtering. *Int. Journal of Computer Vision*, 31(2):111–127.

Publications containing parts of this thesis

[Linaroudis and Hegerl, 2006] Linaroudis, A. A. and Hegerl, R. (2006). SIBS, a powerful concept for segmentation of electron tomograms. *Proc. of SPIE*, 6144(61443H):1-7

[Linaroudis et al, 2006] Linaroudis, A. A., Frangakis, A. S. and Hegerl, R. (2006). Image processing techniques based on the scaling index method in the field of electron tomography. In preparation

[Ortiz et al., 2006] Ortiz, J., Förster, F., Kürner, J., Linaroudis, A. A. and Baumeister, W. (2006). Mapping 70S ribosomes in intact cells by cryo-electron tomography and pattern recognition. *Journal of Struct. Biol.*, in press

[Scheffel et al., 2006] Scheffel, A., Gruska, M., Faivre, D., Linaroudis, A. A., Plitzko, J. M., Schüler, D. (2006). An acidic protein aligns magnetosomes along a filamentous structure in magnetotactic bacteria. *Nature*, 440(7080):110-114

[Cyrklaff et al, 2006] Cyrklaff, M., Linaroudis, A. A., Boicy, M., Baumeister, W., Griffiths, G., Krijnse-Locker, J. (2006). Structural changes of vaccinia virus core upon cell infection revealed by whole cryo-electron tomography. In preparation

[Nickell et al., 2005] Nickell, S., Förster, F., Linaroudis, A. A., Del Net, W., Beck, F., Hegerl, R., Baumeister, W., Plitzko, J. M. (2005). Tom toolbox, acquisition and analysis for electron tomography. *Journal of Struct. Biol.*, 149(3):227-234

[Kürner et al., 2004] Kürner, J. and Medalia, O., Linaroudis, A. A. and Baumeister, W. (2004). New insights into the structural organization of eukaryotic and prokaryotic cytoskeletons using cryo-electron tomography. *Exper. Cell Research*, 301:38-42

[Linaroudis and Hegerl, 2004] Linaroudis, A. A. and Hegerl, R. (2004). Automatic segmentation of electron tomograms based on the scaling index. *Proc. of* 13^{th} *Europ. Microsc. Congress*, vol.I:425-426

Acknoledgments

First and foremost I would like to thank Dr. R. Hegerl for supporting my work in every possible way. His approach to image processing problems, his care in research and his advice have proven invaluable.

I would like to give my sincere gratitude to Professor Dr. W. Baumeister for giving me the opportunity to pursue my Doctor degree in his department.

I would like to acknowledge my colleagues Andrew Leis, Julio Ortiz, Anna Sartori, Manuella Gruska, Christine Kofler, Christoph Best, Jürgen Plitzko, Ohad Medalia, and Marek Cyrklaff for many helpful discussions and a friendly working environment.

A big "thank you" goes to my friend William Del Net for his support during the last four years.

I am pleased to acknowledge my friend Dr. A. S. Frangakis for valuable discussions and advice throughout the whole project.

I would like to thank my girlfriend Mariana for her unconditional love and support.

I feel liable to thank my family for their moral and financial support throughout my studies.

Finally, I feel obliged to embrace all my friends here in Munich, who contributed to these unforgettable and exceptional years.

Alexandros A. Linaroudis